M 2021

U.PORTO
FEUP FACULDADE DE ENGENHARIA
UNIVERSIDADE DO PORTO

THERMAL CHARACTERIZATION OF INJECTED THERMOPLASTIC COMPOSITES BY LASER FLASH ANALYSIS

ANA LUÍSA AZEVEDO COSTA

DISSERTAÇÃO DE MESTRADO APRESENTADA
À FACULDADE DE ENGENHARIA DA UNIVERSIDADE DO PORTO EM
ENGENHARIA QUÍMICA

Master in Chemical Engineering

Thermal Characterization of Injected Thermoplastic Composites by Laser Flash Analysis

Master dissertation

of

Ana Luísa Azevedo Costa

Developed within the course of dissertation

held in

Bosch Car Multimedia Portugal, S.A.



Supervisor at FEUP: Professor Dr. Joaquim Faria

Coordinator at Bosch Car Multimédia Portugal, S.A.: Susana Silva





July 2021

CLASSIFIED DOCUMENT. USE ONLY FOR EVALUATION PURPOSES

Acknowledgments

I want to thank all the people whose help and support was essential for the accomplishment of this dissertation.

First, I want to thank my supervisor at FEUP, Professor Joaquim L. Faria, for the guidance, cooperation and knowledge provided. I thank you for your enormous availability during the entire process. Professor Joaquim L Faria is member of the Associate Laboratory LSRE-LCM funded by national funds through FCT/MCTES (PIDDAC): Base Funding UIDB/50020/2020.

I also want to thank my supervisor at Bosch, Engineer Susana Silva, for the constant support and all the suggestions and knowledge transmitted during the elaboration of the dissertation. Your cooperation was essential to the conclusion of this work and your good mood truly facilitated my integration into Bosch and made all the work easier.

I thank my colleagues at Bosch, who I quote:

Engineers Aníbal Portinha and Pedro Bernardo, for the cooperation and pushing me to do a work with more quality and importance to the innovation group. I appreciate you allowing me to feel welcomed and integrated into this group.

The entire group in the EHP-Brg department at Bosch who were always ready to help and created a great work environment.

Engineers Teresa Cardoso and Carlos Ferreira, for providing me with liquid nitrogen every day I needed to use the Laser Flash equipment and for helping me with the SEM-EDX tests. I appreciate your enormous availability.

Engineer Rui Araújo for the cooperation and availability to help me with TGA analysis.

Eduardo and Vítor, my partners in this internship, for the friendship and for helping me to integrate better in this stage of our lives.

I specially thank my family for the support and encouragement in everything I do.

FCT Fundação para a Ciência e a Tecnologia
MINISTÉRIO DA CIÊNCIA, TECNOLOGIA E ENSINO SUPERIOR
REPÚBLICA PORTUGUESA

Abstract

Research in the field of engineering plastics is becoming increasingly important for the application of new lighter materials with enhanced performances, particularly in the automotive industry. This dissertation arises from the idea of replacing metals with thermoplastic materials in heat sinks. The purpose of this experimental work is to evaluate the thermal conductivity of carefully selected thermoplastic composites, as well as their morphology and processability by injection moulding. In particular, to study the effects of mould temperature and filler dispersion on thermal conductivity.

In this sense, the thermal diffusivity of different materials was measured using Laser Flash Analysis (LFA). To evaluate the effect of mould temperature, discs of the same material were produced by injection moulding with different mould temperatures while maintaining all other injection parameters. To understand the differences in the filler dispersion during the injection process and their impact on the thermal properties, measurements were performed for different regions of the same disc. Density was determined according to Archimedes' principle and specific heat capacity was measured using both LFA and Differential Scanning Calorimetry (DSC). The samples were characterized by Scanning Electron Microscopy (SEM), Energy Dispersive X-Ray Spectrometry (EDX) and Thermogravimetric Analysis (TGA). SEM images were analysed with an image processing software (ImageJ). Theoretical models for thermal conductivity prediction were compared to the experimental results and used to predict the thermal behaviour of each material with different filler volume fractions.

The results show an increase in thermal conductivity in the melt flow direction, with values increasing up to 165 % in positions only 20 mm apart. Additionally, increasing mould temperature resulted in higher thermal conductivity. While SEM and EDX weren't conclusive, the image processing and TGA indicate that these differences could root from higher filler content in the regions further from the injection point. Lewis and Nielsen's model delivered an accurate estimation of thermal conductivity for two-phase mixtures, while Cheng's model did the same for multi-phase mixtures.

Keywords: Laser Flash Analysis; Thermal Conductivity; Thermoplastic Composites; Injection Moulding

Resumo

A investigação na área de plásticos de engenharia é cada vez mais importante para a aplicação de novos materiais mais leves e mais eficiente, em particular na indústria automotiva. Esta dissertação surge da possibilidade de substituir metais por termoplásticos compositos em dissipadores de calor. O objetivo deste trabalho experimental é avaliar a condutividade térmica de compósitos termoplásticos estrategicamente selecionados, bem como a sua morfologia e processabilidade por moldagem por injeção. Em particular, estudar o efeito da temperatura de molde e da dispersão de particulas de enchimento no molde na condutividade térmica.

Nesse sentido, a difusividade térmica dos diferentes materiais foi medida com o método de Laser Flash (LFA). Para avaliar o efeito da temperature de molde, discos do mesmo material foram fabricados por moldagem por injeção a diferentes temperaturas de molde, mantendo todos os outros parâmetros. Para estudar as diferenças na dispersão das particulas de enchimento durante o processo de injeção e o seu impacto nas propriedades térmicas, foram realizadas medições para diferentes regiões de cada amostra. A densidade foi determinada de acordo com o princípio de Arquimedes e a capacidade de calor específica foi medida usando LFA e Calorimetria Diferencial de Varrimento (DSC). As amostras foram caracterizadas por Microscopia Eletrónica de Varrimento (SEM), Espectrometria de Energia Dispersiva de Raios-X (EDX) e Análise Termogravimétrica (TGA). As imagens obtidas por SEM foram avaliadas com um software de processamento de imagem (ImageJ). Modelos teóricos para previsão da condutividade térmica foram comparados com os resultados experimentais e usados para prever o comportamento térmico de cada material com diferentes frações de volume de enchimento.

Os resultados mostram diferenças na condutividade térmica em diferentes regiões da parte injetada, obtendo-se diferenças de até 165 % em apenas 20 mm de distância. Denota-se um aumento da condutividade térmica na direção do fluxo do material, com valores menores junto ao ponto de injeção. O aumento da temperatura do molde resultou numa maior condutividade térmica. Embora as análises de SEM-EDX não tenham sido conclusivas, o processamento de imagem (ImageJ) e TGA indicam que essas diferenças podem ter origem num conteúdo superior de enchimento nas regiões mais afastadas do ponto de injeção. O modelo de Lewis e Nielsen forneceu uma estimativa precisa da condutividade térmica para misturas de duas fases, enquanto o modelo de Cheng fez o mesmo para misturas multifásicas.

Palavras-Chave: Método Laser Flash; Condutividade térmica; Compósitos termoplásticos; Moldagem por Injeção

Declaration

I hereby declare, under word of honour, that this work is original and that all non-original contributions is indicated and due reference is given to the author and source



Ana Luísa Azevedo Costa, 5 July, 2021

Index

1 Introduction 1

1.1 Framing and presentation of the work 1

1.2 Presentation of the company 2

1.3 Contribution of the author to work 2

1.4 Organization of the dissertation 2

2 Context and State of the art 3

2.1 Composite materials in automotive applications 4

2.1.1 Heat sinks 5

2.2 Theory of thermal conductivity 5

2.3 Factors affecting thermal conductivity of composite materials 7

2.3.1 Crystallinity 8

2.3.2 Chain structure 8

2.3.3 Orientation 9

2.3.4 Filler intrinsic thermal conductivity 9

2.3.5 Filler loading level 9

2.3.6 Filler shape 10

2.3.7 Filler size 10

2.3.8 Hybrid fillers 10

2.3.9 Surface modification 11

2.4 Injection moulding process 11

2.5 Experimental approach for thermal conductivity measurements 13

2.6 Theoretical approach for thermal conductivity predictions 14

3 Materials and Methods 17

3.1 Material Selection 17

3.2 Injection Moulding 19

3.3 Characterization Techniques 19

3.3.1 Experimental approach 19

3.3.2 Sample Density Determination 20
3.3.3 Laser Flash Analysis 21
3.3.4 Differential Scanning Calorimetry 23
3.3.5 Scanning electron microscopy and Energy Dispersive X-ray spectroscopy 25
3.3.6 Image processing 26
3.3.7 Thermogravimetric Analysis 26
4 Results and Discussion 27
4.1 Thermal diffusivity 27
4.2 Specific Heat Capacity 28
4.3 Thermal conductivity 30
4.4 SEM/EDX 39
4.5 Image processing 40
4.6 TGA 41
4.7 Micromechanical Models 42
5 Conclusions 45
6 Assessment of the work done 46
6.1 Objectives achieved 46
6.2 Limitations and Future Work 46
6.3 Final Assessment 46
7 References 47
Appendix A - Properties of different polymers 51
Appendix B - Thermal conductivity of commonly used thermally conductive fillers 52
Appendix C - Technical specifications of the LFA equipment 53
Appendix D - Experimental results of thermal conductivity 54
D.1 Sample A 54
D.2 Samples B-HMT and B-LMT 55
D.3 Samples C-HMT and C-LMT 59
D.4 Samples B and C 63
D.5 Samples D-HMT and D-LMT 65

Appendix E - SEM 69

Appendix F - EDX 71

I.1 Material B 71

I.2 Material C 72

I.3 Material D 74

Appendix G - Image processing 76

Appendix H - Lewis and Nielsen's Model parameters 78

List of Figures

Figure 2-1 – Thermoplastic applications in car parts[11]. 4

Figure 2-2 – Various Heat sinks: (a) Plate Fin Heat Sink, (b) Square Pin Fin Heat Sink, (c) Round Pin Fin Heat Sink-inline and (d) Round Pin Fin Heat Sink-Staggered[12]. 5

Figure 2-3 – Factors causing phonon scattering in polymers. Reproduced from[15]. 6

Figure 2-4 – (a) Thermal conduction paths in high fillers loading; (b) Percolation phenomenon; (c) Thermoelastic coefficient theory[18]....7

Figure 2-5 – Comparison by the Newton pendulum of thermal conductivity in (a) crystalline materials and (b) polymers[21]....8

Figure 2-6 – Schematic of (a) the crystalline and amorphous domains of a polymer and (b) the structure of a polymer chain [23]. 8

Figure 2-7 – Effect of molecular chain alignment on heat transfer on a polymer with (a) high chain orientation and (b) less chain alignment....9

Figure 2-8 – Representation of the injection unit, including the hopper, rotating screw and the heated barrel. 12

Figure 2-9 –Representation of (a) the fountain flow during injection moulding and (b) the profile injection-moulded parts made of polymer composites. Reproduced from[41]. 13

Figure 3-1 – Synthesis of (a) PA6, (b) PBT and (c) PA6,6. 17

Figure 3-2 – (a) Hydrogen bonding between adjacent PA chains; (b) A possible water absorption mechanism and disruption of the H-bonded bridges.... 18

Figure 3-3 – Composition off the thermoplastic composites studied. 18

Figure 3-4 – Diagram of the steps followed in the experimental work.... 20

Figure 3-5 – a) Archimedes set for density measurement and b) representation of steps for measurement, with the samples in the top and bottom holder[50].... 21

Figure 3-6 – Sample cutting: a) and b) for in-plane and c) and d) for through-plane measures; deposition of graphite layers: e) before and g) after for in-plane and g) before and h) after for through-plane measures; Sample assembly: i) and j) in-plane, k) through-plane and l) total. 22

Figure 3-7 – LFA measuring windows and different parameters.... 23

Figure 3-8 – DSC curves of standard and unknown Specimens[52].... 24

Figure 3-9 – a) STA 409 PC Luxx®, NETZSCH, used for DSC measurements; b) Crucible placed on the heat flux sensor.... 24

Figure 3-10 – a) Hitachi FlexSEM 1000 SEM; Sample preparation: b) Sample in liquid nitrogen,.... 25

Figure 3-11 – Sample a) before and b) after breaking for TGA measurements. 26

Figure 4-1 – Through-plane thermal diffusivity for position 2. 27

Figure 4-2 – In-plane thermal diffusivity for position 2. 27

Figure 4-3 – Specific Heat obtained by DSC and LFA for samples (a) A, (b) B, (c) C and (d) D. 29

Figure 4-4 – Representation of the through-plane thermal conductivity for position 2. 30

Figure 4-5 – Representation of the in-plane thermal conductivity for position 2. 31

Figure 4-6 – Representation of the in-plane thermal conductivity at 35 ºC. 32

Figure 4-7 – Representation of the disc samples, with the different analysed positions in blue. 32

Figure 4-8 – Representation of the through-plane thermal conductivity at 35 ºC. 33

Figure 4-9 – Flow pattern in a disc produced from injection moulding. 33

Figure 4-10 – Through-plane thermal conductivity of sample A at 35 ºC. 34

Figure 4-11 – Through-plane thermal conductivity of B-LMT and B-HMT at 35 ºC. 34

Figure 4-12 – Through-plane thermal conductivity of C-LMT and C-HMT at 35 ºC. 35

Figure 4-13 – Through-plane thermal conductivity of B-HMT and C-HMT at 35 ºC. 36

Figure 4-14 – Through-plane thermal conductivity of B-LMT and C-LMT at 35 ºC. 37

Figure 4-15 –Thermal Conductivity in each position of D-LMT and D-HMT at 35 ºC. 37

Figure 4-16 – Representation of the sample cut for through-plane measurements, with each position in blue and the difference between them in green. 38

Figure 4-17 – SEM image of sample B-HMT for positions a) one, b) two and c) three and sample B-LMT for positions d) one, e) two and f) three. Image processing 39

Figure 4-18 – ImageJ analysis for sample B-LMT in position 2. 40

Figure 4-19 – TGA of the three positions of samples a) B-HMT and c) C-HMT. 41

Figure 4-20 – Theoretical prediction of thermal conductivity with increasing filler load for samples A, B and C using the Cheng model and D using the Lewis and Nielsen model. 44

Figure C-1 – LFA 467 HyperFlash® manufactured by NETZSCH. 53

Figure D-1 – Through-plane Thermal conductivity as a function of temperature of sample A. 54

Figure D-2 – Percentual increase in thermal conductivity as a function of temperature between positions in sample A. 54

Figure D-3 – Through-plane Thermal conductivity as a function of temperature of sample B-HMT. 55

Figure D-4 – Percentual increase in thermal conductivity as a function of temperature between positions in sample B-HMT. 55

Figure D-5 – Through-plane thermal conductivity as a function of temperature of sample B-LMT. 56

Figure D-6 - Percentual increase in thermal conductivity as a function of temperature between positions in sample B-LMT. 56

Figure D-7 – Through-plane thermal conductivity as a function of temperature of B-HMT and B-LMT in positions a) one, b) two, c) three and d) four. 57

Figure D-8 – Increase in through-plane thermal conductivity for sample B-HMT and B-LMT between positions a) one and two, b) two and three, c) one and four and d) two and four. 58

Figure D-9 – Through-plane Thermal conductivity as a function of temperature of sample C-HMT. 59

Figure D-10 - Percentual increase in thermal conductivity as a function of temperature between positions in sample C-HMT. 59

Figure D-11 – Through-plane Thermal conductivity as a function of temperature of sample C-LMT. ... 60

Figure D-12 – Percentual increase in thermal conductivity as a function of temperature between positions in sample C-LMT. 60

Figure D-13 – Through-plane thermal conductivity as a function of temperature of C-HMT and C-LMT in positions a) one, b) two, c) three and d) four. 61

Figure D-14 – Increase in through-plane thermal conductivity for sample B-HMT and B-LMT between positions a) one and two, b) two and three, c) one and four and d) two and four. 62

Figure D-15 – Through-plane thermal conductivity as a function of temperature of B-HMT and C-LMT in positions a) one, b) two, c) three and d) four. 63

Figure D-16 – Through-plane thermal conductivity as a function of temperature of B-HMT and C-LMT in positions a) one, b) two, c) three and d) four. 64

Figure D-17 – Through-plane Thermal conductivity as a function of temperature of sample D-HMT.... 65

Figure D-18 – Percentual increase in thermal conductivity as a function of temperature between positions in sample D-HMT. 65

Figure D-19 – Through-plane Thermal conductivity as a function of temperature of sample D-LMT. ... 66

Figure D-20 – Percentual increase in thermal conductivity as a function of temperature between positions in sample D-LMT. 66

Figure D-21 – Through-plane thermal conductivity as a function of temperature of D-HMT and D-LMT in positions a) one, b) two, c) three and d) four. 67

Figure D-22 – Increase in through-plane thermal conductivity for sample D-HMT and D-LMT between positions a) one and two, b) two and three, c) one and four and d) two and four. 68

Figure E-1 – SEM image of sample A for positions a) one, b) two and c) three. 69

Figure E-2 – SEM image of sample C-HMT for positions a) one, b) two and c) three and sample C-LMT for positions d) one, e) two and f) three. 69

Figure E-3 – SEM image of sample D-HMT for positions a) one, b) two and c) three and sample D-LMT for positions d) one, e) two and f) three. 70

Figure F-1 – EDX spectrum for the material B-HMT. 71

Figure F-2 –EDX mapping analysis of material B-HMT: a) analysed areas, b) Carbon (C), c) Oxygen (O), d) Magnesium (Mg), e) Potassium (K), f) Silicon (Si), g) Iron (Fe), and h) Aluminium (Al). 71

Figure F-3 – EDX spectrum for the material C-HMT. 72

Figure F-4 – EDX mapping analysis of material C: a) analysed area, b) Oxygen (O), c) Iron (Fe), and d) Carbon (C). 73

Figure F-5 – EDX spectrum for the material D-HMT. 74

Figure F-6 – EDX mapping analysis of material D. 74

Figure G-1 – ImageJ for position: 1 a) B-HMT and b) B-LMT; position 2: c) B-HMT and d) B-LMT; position 3: e) B-HMT and f) B-LMT. 76

Figure G-2 – ImageJ for position: 1 a) C-HMT and b) C-LMT; position 2: c) C-HMT and d) C-LMT; position 3: e) C-HMT and f) C-LMT. 77

List of Tables

Table 1. Theoretical models for transverse effective thermal conductivity on two-phase mixtures. .. 15

Table 2. Theoretical models for transverse effective thermal conductivity on three- or multi-phase mixtures. 16

Table 3. Temperatures during the injection moulding process. 19

Table 4. Specific heat capacity calculated by LFA and DSC. 28

Table 5. Increase in thermal conductivity between different positions of samples B-HMT and B-LMT at 35 ºC. 38

Table 6. Estimation of percentage area of fillers in the SEM images of materials B and C, obtained by ImageJ. 40

Table 7. Final mass fraction for samples B-HMT, C-HMT and D-HTM, obtained by TGA. 42

Table 8. Comparison of experimental and theoretical models for sample D for longitudinal effective thermal conductivity using models for two-phase mixtures. 42

Table 9. Comparison of experimental and theoretical models for samples A, B and C for longitudinal effective thermal conductivity using models for multi-phase mixtures. 43

Table 10. Properties of some polymers[55]. 51

Table 11. Thermal conductivity values of commonly used thermally conductive fillers[55]. 52

Table 12. Technical specifications of the LFA equipment[43]. 53

Table 13. Normalized mass concentration of the chemical elements constituting samples B-LMT and B-HMT, obtained by Energy Dispersive X-ray spectroscopy. 72

Table 14. Normalized mass concentration of the chemical elements constituting samples C-LMT and C-HMT, obtained by Energy Dispersive X-ray spectroscopy. 73

Table 15. Normalized mass concentration of the chemical elements constituting samples D-HMT, obtained by Energy Dispersive X-ray spectroscopy 75

Table 16. Value of A for various systems [56]. 78

Table 17. Value of Φ_m for various systems [56]. 79

Notation and Glossary

A	Shape parameter in Lewis and Nielsen's Model	
c_p	Specific heat capacity	$J \cdot g^{-1} \cdot K^{-1}$
d	Thickness	m
D	Vertical displacement between the baseline and the specimen DSC thermal curves at a given temperature	W
k	Thermal conductivity	$W \cdot m^{-1} \cdot K^{-1}$
l	Phonon mean free path	m
m	Mass	g
q	Heat flux	$W \cdot m^{-2}$
t	Time	s
$t_{1/2}$	Half-time	s
T	Temperature	ºC
Tg	Glass transition temperature	ºC
Tm	Melting temperature	ºC
v	Volume	m^3
w	Weight	g
ΔT_{max}	Maximum temperature rise	ºC

Greek Letters

α	Thermal diffusivity	$mm^2 \cdot s^{-1}$
ρ	Density	$g \cdot cm^{-3}$
υ	Phonon velocity	$m \cdot s^{-1}$
σ	Standard deviation	
ϕ	Orientation parameter in Lewis and Nielsen's Model	
∅	Shape parameter in Hamilton's Model	

Indexes

a	Air
c	Continuous phase
ce	Mean of the new continuous phase
d	Discontinuous phase
de	Sum of all discontinuous phases
e	Effective
f	Filler
fl	Fluid
i	counter
m	Matrix
ref	Reference

List of Acronyms

ASTM	American Society for Testing and Materials
DSC	Differential Scanning Calorimeter
EDX	Energy Dispersive X-ray spectrometry
HTM	High Mould Temperature
IMDS	International Material Data System
LMT	Low mould temperature
PA	Polyamide
PBT	Polybutylene Terephthalate
SEM	Scanning Electron Microscopy
TGA	Thermogravimetric Analysis
HDT	Heat Deflection Temperature

1 Introduction

1.1 Framing and presentation of the work

The current technology development drives the demand for manufacturing innovation and development of new advanced materials that will outperform the traditional ones. The increasing concern for fuel consumption in the automotive industry has led to a greater focus on deploying lightweight materials in cars to reduce energy consumption. Thus, polymers have increasingly become a vital material in the automotive sector, leading to enhancements in performance, safety, and efficiency. Heat sinks efficiently move thermal energy from a heat-generating component to a surrounding fluid and prevent the device from permanent damage. Metals have conventionally been used in this application; however, their high density and low corrosion resistance are not optimal for electronic packaging applications. In this context, this dissertation arises from the possibility to replace metals with thermoplastic composites in heat sinks due to their low density, low cost and ease of manufacturing in complex geometries.

The applicability of these materials depends on their thermal, electrical, and mechanical properties to guarantee higher efficiency without compromising performance. Thus, fillers must be carefully chosen to induce properties according to the final application in the polymer matrix. Therefore, the main objectives of this dissertation are to strategically select different commercial injection grades and evaluate their processability, morphology and thermal behaviour. Thus, the focus is on the optimization of the injection parameters, mainly the mould temperature, and the investigation of the thermal conductivity in different regions of discs produced by injection moulding. The effect of mould temperature was analysed for the same material, maintaining constant all the remaining injection parameters. The thermal properties of injected discs were analysed by strategically selecting the measurements regions. Therefore, different positions relating to the injection point and to melt flow direction were analysed to evaluate the impact of differences in filler dispersion in the injection mould. The thermal conductivity was compared among different materials, and the morphology was investigated. Finally, theoretical models were used to predict thermal conductivity and were compared to the experimental data. The more accurate models were applied to predict the thermal behaviour of each material with different filler volume fractions.

The thermal diffusivity was determined using the laser flash method, which is considered the reference technique because it is the only method covered by an ASTM standard[1]. The thermal conductivity was indirectly determined using the measured thermal diffusivity, density, and specific heat capacity of the material obtained from a Differential Scanning Calorimeter (DSC). Scanning Electron Microscopy (SEM) with Energy Dispersive X-ray Spectrometry (EDX) and

Thermogravimetric Analysis (TGA) were performed to understand if the difference in conductivity in each position were related to differences in morphology and filler content. SEM images where analysed with an image processing software (ImageJ). All tests were performed according to ASTM standards.

1.2 Presentation of the company

This dissertation was developed at Bosch Car Multimédia Portugal, S.A., located in Braga, Portugal. The Bosch Group is a leading global supplier of technology and services. Its operations can be divided into four business sectors: Mobility Solutions, Industrial Technology, Consumer Goods, and Energy and Building Technology. This work was integrated in an innovation group whose focus is on mobility solutions and pursuing a new, safer, sustainable, and exciting vision of mobility.

1.3 Contribution of the author to work

The thermoplastic composites were produced by injection moulding at PIEP (Pólo de Inovação em Engenharia de Polímeros) and the samples were cut by the construction department at Bosch. SEM/EDX and TGA analysis were performed at Bosch with the help of other colleagues. Still at Bosch, density and thermal diffusivity measurements were performed by me. I conducted the DSC tests, using the equipment located in the LSRE-LCM facilities, at FEUP.

1.4 Organization of the dissertation

The body of this thesis is structured in six chapters. Initially, Chapter 1 introduces the subject of the work and contextualizes the main objectives. Chapter 2 presents a background and literature review, as well as concepts and definitions essential to understand this work. Chapter 3 presents details on constituent materials, fabrication, and characterization techniques of the test samples. In Chapter 4, all results are presented and discussed. Chapter 5 presents the general conclusions of the work. Finally, in Chapter 6, the thesis concludes with an overview of this research, mentioning whether the initial objectives were achieved as well as limitations and directions for future work.

2 Context and State of the art

2.1 Introduction

Polymers filled with thermally conductive fillers are emerging as a cost-effective solution to deal with thermal management issues, emphasizing the importance of thermal property analysis of engineering systems.

Polymer composites are multi-phase systems integrating reinforcing materials in a polymer matrix that result in synergistic properties unattainable by the individual constituents[2]. The primary purpose of the matrix is to hold all reinforcements together while protecting them, maintaining their orientation and keeping them separated[3]. The reinforcing material is designed to carry the load and provide the strength and stiffness required for structural applications but can also be added to perform other specific functions[4].

The demand for lighter and stronger materials has made composites an exciting choice for advanced applications. Notably, they are gaining attention in the automotive industry to replace metals to make lighter, safer, and more fuel-efficient vehicles. In general, composites are lightweight, easily mouldable to complex shapes and have good mechanical properties, such as high specific stiffness and strength, good fatigue resistance and low thermal expansion[5]. However, temperature limits, high material cost, damage susceptibility, manufacturing difficulties, low ductility and long development time are limiting factors to consider when designing with composites[6]. Moreover, polymers' intrinsic low thermal conductivity restricts their application in fields requiring efficient heat dissipation to avoid dielectric failures due to overheating. However, composites offer the great advantage of a flexible design, meaning that, in principle, the material can be tailor-made to meet specific needs, allowing to design different materials for each application[2]. The addition of thermally conductive fillers in polymeric matrices can provide heat-conducting paths through the composite, surpassing the difficulties associated with plastics in heat transfer applications[7].

The thermal behaviour of composites plays a critical role in their performance; therefore, accurate thermal measurements are essential. The thermal conductivity of a composite can be measured by experimental methods, while analytical equations are essential to predict it. Further understanding of the thermal behaviour of a composite system is essential for designing and developing thermally conductive polymers.

2.1 Composite materials in automotive applications

The automotive industry has seen a significant change in the types of materials employed in its manufacture, from the extensive use of metals in the 1950s to the current development of alternative advanced materials[8]. This shift can be attributed to increasing demands to produce lighter and more sustainable vehicles, with improved quality and performance, extend guarantees, fast production times and reduced costs.

While thermosetting plastics have good thermal stability, thermoplastics have several advantages that make them popular for automotive manufacturing, such as short processing cycles and the ability to be injection mouldable into complex geometries that would not be possible with other materials[9]. This results in more flexibility of design, ease of construction and assembly and reduction of design and manufacturing times[9]. They also allow the integration of functionalities and require little maintenance. Additionally, they exhibit superior mechanical and thermal properties over a wide range of conditions[10]. The increasing concern with fuel consumption and legislative and regulatory requirements regarding combating climate change is a driving force behind the significant effort to produce enhanced performance-to-weight ratio materials. The weight reduction leads to better car performances, increased fuel efficiency and reduced CO_2 emission. Thermoplastic composites present economic advantages because reducing finishing costs, design and manufacturing times results in higher productivity[9]. Figure 2-1 displays the current applications of thermoplastics composites in cars. Looking at the image, it is possible to see that polymeric materials have been applied in different components in cars. The PBT (Polybutylene terephthalate) and PA (polyamide) have been widely explored for automotive needs by doping these polymeric matrices with specific fillers, obtaining what is denominated by engineering plastics.

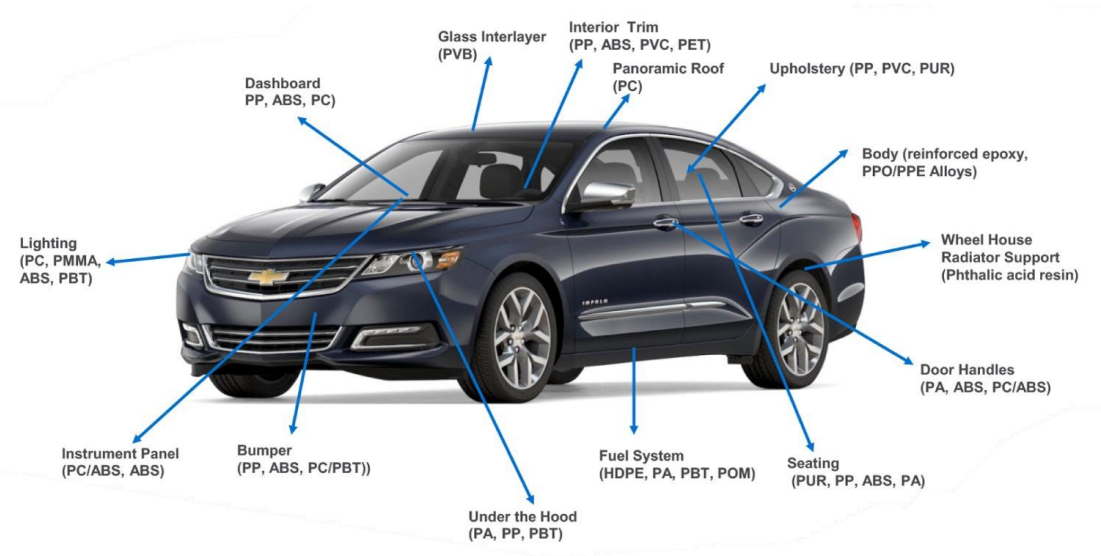


Figure 2-1 – Thermoplastic applications in car parts[11].

2.1.1 Heat sinks

Heat sinks are heat exchangers that support electronic devices by providing a path for heat dissipation and are vastly used due to their simplicity of fabrication, low cost, and reliability[7]. Metals are typically used as heat sink material due to their high thermal conductivity and mechanical resistance. However, the high density, electric conductivity and reduced corrosion and fouling resistances encourage the search and development of alternative materials[7]. Since there is a broad spectrum of matrix materials available and their properties can be adjusted by selecting appropriate fillers, conductive thermoplastic materials can be economical, lightweight alternatives for metallic ones in heat sinks. Figure 2-2 shows different heat sinks geometries designed for the optimization of thermal management. These geometries can be complex and difficult to reproduce using metals. However, thermoplastics allow for precise mass production through injection moulding.

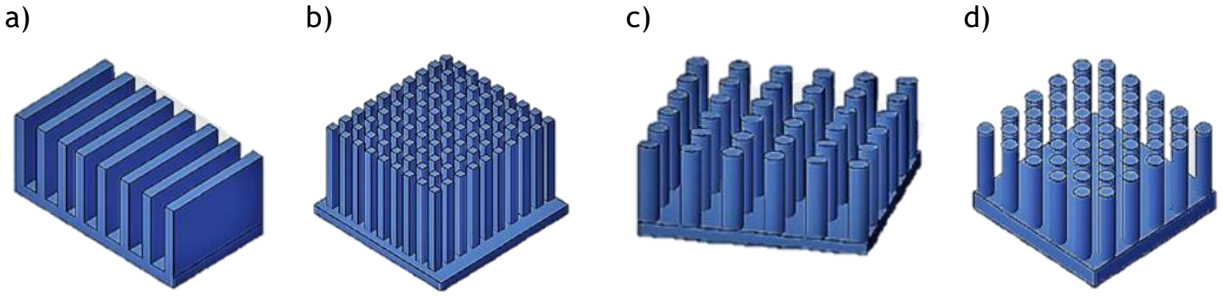


Figure 2-2 – Various Heat sinks: (a) Plate Fin Heat Sink, (b) Square Pin Fin Heat Sink, (c) Round Pin Fin Heat Sink-inline and (d) Round Pin Fin Heat Sink-Staggered[12].

2.2 Theory of thermal conductivity

Heat conduction of homogeneous solid materials is ruled by Fourier's Law, which states that the local heat flux is proportional to the negative local temperature gradient. For one-dimensional, steady-state heat conduction along the *x*-direction, the heat conduction rate can be represented by:

$$q = -k \frac{dT}{dx} \tag{2.1}$$

where q is the heat flux ($W \cdot m^{-2}$), k is the thermal conductivity of the material ($W \cdot m^{-1} \cdot K^{-1}$), $\frac{dT}{dx}$ represents the change in temperature across the thickness, and the negative sign indicates the temperature reduction from the hotter surface to the cooler surface ($K \cdot m^{-1}$).

Heat can be transmitted through solids via electrical carriers, as well as by lattice waves (phonons) or other excitations. A phonon is a quantum of vibrational mechanical energy associated with the lattice, corresponding to the vibration of atoms and molecules near their equilibrium position[13]. In metals, the heat is conducted mainly by electrical carriers, while in insulators and semiconductors, lattice waves are the dominant heat transporter[13]. Therefore, phonon thermal conduction is the dominant mechanism for most polymers. The Debye equation is usually used to calculate the thermal conductivity of polymers:

$$k = \frac{c_p \cdot v \cdot l}{3} \tag{2.2}$$

where c_p is the specific heat capacity per unit volume, v is the average phonon velocity, and l is the phonon mean free path. For amorphous polymers, l is an extremely small constant due to lattice imperfections, voids and impurities, which result in phonon scattering and, ultimately, low thermal conductivity[14]. In a multi-phase system such as a polymeric composite, scattering also occurs when phonons propagate through the interface of the different phases. Figure 2-3 represents the different factors hindering the establishment of conduction paths and leading to lower thermal conductivity.

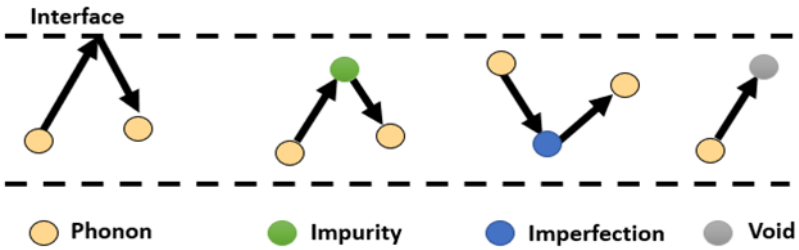


Figure 2-3 – Factors causing phonon scattering in polymers. Reproduced from[15].

Thermal conduction path, thermal percolation and thermoelastic coefficient theories are the currently accepted mechanisms for explaining thermal conduction in polymer composites[16]. These mechanisms are represented in Figure 2-4 and the main differences between them are reported below.

The thermal conduction path theory is the most widely accepted, stating that when the thermally conductive fillers are added to the polymer matrices, they form continuous networks that allow the conduction of heat[16]. These networks are marked in red in Figure 2-4 a).

The thermal percolation theory describes the sharp increase in thermal conductivity when the filler volume fraction exceeds a percolation threshold[17]. As represented in Figure 2-4 b), when

the filler loading is higher than this particular value, fillers come into contact with each other to form a network structure, while at low filler loadings, the composite's thermal conductivity is similar to that of a pure thermally insulating polymer matrix. However, most fillers are only 10 to 1000 times more thermally conductive than the polymer matrix[18]. Because the addition of conductive fillers creates more interfaces between the matrix and filler, the phonon scattering increases and causes thermal conductivity to decrease. Thus, the combination of the two factors may not allow for abrupt increases in thermal conductivity.

Thermal conductivity can be deemed as a thermoelastic coefficient in the phonon propagation[16]. This analogy is represented in Figure 2-4 c), demonstrating that thermal conductivity depends on the properties of the composites rather than on the transmission path. Filler and matrix are considered two distinct phases, and their ability to conduct heat is what influences the thermal conductivity of the composite. The difference in properties between the filler and the polymer matrix inevitably causes phonon scattering at the interfaces, which results in lower thermal conductivity and doesn't allow for an abrupt increase of filler loading.

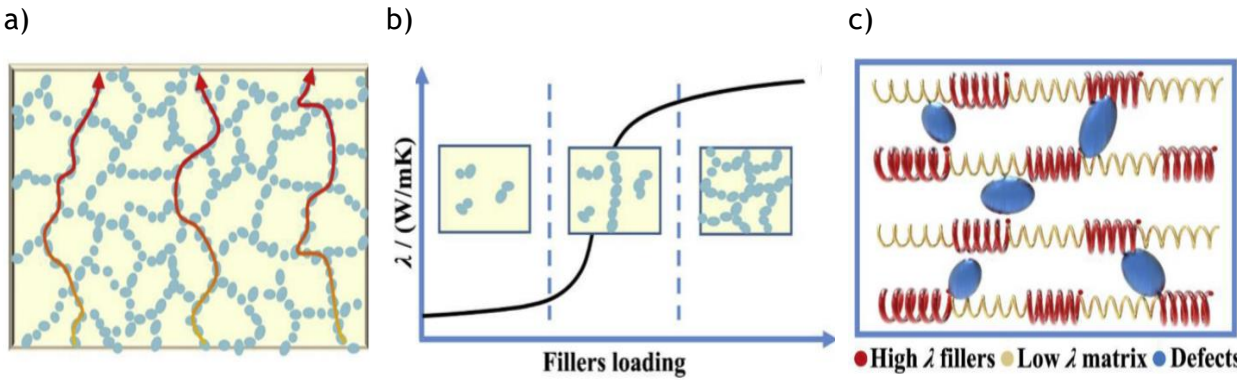


Figure 2-4 – (a) Thermal conduction paths in high fillers loading; (b) Percolation phenomenon; (c) Thermoelastic coefficient theory[18].

2.3 Factors affecting thermal conductivity of composite materials

Thermally conductive polymer composites can be produced by doping polymers with conductive fillers, with low preparation costs and simple processing. However, the resulting thermal conductivity is lower than theoretical predictions due to the thermal resistances associated with the polymer matrix, the thermally conductive fillers and the interfaces[18]. The following subchapters expound on nine factors affecting thermal conductivity in polymer composites, from the effects of the matrix (crystallinity, chain structure, orientation), filler (intrinsic thermal conductivity, loading level, shape, size and hybrid fillers) and interfaces (surface modification).

2.3.1 Crystallinity

Polymers have both crystalline and amorphous regions. Amorphous domains generally have low thermal conductivity (~0.2–0.3 $W \cdot m^{-1} \cdot K^{-1}$)[19], because the random orientation and disordered alignment of the molecular chains diminishes the mean free path for energy transport along chains. Because crystallization can increase the intrinsic order, semicrystalline polymers usually have higher thermal conductivity than amorphous ones[20]. This difference is demonstrated in Figure 2-5, where these materials are represented as a Newton pendulum. A classic ordered Newton pendulum (a) symbolizes a crystalline material, where the initial vibration (in red) is easily transferred to the opposite face without scattering. Conversely, a disordered pendulum (b) can symbolize an amorphous polymer, in which the initial kinetic energy is mainly transmitted to the atoms of the disordered structure, causing vibrations of each ball[21].

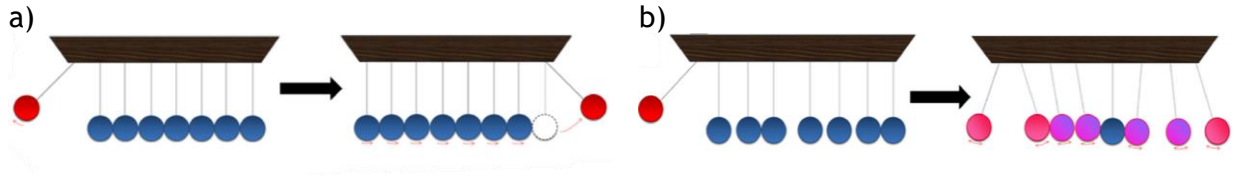


Figure 2-5 – Comparison by the Newton pendulum of thermal conductivity in (a) crystalline materials and (b) polymers[21].

2.3.2 Chain structure

Polymers with rigid backbones and π-conjugation can achieve high thermal conductivity because of the suppressed segmental rotation of the chains[22]. This can lead to strong intermolecular interaction and thus facilitate the formation of paths for heat conduction, ultimately resulting in higher phonon velocity[22] (Figure 2-6). Conversely, polymers with intrinsic segmental rotations have lower thermal conductivity due to increased disorder and phonon scattering. Chain branches also have that effect on thermal conductivity because of their rotation and disorder. Additionally, heavier atoms and weaker backbone bonds reduce the phonon velocity, resulting in lower thermal conductivity[22].

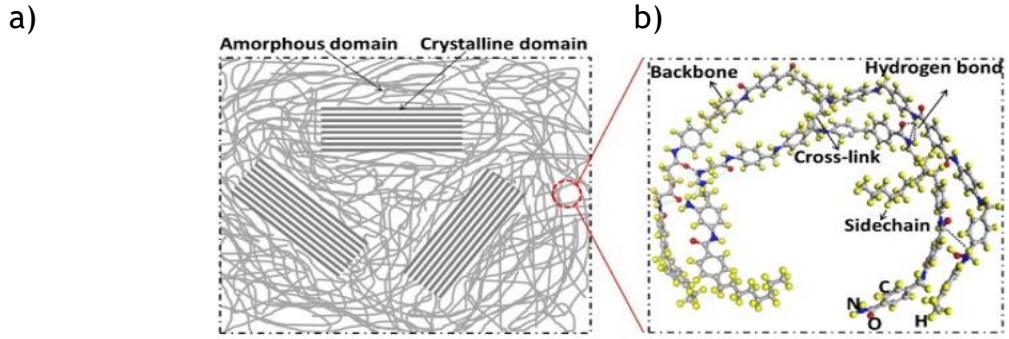


Figure 2-6 – Schematic of (a) the crystalline and amorphous domains of a polymer and (b) the structure of a polymer chain [23].

2.3.3 Orientation

During chain alignment processes, both crystalline and amorphous domains are orientated in the direction of an external force resulting in an improved thermal conductivity. This happens because heat carriers are more easily transported along straight chains, consisting of strong carbon-carbon covalent bonds, than between chains, consisting of weak van der Waals forces[19]. Thus, thermal conduction in polymers is inherently anisotropic because the value of thermal conductivity is much higher in the oriented direction. Figure 2-7 demonstrates how (a) high chain orientation facilitates heat transfer compared to (b) low chain orientation.

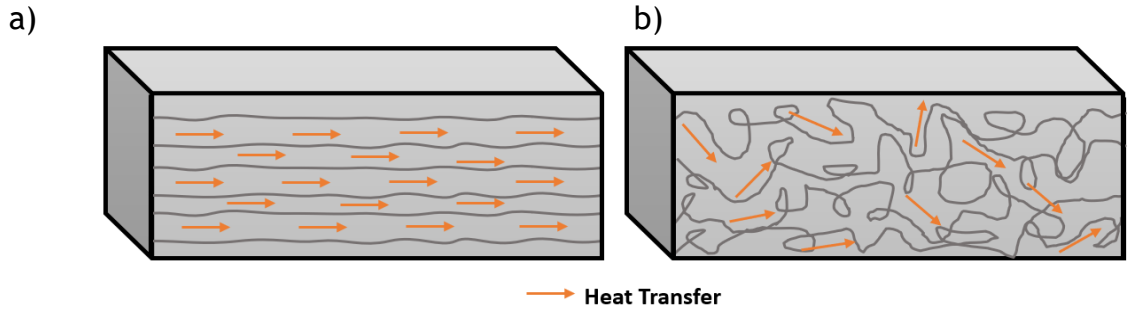


Figure 2-7 – Effect of molecular chain alignment on heat transfer on a polymer with (a) high chain orientation and (b) less chain alignment.

2.3.4 Filler intrinsic thermal conductivity

Thermally conductive fillers are one of the most critical factors affecting the thermal conductivity of polymer composites. There are three common types of thermally conductive fillers: metals, ceramic and carbon materials[24].

The thermal conductivity of fillers is primarily determined by the way heat transfers in filler particles. In general, fillers with purely phonon heat transfer mechanisms have lower thermal conductivity than those with both phonon and electron transfer because electrons move at higher speeds and are more resistant to dispersion[25]. Thus, metallic and carbon-based fillers have more significant thermal conductivity due to free electrons, making them very useful in applications where electrical insulation is not required, such as heat exchangers. Conversely, ceramic fillers are widely used as an electrically insulating method.

2.3.5 Filler loading level

In general, the thermal conductivity of composites increases with increased fillers loading[26]. When the loading is too low, it is difficult for fillers to form conductive pathways, which results in the ineffective enhancement of thermal conductivity. However, excessive loading can lead to agglomerations, which induces many problems such as stress concentration, a decrease of

the tensile strength, modulus and ductility of the material, processing difficulty and cost enhancement[27].

2.3.6 Filler shape

The filler shape has a significant influence not only on thermal conductivity but also on viscosity[28]. While filler loading above the percolation threshold is desired to achieve high thermal conductivity, this can cause an increase in viscosity and introduce processability problems[29]. Therefore, it is necessary to select the filler shape that can optimize both properties. Fillers with a high aspect ratio, either one- or two-dimensional, usually exhibit a lower filler percolation threshold to create a thermally conductive network, resulting in higher thermal conductivity[30]. Fillers with irregular shapes can cause friction during mixing or compounding, thus increasing the viscosity and reducing the processability[29]. Spherical fillers have high viscosity percolation threshold, meaning they can be incorporated into a polymeric matrix with high loading without significant change of viscosity[28].

2.3.7 Filler size

When the characteristic length, such as the thickness of a film, the diameter of a filament or the size of the fillers is comparable to the mean free path, the interface scattering becomes significant[31]. Thus, the thermal conductivity becomes size-dependent.

The smaller filler has a lower interparticle distance at the same particle loading and more chances to form thermal conductive paths, favouring thermal conductivity[27]. However, composites with smaller-sized fillers have a higher tunnelling effect and large interfacial area, causing phonon scattering and often leading to lower thermal conductivity[30,16].

Larger size thermally conductive fillers can reduce the filler/polymer interface, thereby reducing the interfacial thermal and percolation threshold resistances, leading to improved heat conduction[30]. However, the larger filler surface areas can substantially increase the viscosity and cause dispersion problems[16].

Particle size also strongly influences the distribution of filler composite since bigger particles settle down mostly, while the smaller fillers distribute mostly uniformly[32].

2.3.8 Hybrid fillers

Various fillers can be used to integrate all their advantages in a single composite. The combination of different fillers creates a symbiotic phenomenon, which is also known as the synergistic effect, that can significantly improve thermal conductivity[33].

A hybrid filler system can help form extensive thermally conductive paths by building bridges between fillers, increasing the packing density, and reducing overall filler loading, thus reducing the system viscosity[29].

Different sized thermally conductive fillers can be used together so that the smaller ones can fill the gaps of the bigger ones, thereby increasing the probability of formation of thermal conduction paths[29].

2.3.9 Surface modification

Polymer composites can suffer from poor dispersibility, leading to agglomeration and hindering phonon transport. Also, the introduction of thermally conductive fillers creates interfacial thermal resistances, originating from the mismatch of phonon spectra at the filler-filler and filler-matrix interfaces, causing phonon scattering[34]. This represents a bottleneck for the heat transfer across the interfaces, thus leading to a significant reduction in the thermal conductivity. Therefore, it is crucial to reduce the interfaces or improve the interfacial performance to enhance the thermal conductivity in polymer composites. Surface modification can manipulate and enhance the filler properties by addressing filler dispersibility and interfacial filler-matrix resistances[35].

The interfacial thermal resistance can be classified by thermal contact resistance or by thermal boundary resistance[35].

The thermal contact resistance is the most comprehensive quantity used to characterize interfacial heat transfer and can be defined as the temperature difference across an interface per unit heat flux[36]. While most surfaces seem flat, on a microscopic level, all of them possess micro asperities that diminish the contact area of two surfaces[36]. This mismatch in the contact area means a decrease in the amount of heat transferred, resulting in a decline in thermal conductivity, proportional to the value of thermal contact resistance at the interface.

Contrary to thermal contact resistance, thermal boundary resistance still occurs over atomically flat interfaces. Because of the differences in the electronic and acoustic properties of the contacting materials, the energy carriers of one material are deflected at its geometric boundaries[35]. When comparing the two types of interfacial thermal resistance, this one can be orders of magnitude more significant for nanoparticle-based materials and is much harder to model and control[35].

2.4 Injection moulding process

Injection moulding is one of the most widely used polymer processing methods for low-cost mass-producing plastic and plastic composite parts with complex geometry and high precision.

The injection moulding machine (Figure 2-8) transports, melts and pressurizes the polymeric composites fed into the machine in granular form. The material is plasticized, and the melt is concentrated at the front of the nozzle until the desired volume is achieved and is then forced into the tooling[37]. After the mould is filled, a hold pressure is applied to the melt to force more materials into the cavity and compensate for the shrinkage caused by the cooling of the melt within the cavity. When the product is cooled, the mould opens, and the part is ejected[37].

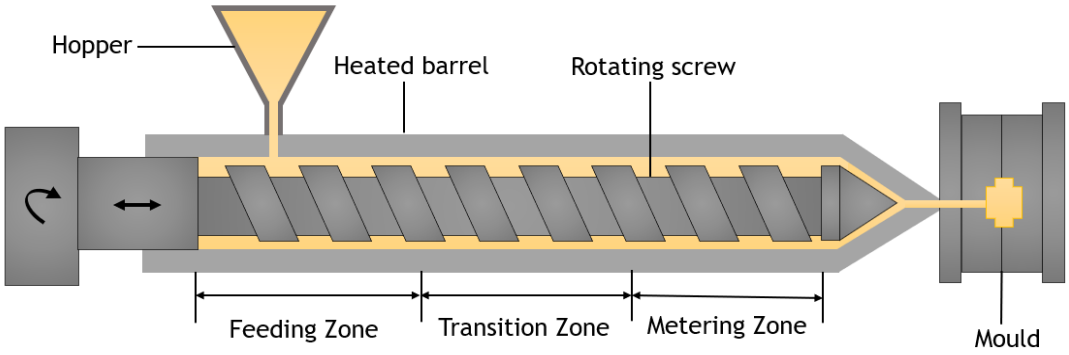


Figure 2-8 – Representation of the injection unit, including the hopper, rotating screw and the heated barrel.

Thermoplastic materials have non-Newtonian flow behaviour, more precisely shear thinning behaviour, meaning their viscosity decreases with increasing shear rates. Therefore, the higher the shear rate, the easier it is to inject polymers. The change in viscosity as a function of shear rate creates a fountain flow, represented in Figure 2-9 (a), where the melt in the flow channel's centre flows ahead of the melt at the walls[38]. During mould filling, the first material is injected into an empty melt flow channel fountains to the channel walls and, as additional material is injected, the most recent material advances to the flow front and continually fountains to the wall. The flow in the centre is considered laminar, and the flow along the channel wall is assumed to be zero. When the polymer is injected into a relatively cold mould, a thin layer of the melt is rapidly cooled at the cavity wall, immediately creating a frozen layer of the polymer[39]. Due to the rapid solidification, the fillers in the frozen layer can be highly orientated, mostly aligned along the flow direction, while in the centre of the flow the material has more time to relax and crystallize, although the shear flow also generates some orientation[39] (Figure 2-9 (b)).

When working with reinforced thermoplastics, it is difficult to maintain the not melted, oriented structure of fillers with the final product, primarily due to the required high processing temperatures. The fillers orientation is related to the flow direction in the mould, depending on the viscoelastic properties of the matrix and the geometric properties of the fillers. The degree of orientation and the dominant direction of the fillers change throughout the part,

resulting in anisotropy and different properties at different locations of the piece[40]. Thus, adding filler reinforcement to plastic parts creates challenges for structural analysis.

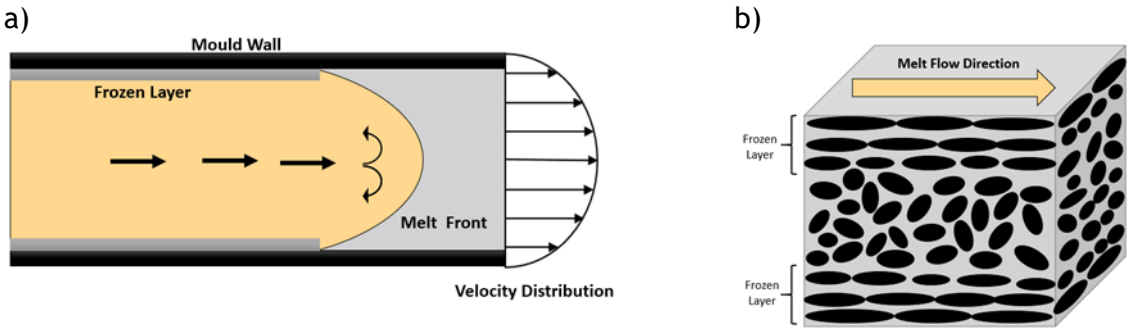


Figure 2-9 –Representation of (a) the fountain flow during injection moulding and (b) the profile injection-moulded parts made of polymer composites. Reproduced from[41].

As injection moulding is a complex process, several parameters can lead to different polymer microstructures and affect the moulded product quality.

The shear flow of the melt impacts filler orientation by aligning fillers with the flow direction. This results in a higher in-plane thermal conductivity than through-plane. While flow is affected more by shear-rate changes than by small temperature changes, the desired temperature needs to be controlled and held constant[37].

The mould temperature determines the cooling rate and how much stress is locked into the product, how much crystallization takes place in the mould and the surface finish of the moulded product[37]. Increasing the mould temperature delays the heat transfer from the melt to the mould walls, resulting in a decrease in viscosity of the melt and lower resistance to the flow. Thus, increasing mould temperature facilitates the flow inside the cavity and the rotation of the fillers during the packing stage, ultimately resulting in higher filler orientation[42].

2.5 Experimental approach for thermal conductivity measurements

Thermal conductivity and diffusivity are essential parameters to describe the heat transport properties of a material.

The laser flash is the reference method for thermal diffusivity because it is the only method covered by an ASTM standard[1]. The measurement is done by irradiating the front of the sample with a single pulse from a laser source and detecting the corresponding temperature rise on the back surface as a function of time. The laser flash technique uses a laser pulse to eliminate the problem of the thermal contact resistance while minimizing the heat losses by making the measurements in a time short enough to avoid significant cooling because convection is negligible. This method also allows for easy sample preparation, fast measurement times, small

sample dimensions (from 6 mm to 25.4 mm) and high accuracy (3 % for thermal diffusivity and 5% thermal conductivity)[43].

From the thermogram, thermal diffusivity can be calculated using Parker's formula:

$$\alpha = \frac{138\ d^2}{t_{1/2}} \tag{2.3}$$

where d is the sample's thickness (mm), and $t_{1/2}$ (s) is the time necessary for the signal to reach 50 % of its maximum value.

A thermal diffusivity model can be fit to the time-dependent temperature rise. Thermal conductivity, k ($W \cdot m^{-1} \cdot K^{-1}$), can be expressed by the following equation:

$$k = \alpha \cdot \rho \cdot c_p \tag{2.4}$$

Where α is the thermal diffusivity ($mm^2 \cdot s^{-1}$), ρ is the density ($g \cdot cm^{-3}$), and c_p is the specific heat capacity ($J \cdot g^{-1} \cdot K^{-1}$) under constant pressure. Because the parameters are temperature dependent, a measurement of these properties in dependence of the temperature is necessary for the characterization of the material.

2.6 Theoretical approach for thermal conductivity predictions

The increasing use of composites for various applications emphasizes its relevance in the thermal property analysis of an engineering system to determine the feasibility of a composite for use in electronic packaging. While experimental methods can measure the thermal conductivity of composites, theoretical and empirical correlations can be used as a preliminary method for evaluating their potential and predicting their behaviour. Although the predictions may not be precise, micromechanical models can be applied to determine if the properties will be favourable, thus reducing the unnecessary and time-consuming likelihood of failed experimental work.

The fundamental models to predict the thermal conductivity of polymer composites are Series, Parallel, and Geometric Mean models[44]. The rule of mixtures is the most widely used method of approach to estimate the modulus and strength of filler-reinforced composites, based on the weighted contributions from the filler and the polymer matrix. The parallel and series rule of mixtures allows to determine the thermal conductivity of composites based on the direction of heat flow concerning the fillers and act as the theoretical upper and lower bounds for thermal conductivity, respectively. In general, the actual thermal conductivity lies between the two[44]. The series model considers a case where the fillers are fully interconnected, forming an internal network structure, while in the parallel model, each particle is assumed to be an isolated entity[44]. The geometric mean model combines the parallel and series models, assuming an equal

proportion of each arrangement. This model is dependent on the weighted average of the filler and matrix materials and has no physical basis [44].

Parallel Model $$k_e = k_f\, v_f + (1 - v_f)\, k_m \quad (2.5)$$

Series Model $$\frac{1}{k_e} = \frac{v_f}{k_f} + \frac{(1 - v_f)}{k_m} \quad (2.6)$$

Geometric Model $$k_e = k_f^{v_f}\, k_m^{(1-v_f)} \quad (2.7)$$

Where k_e, k_f and k_m are the effective, the fillers and the matrix thermal conductivity, and V_f is the filler volume fraction. Other theoretical models for two-phase mixtures are presented in Table 1.

Table 1. Theoretical models for transverse effective thermal conductivity on two-phase mixtures.

Author	Model	Notes
Maxwell[44]	$k_e = k_m \left[\frac{k_f + 2k_m + 2\,V_f\,(k_f - k_m)}{k_f + 2k_m - V_f\,(k_f - k_m)}\right]$	• Fillers are grouped at the centre of the cube block of the composites • Low particle content, isolated existence, no interaction
Bruggeman[44]	$1 - V_f = \left[\frac{k_f - k_e}{k_f - k_m}\right]\left(\frac{k_m}{k_e}\right)^{1/3}$	•Randomly dispersed, isolated, spherical particles • More accurate at higher filler concentrations
Cheng and Vachon[44]	For $k_f > k_m$ $\frac{1}{k_e} = \frac{1}{\sqrt{C\,(k_m - k_f)\,[k_m + B\,(k_f - k_m)]}}$ $\ln\frac{\sqrt{k_m + B\,(k_f - k_m)} + \frac{B}{2}\sqrt{C\,(k_m - k_f)}}{\sqrt{k_m + B\,(k_f - k_m)} - \frac{B}{2}\sqrt{C\,(k_m - k_f)}} + \frac{1 - B}{k_m}$ Where $B = \sqrt{\frac{3}{2}V_f} \qquad C = -4\sqrt{\frac{2}{3V_f}}$	• Assumes the discontinuous phase has a parabolic distribution
Lewis and Nielsen[44]	$k_e = k_m \left[\frac{1 + A\,B\,v_f}{1 - B\,v_f\,\psi}\right]$ Where $B = \frac{\frac{k_f}{k_m} - 1}{\frac{k_f}{k_m} + A} \qquad \psi = 1 + \left(\frac{1 - \Phi m}{\Phi_m^2}\right) v_f$	• Accounts for particle shape, size, and packing • A and φ_m vary for different shapes and orientation

The analysis of three or more phase mixtures is more complicated than the two phase-case because it is challenging to describe the phase distribution. There is still a knowledge gap regarding filled polymer composites since most studies report for single filler composites without considering the synergetic effects of two or more different types of fillers on the thermal properties. Theoretical models for three or more phase mixtures are shown in Table 2.

Table 2. Theoretical models for transverse effective thermal conductivity on three- or multi-phase mixtures.

Author	Model	Notes
Hamilton[45]	$k_e = k_m \left[\frac{1 - \sum_{i=2}^{m} \frac{v_i \, (\emptyset_i - 1) \, (k_m - k_i)}{k_i + (\emptyset_i - 1) \, k_m}}{1 + \sum_{i=2}^{m} \frac{v_i \, (k_m - k_i)}{k_i + (\emptyset_i - 1) \cdot k_m}} \right]$	• If all the discontinuous phases are presumed to be spherical particles, $\emptyset_i$ = 3
Budiansky[45]	$\sum_{i=1}^{n} \frac{v_i}{\frac{2}{3} + \frac{1}{3} \frac{k_i}{k_e}} = 1$	• For a mixture of at least N-1 isotropic constituents, assuming they are roughly spherical
Cheng[45] Case 1 k_{d1}/k_C >100 k_{d2}/k_C >100	$k_e = \frac{k_c}{1 - B_e}$ Where $B_e = \sqrt{\frac{3}{2} V_{de}}$	• k_{d1} and k_{d2} are the thermal conductivity of the first (higher content) and second discontinuous phases, respectively • k_c is the thermal conductivity of the continuous phase • V_{de} is the sum of all discontinuous phases volumes
Cheng[45] Case 2 k_{d1}/k_C > 100 k_{d2}/k_C >1	$k_e = \frac{k_{ce}}{1 - B}$ Where $B = \sqrt{\frac{3}{2} V_{d1}}$	• The new continuous phase is the sum of the original continuous and the second discontinuous phase • k_{ce} is the mean thermal conductivity of the new continuous phase
Cheng[45] Case 3 100 > k_{d1}/k_C > 1 100 > k_{d2}/k_C	$k_e = \frac{k_{ce}}{1 - B}$ Where $B = \sqrt{\frac{3}{2} V_{dx}}$	• New continuous phase = original continuous phase + one of the discontinuous phases • V_{dx} is the volume fraction of the discontinuous phase not included in the new continuous phase
Cheng[45] Case 4 k_{d1}/k_C < 1 and/or k_{d2}/k_C < 1	$k_e = \frac{k_{ce}}{1 - B}$ Where $B = \sqrt{\frac{3}{2} V_{dx}}$	• New continuous phase = original continuous phase + one of the discontinuous phases • V_{dx} is the volume fraction of the discontinuous phase not included in the new continuous phase

3 Materials and Methods

3.1 Material Selection

The material from which heat sinks are constructed is one of the most critical parameters for their performance. This application requires a cost-effective alternative to traditional heat management parts with service temperatures between -40 ºC and 85 ºC and heat deflection temperatures at 1.8 MPa superior to 150 ºC. The focus of this material selection is to choose material combinations that allow for thermal conductivity values superior to 5 $W \cdot m^{-1} \cdot K^{-1}$ through-plane and 20 $W \cdot m^{-1} \cdot K^{-1}$ in-plane. After comparing the cost, thermal conductivity and service and heat deflection temperatures of polymers, PA6, PA6,6 and PBT were selected for the matrix. Figure 3-1 shows the synthesis reaction of the chosen polymers.

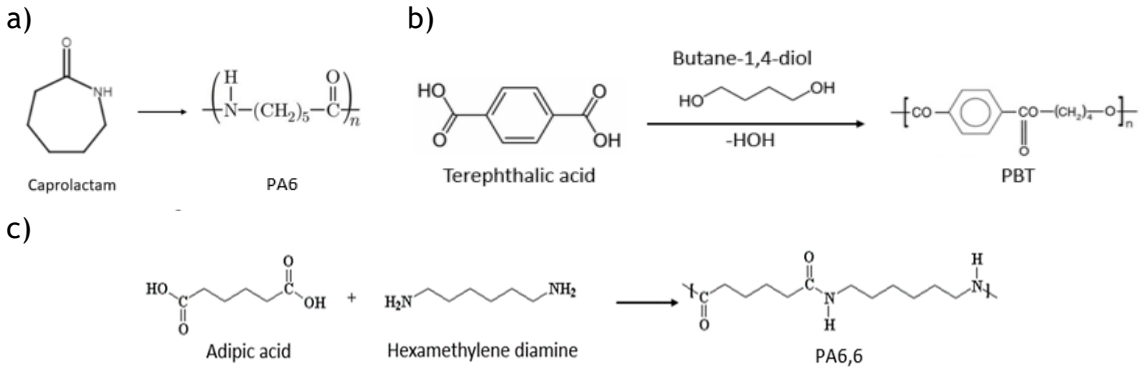


Figure 3-1 – Synthesis of (a) PA6, (b) PBT and (c) PA6,6.

The presence of amide groups in PA generates hydrogen bonding between the adjacent chains, which results in a three-dimensional network structure that provides strong bonds between the molecules[46] (Figure 3.2 (a)). This network structure results in a combination of good mechanical performances, high impact strength, good heat resistance, exceptional fatigue properties and chemical and abrasion resistance[47]. However, they absorb substantial amounts of water when exposed to humidity. The water molecules can form polar bonds with the amide groups due to their inherent hydrophilicity and can disrupt the hydrogen bonds between the PA chains[46] (Figure 3.2 (b)). This causes plasticization of the material, leading to more mobility of the chains and meaningful changes in the mechanical behaviour[47]. Moreover, the presence of water in PA can introduce significant internal stresses, reduce mechanical strength and stiffness, and lead to extensive chemical degradation of the polymer[46,47].

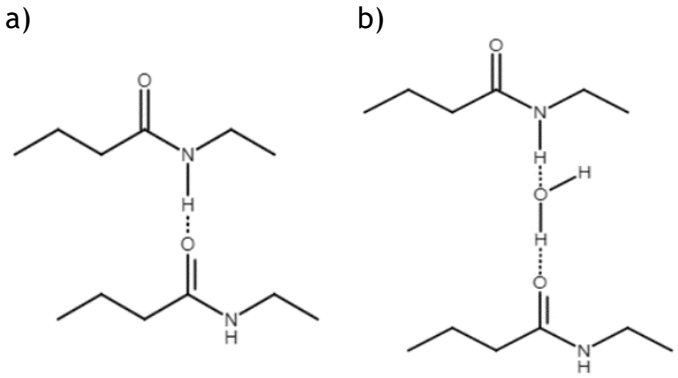


Figure 3-2 – (a) Hydrogen bonding between adjacent PA chains; (b) A possible water absorption mechanism and disruption of the H-bonded bridges.

Because of these disadvantages, Polybutylene Terephthalate (PBT) was also used in this work. PBT absorbs minimal amounts of humidity, representing an essential advantage over polyamides in terms of dimensional and electrical stability because the mechanical and electrical properties are constant and independent of the condition of the material. Additionally, the polymer displays great mechanical strength and toughness, high heat distortion and continuous use temperature (140 °C), fast crystallization rates, and short processing cycle times in injection moulding[48].

To induce thermal conductivity, the fillers used in this research include carbon-based fillers, namely carbon fibre, carbon black and graphite, and mineral powder and triiron tetraoxide. Four different thermoplastic composites with a combination of these matrixes and thermally conductive fillers were chosen for this work. The composition of each polymer composites was assessed by IMDS (International Material Data System) and is summarized in Figure 3-3.

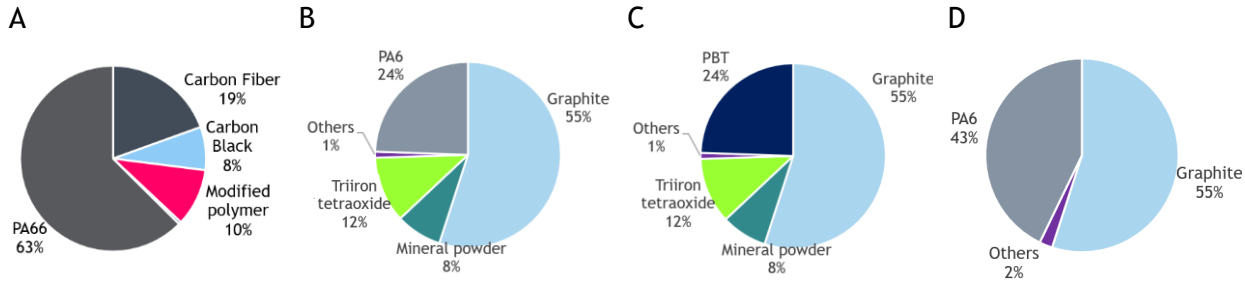


Figure 3-3 – Composition off the thermoplastic composites studied.

Material A is considered for electrical applications, while materials B, C and D are thermally conductive. By analysing their composition, it is noticeable that the thermal properties are mainly induced by the adition of graphite to the polymeric matrices (material B, C and D). Material B and C only differ in the matrix material, to allow for the evaluation of their influence on thermal conductivity.

3.2 Injection Moulding

The injection moulding experiments were conducted on an industrial injection-moulding machine (Engel ES200V/45VT-ELAST, Engel, GmbH) with a mould with 60 mm diameter and 2 mm thickness. The barrel zones and the mould were set to various temperatures depending on the material used. All masterbatch formulations were dried for 8 h at 80 ºC to ensure no residual moisture would affect the injection moulding process. The injection pressure was defined as 200 bar to achieve an injection rate of 60 $mm \cdot s^{-1}$. The screw speed was kept at 20 rpm, the backpressure at 10 bar and the cooling time at 10 s. To understand the effect of the mould temperature, samples of material B, C and D were injected twice, first at a lower mould temperature (B-LMT, C-LMT and D-LMT) and after at high mould temperature (B-HMT, C-HMT and D-HMT). Table 3 lists the temperatures during the process, according to the processability window indicated by the manufacturer.

Table 3. Temperatures during the injection moulding process.

Sample	Feeding Zone	Transition Zone	Metering Zone	Nozzle	Mould
A	280	290	310	290	100
B-LMT	250	270	290	280	70
B-HMT	250	270	300	290	110
C-LMT	250	270	290	280	70
C-HMT	250	270	300	290	110
D-LMT	240	270	290	280	100
D-HMT	250	290	310	300	120

3.3 Characterization Techniques

3.3.1 Experimental approach

The experimental work was initially defined to find the best method to guarantee an effective approach in achieving the research goals. Figure 3-4 shows a diagram of the steps followed in this experimental work. The thermal diffusivity was measured with the LFA to measure thermal conductivity, followed by the density and the specific heat (by LFA and DSC). This study was made for different measuring regions and different mould temperatures. Since these parameters can be affected by filler dispersion, anisotropy and filler loading, the samples were characterized by SEM/EDX, image processing and TGA. The following subchapters describe each technique in more detail.

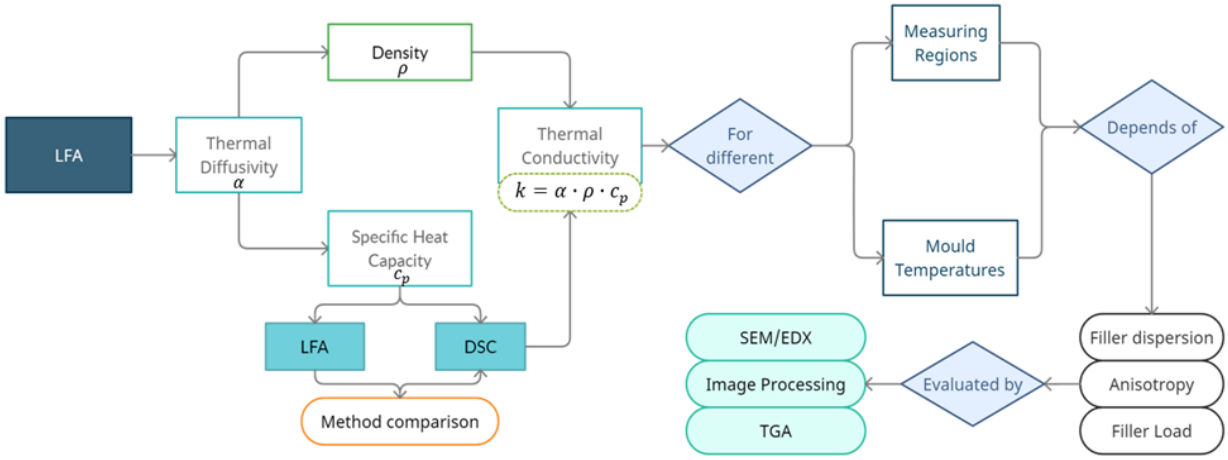


Figure 3-4 - Diagram of the steps followed in the experimental work.

3.3.2 Sample Density Determination

Individual sample density was measured with an Archimedes set (PBS-A03/A04, KERN & Sohn GmbH, shown in Figure 3-5 (a)), per ASTM standard D-792[49].

Archimedes' principle states that the buoyancy force exerted on an immersed object is equal to the weight of the fluid displaced by the object. Demineralized water was used as the auxiliary liquid. The balance was initially tared, and both the weights of the sample in air, positioned in the top holder, and submersed in the auxiliary fluid, in the bottom suspended holder (as presented in Figure 3-5 (b)), were measured, assuring that no bubbles adhered to the sample.

The weight of the displaced fluid exerts an upward force on the scale and produces a negative reading, which was recorded. The sample density (ρ) can be calculated using the following equation:

$$\rho_{sample} = \frac{w_a}{w_a - w_{fl}} \cdot (\rho_{fl} - \rho_a) + \rho_a \qquad (3.1)$$

where w_a and w_{fl} are the weight of the sample (g) in air and fluid, respectively, and ρ_a and ρ_{fl} are the density of the sample ($g \cdot cm^{-3}$) in air and fluid, respectively.

All samples were dried for 24h at 100 ºC to guarantee no residual water would influence the results of the following procedures.

a) b)



Figure 3-5 – a) Archimedes set for density measurement and b) representation of steps for measurement, with the samples in the top and bottom holder[50].

3.3.3 Laser Flash Analysis

The thermal diffusivity and specific heat capacity were measured using the LFA 467 HyperFlash® apparatus by NETZSCH. Both tests were performed according to ASTM testing standards (E1461, the Standard Test Method for Thermal Diffusivity by the Flash Method, and ASTM E1461, the Standard Test Method for Thermal Diffusivity by the Flash Method).

Four different square samples with 10 mm side length were cut from different positions in the disc compounded by injection moulding to measure the through-plane diffusivity, which is perpendicular to injection direction. The samples have 2 mm thickness because while at higher temperatures, thinner specimens are desired to minimize heat loss corrections. However, they should be thick enough to represent the test material (in the 1 to 6 mm range)[51]. Three of the samples were cut in the same line from the injection point to the other extremity, and the fourth one was cut from the centre on the left of the disc. To measure the in-plane diffusivity, parallel to the filler orientation direction, samples of 10x2 mm^2 were cut from the disc centre and individually rotated 90 degrees. After carefully cleaning the samples with isopropyl alcohol, a thin, uniform layer of graphite was applied to both faces to reduce their reflectability and improve their capability to absorb the laser's energy. Each sample was placed in the appropriate sample holder. The in-plane measurement requires the assembly of the separate cut samples in the laminate sample holder. The preparation process is demonstrated in Figure 3-6.

To determine the specific heat, pyroceramic was used as reference material, with the same dimensions, coating, and test conditions as the samples.

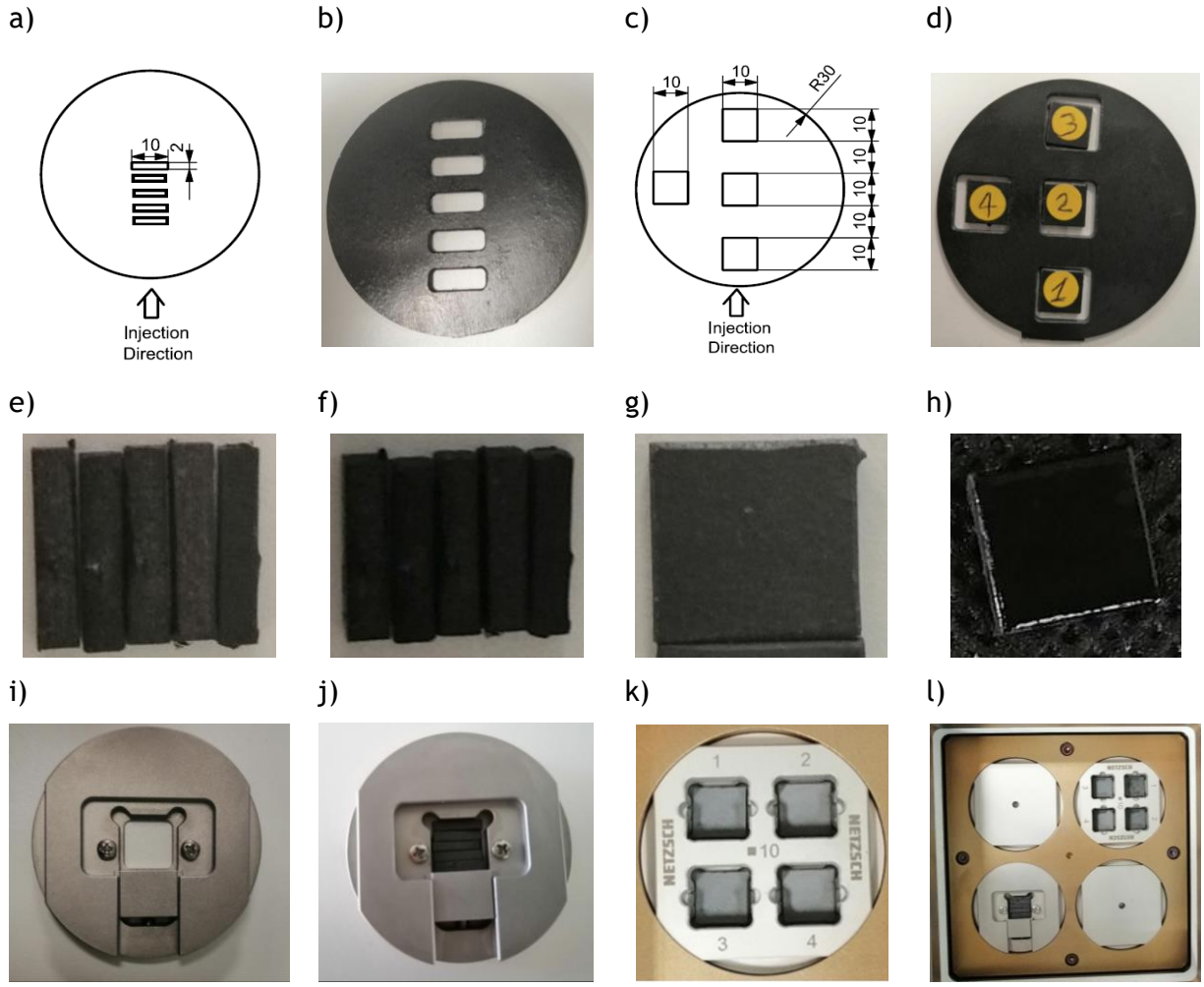


Figure 3-6 – Sample cutting: a) and b) for in-plane and c) and d) for through-plane measures; deposition of graphite layers: e) before and g) after for in-plane and g) before and h) after for through-plane measures; Sample assembly: i) and j) in-plane, k) through-plane and l) total.

To initiate the tests, first it is necessary to manually pour liquid nitrogen into the receptacle to manage the cooling of the furnace. The specifications of each sample were recorded into the Laser Flash System, such as the material, type of coating, thickness, size, and density at the reference temperature. Three shots were performed for each sample at temperatures ranging from 35 ºC to 130 ºC, including the automotive temperature limit of 85 ºC. Before starting a measurement, it is necessary to change the main gain and duration for each sample at each temperature to guarantee that the duration time is approximately 10 half times, $t_{1/2}$, and the maximum temperature rise (ΔT_{max}) is around 2/5 of the total horizontal area displayed in the measurement window, which results in the measuring curve being below the limits shown in the measuring window (Figure 3-7). Standard algorithms were used to correct heat losses through radiation during measurements.

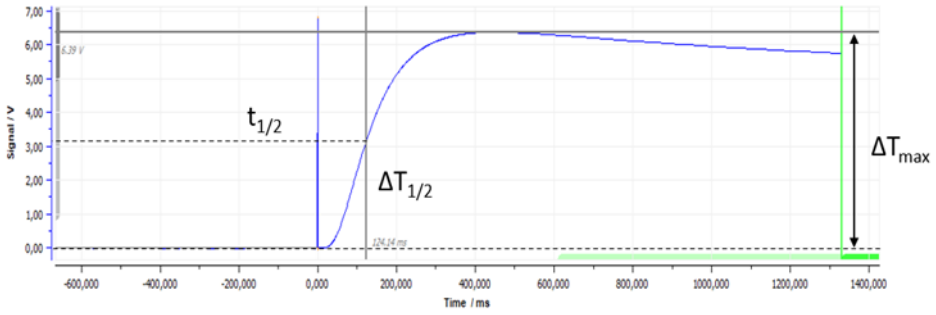


Figure 3-7 - LFA measuring windows and different parameters.

3.3.4 Differential Scanning Calorimetry

According to ASTM E1461, the Laser Flash is applicable to determine the specific heat capacity of primarily homogeneous isotropic solid materials[51]. Since this isn't the case for testing samples, the specific heat was measured using Differential Scanning Calorimetry (DSC), following testing standard ASTM E1269[52].

DSC is a thermoanalytical technique widely used to study the thermal behaviour of different types of materials. This method measures the difference in the amount of heat required to increase the temperature of a sample and reference as a function of temperature[52]. To calculate the specific heat of an unknown material, DSC requires the ratio method. It is necessary to measure the heat flux of the baseline, the specimen, and a reference (synthetic sapphire). The specific heat capacity is calculated using the ratio method as follows:

$$c_p = \frac{m_{ref} - m_{empty\ crucible}}{m - m_{empty\ crucible}} \cdot \frac{D}{D_{ref}} \cdot c_{p,ref} \qquad (3.2)$$

where c_p and $c_{p,ref}$ are the specific heat capacity of the sample and the sapphire standard, respectively ($J \cdot g^{-1} \cdot K^{-1}$); m, m_{ref} and $m_{empty\ crucible}$ are the mass of the unknown sample, the reference and the empty crucible, respectively (g); D is the vertical displacement between the baseline and the sample DSC thermal curves at a given temperature (W) and D_{ref} is the vertical displacement between the baseline and the sapphire DSC thermal curves at a given temperature (W). The ratio method can be calculated from the DSC curve as presented in Figure 3-8

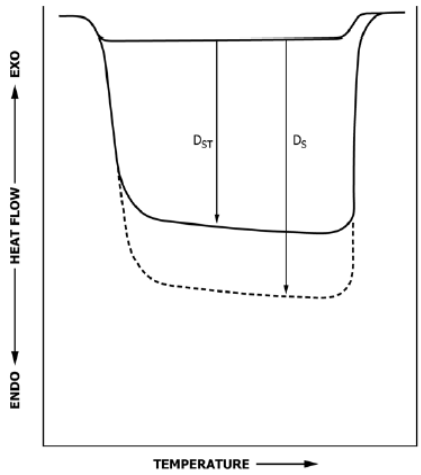


Figure 3-8 – DSC curves of standard and unknown Specimens[52].

The calorimeter used in this work was the STA 409 PC Luxx®, manufactured by NETZSCH (Figure 3-9 (a)). Each specimen was broken using uncontaminated pliers, and portions from various parts of the disc samples were removed to ensure a representative specimen for the determination. The initial baseline run was performed by placing two empty crucibles in the designated location on the heat flux sensor. The baseline corrects the contact resistance added by the crucible containing the samples during testing, hence increasing the accuracy of the results. The crucibles were heated to the final temperature of 150 ºC at a rate of 20 °C·min^{-1} in a nitrogen atmosphere (20 cm^{-3}·min^{-1}) and held isothermally while the calorimeter recorded the thermal curve. Following the baseline run, the calorimeter testing chamber was cooled to ambient temperature. To start the sample testing, the empty crucible on reference location was first weighted and tared, then was replaced with the sample, making sure to fill 3/4 or less of the total capacity, as shown in Figure 3-9 (b). A minimum of three runs was performed for every material.

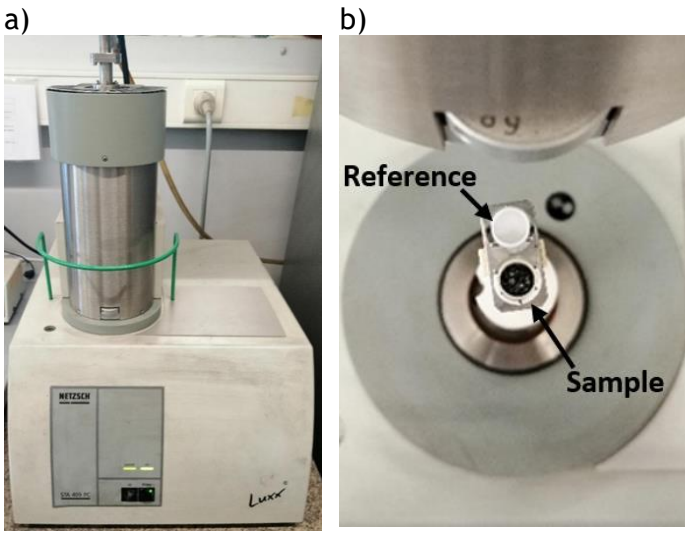


Figure 3-9 – a) STA 409 PC Luxx®, NETZSCH, used for DSC measurements; b) Crucible placed on the heat flux sensor.

3.3.5 Scanning electron microscopy and Energy Dispersive X-ray spectroscopy

Scanning electron microscopy (SEM) is a powerful method to characterize the surface features and evaluate the morphological changes and the dispersion of fillers within the matrix from the injection point to the opposite side of the samples. Energy Dispersive X-ray spectroscopy (EDX) is a powerful tool for forensic purposes, allowing for examining materials considering their morphology and elemental composition. Moreover, the obtained results can be evaluated by using suitable methods of chemometric analysis to determine the chemical composition of the materials. Polymer-filler morphology was obtained by a Hitachi FlexSEM 1000 scanning electron microscope and Bruker Quantax 80 detector EDX (Figure 3-10 (a)). The samples were fractured using liquid nitrogen to obtain an accurate representation of the material's morphology, as shown in Figure 3-10 (b)–(d). The freezing before fracturing produces a brittle sample and prevents the distortion of the surface for a clean cut and more accurate analysis.

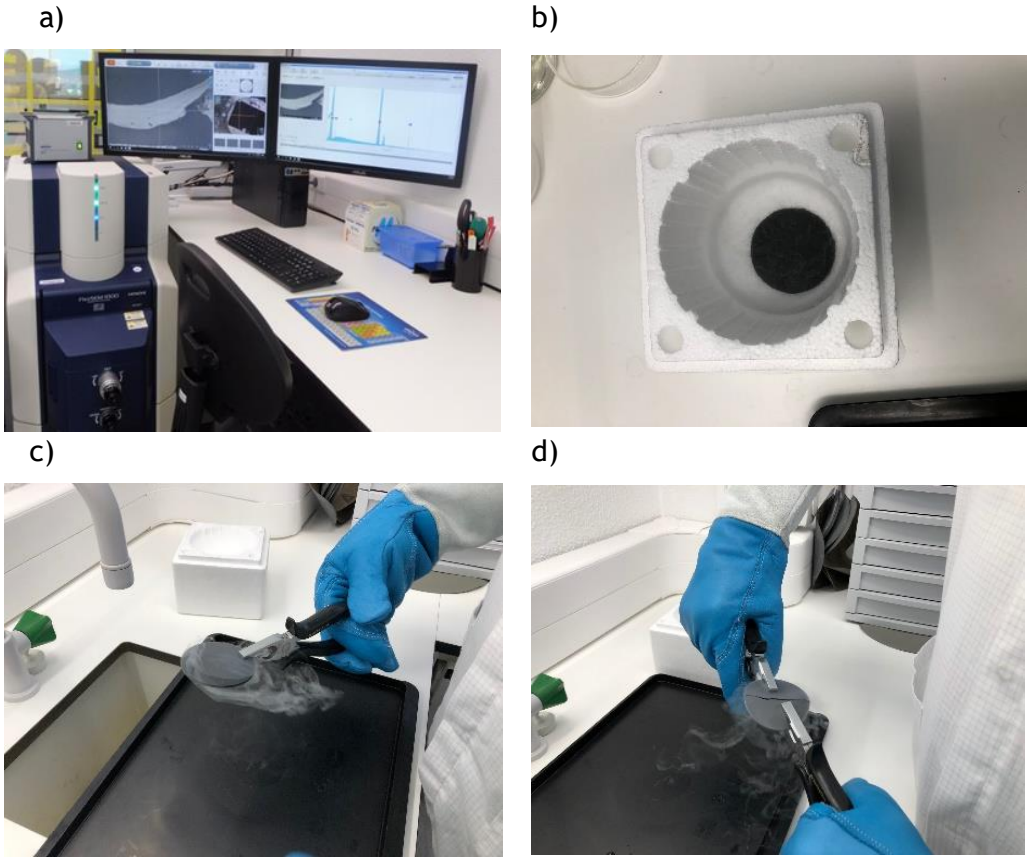


Figure 3-10 – a) Hitachi FlexSEM 1000 SEM; Sample preparation: b) Sample in liquid nitrogen, c) Sample after freezing and d) Sample cutting.

3.3.6 Image processing

The image processing program ImageJ was used to take advantage of the strong contrast between fillers and polymer matrix in the images previously obtained by SEM. A threshold was set so that pixels with higher intensity values than the threshold were separated from the background and identified as fillers. However, the results can be very sensitive to the chosen threshold, so manual thresholds could alter the interpretation of the data. To avoid this, the automated threshold determination models provided by the software were used.

3.3.7 Thermogravimetric Analysis

Thermogravimetric analysis (TGA) is a thermoanalytical technique that allows determining the quantity and the frequency of the weight variation of samples as a function of temperature and time in a controlled atmosphere[53]. This method was performed on Hitachi STA7200 equipment to investigate the differences in compositional properties in each position of the samples. The method has been recognized as reliable and was performed in accordance with ASTM E11310[53]. The disc samples were fractured using pliers (Figure 3-11), and representative parts of the different positions were cut, placed on the platin pan and weighed, subjected to a nitrogen flow of 200 $cm^3 \cdot min^{-1}$ and carbonized with a linear heating rate of 20 $^\circ C \cdot min^{-1}$ up to a final temperature of 800 ºC.

a) b)

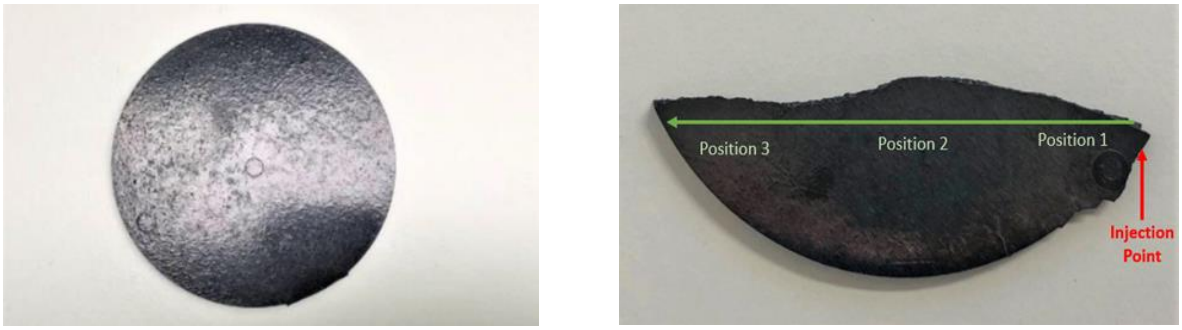


Figure 3-11 – Sample a) before and b) after breaking for TGA measurements.

4 Results and Discussion

In this chapter, all the results obtained in the tests previously described will be presented and discussed.

4.1 Thermal diffusivity

The laser flash method was used to measure the thermal diffusivity of the same materials with different mould temperatures and of parts cut from different regions of the same original sample. The thermal diffusivity of the thermoplastic composites was measured between 35 °C and 130 °C, including the automotive limit of 85 °C. The results are an average of at least three measurements, each consisting of an average of three shots. Figure 4-1 and Figure 4-2 display temperature dependence of the through-plane and in-plane diffusivity, respectively. To simplify the analysis of this thermal behaviour, the results are shown for position 2 (centre of the disc).

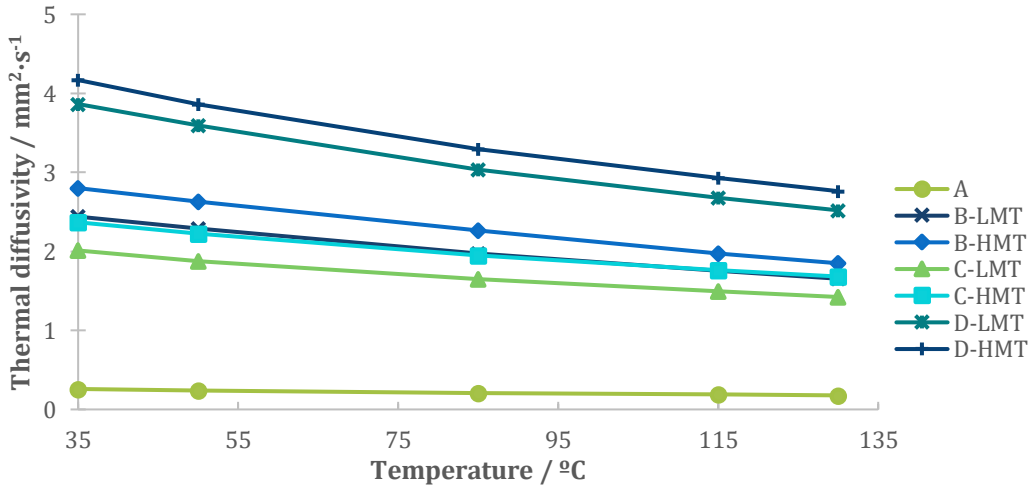


Figure 4-1 - Through-plane thermal diffusivity for position 2.

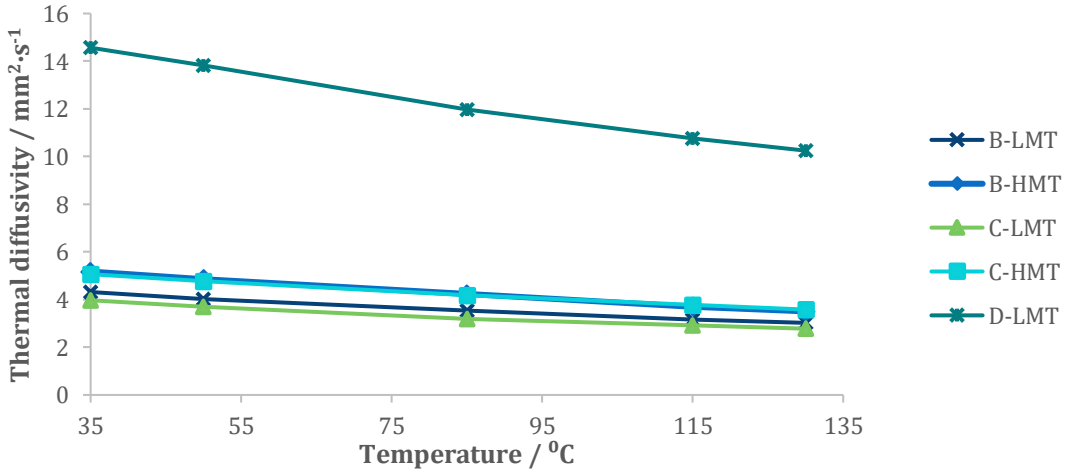


Figure 4-2 - In-plane thermal diffusivity for position 2.

In all cases, thermal diffusivity decreases with increasing testing temperatures. The increase in molecular and structural vibrations leads to an increase in phonon dispersion, which results in a significant reduction of the mean free path[54]. Since thermal diffusivity is directly connected to the mean free path, as per equation (2.2), this reduction leads to a decrease in thermal diffusivity. The least promising results were obtained for Material A, which was expected since it is marketed as an electrical material. For the thermal materials, Material D has the highest thermal conductivity, both in-plane (only D-LMT was measured) and through-plane (D-HMT). C-LMT has the lowest values both in-plane and through-plane.

4.2 Specific Heat Capacity

According to the Standard Test Method ASTM E1461, the LFA method should only be applied to primarily homogeneous isotropic solid materials[51]. Thus, DSC is the appropriate method for this determination. However, the LFA method only requires the measurement of one additional reference sample to use the comparison method and the LFA software automatically detects the best model fit. In comparison to DSC, LFA simplifies and accelerates the process of determining thermal conductivity. To understand the applicability of this method and the significance of the induced error, Table 4 presents the results obtained for both measurements, as well as the standard deviation and the relative error between the two methods.

Table 4. Specific heat capacity calculated by LFA and DSC.

Sample	Temperature (°C)	Cp LFA ($J \cdot g^{-1} \cdot K^{-1}$)	σ	Cp DSC ($J \cdot g^{-1} \cdot K^{-1}$)	σ	Relative Error (%)
A	50	2.122	0.090	2.308	0.058	8.1
	85	2.168	0.101	2.485	0.063	12.8
	115	2.179	0.088	2.642	0.067	17.5
	130	2.219	0.094	2.721	0.069	18.5
B	50	1.554	0.011	1.349	0.048	15.3
	85	1.547	0.012	1.448	0.054	6.8
	115	1.550	0.006	1.538	0.058	0.8
	130	1.544	0.010	1.586	0.060	2.6
C	50	1.295	0.047	1.348	0.052	3.9
	85	1.297	0.047	1.453	0.057	10.7
	115	1.327	0.054	1.544	0.061	14.0
	130	1.331	0.060	1.591	0.062	16.4
D	50	1.685	0.082	1.622	0.102	3.9
	85	1.741	0.091	1.714	0.110	1.6
	115	1.807	0.096	1.795	0.117	0.7
	130	1.824	0.095	1.836	0.119	0.6

The results presented in Table 4 show that both methods provide similar values, with the relative error ranging from 0.6 % to 18.5 %. Material D is the most accurate, which could be related to it being the only composite with a single type of filler. In comparison to the other materials, this makes it the most homogeneous, which is a requirement for the LFA method.

The specific heat capacities obtained by LFA and DSC as a function of time and respective linear regressions equations and R-squared fit are shown in Figure 4-3.

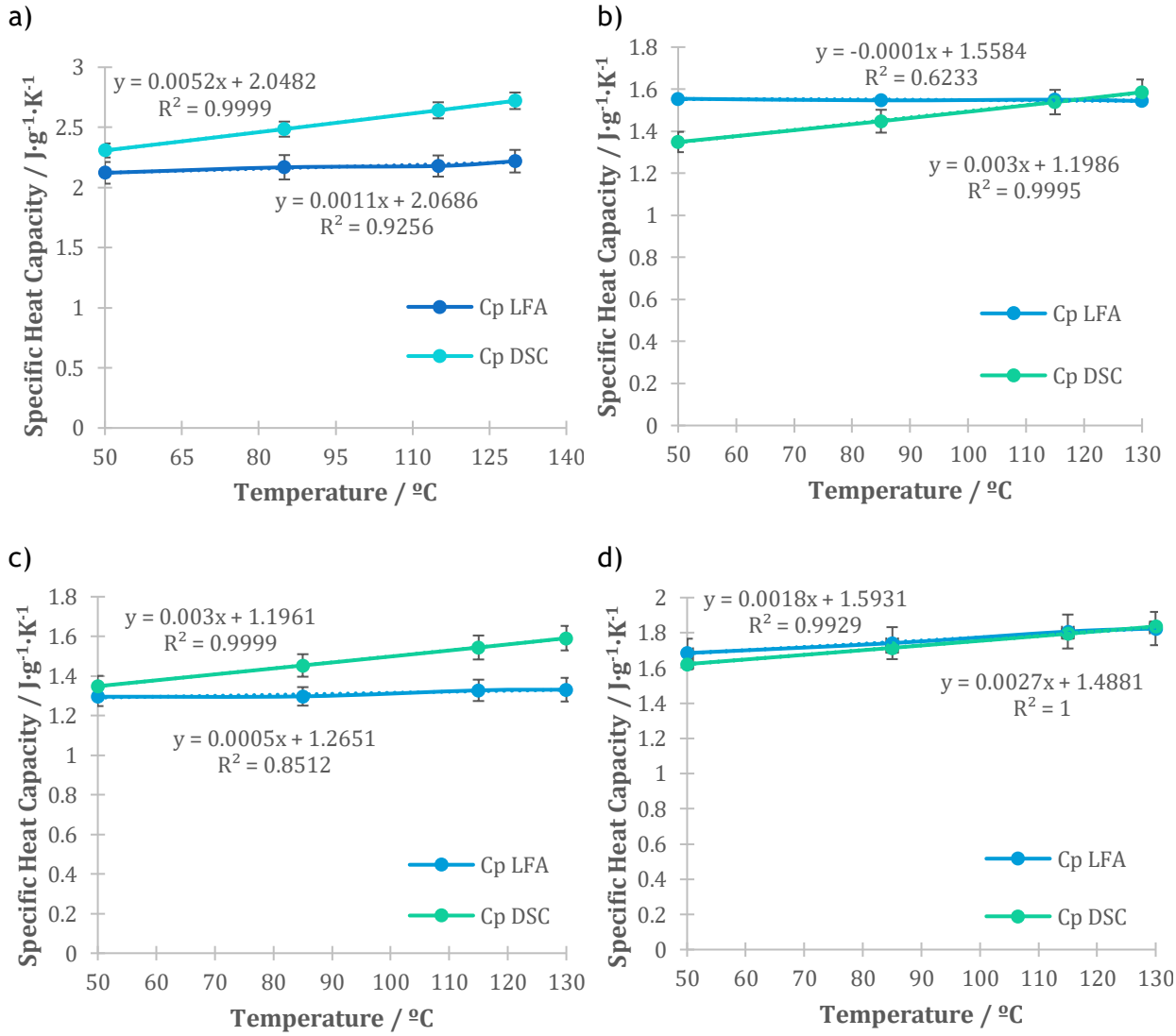


Figure 4-3 - Specific Heat obtained by DSC and LFA for samples (a) A, (b) B, (c) C and (d) D.

An increase in specific heat capacity with temperature was observed for all samples in Figure 4-3. In thermodynamics, the specific heat capacity is the amount of heat required to cause an increase of one unit in temperature for one unit of mass of the material. As temperature increases, the average kinetic energy of the molecules rises, and vibrational energy gains increasing significance. Thus, more heat is required to raise the temperature due to the additional energy required for vibrational energies.

DSC measurements could only be performed at the minimum temperature of 50 ºC due to apparatus limitations. Therefore, the values for 35 ºC were calculated using the linear regression equations derived from the experimental data since all equations have a good R^2-fit (>0.9995).

4.3 Thermal conductivity

Using the density, specific heat calculated using the DSC approach and the thermal diffusivity determined previously, the thermal conductivity was calculated. For heat sink applications, thermal conductivity values should be superior to 5 $W \cdot m^{-1} \cdot K^{-1}$ through-plane and 20 $W \cdot m^{-1} \cdot K^{-1}$ in-plane.

Thermal diffusivity decreases with temperature and specific heat capacity increases; it is important to evaluate which of these effects dominates. Temperature dependence of the calculated thermal conductivity for through-plane and in-plane measurements are shown in Figure 4-4 and Figure 4-5, respectively. These results refer to position 2, located at the centre of the discs.

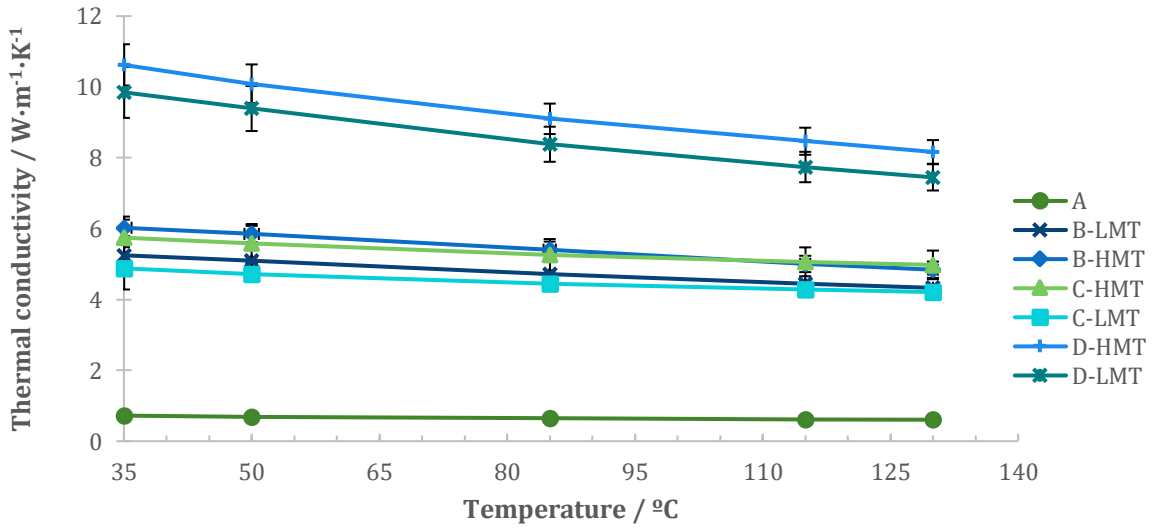


Figure 4-4 – Representation of the through-plane thermal conductivity for position 2.

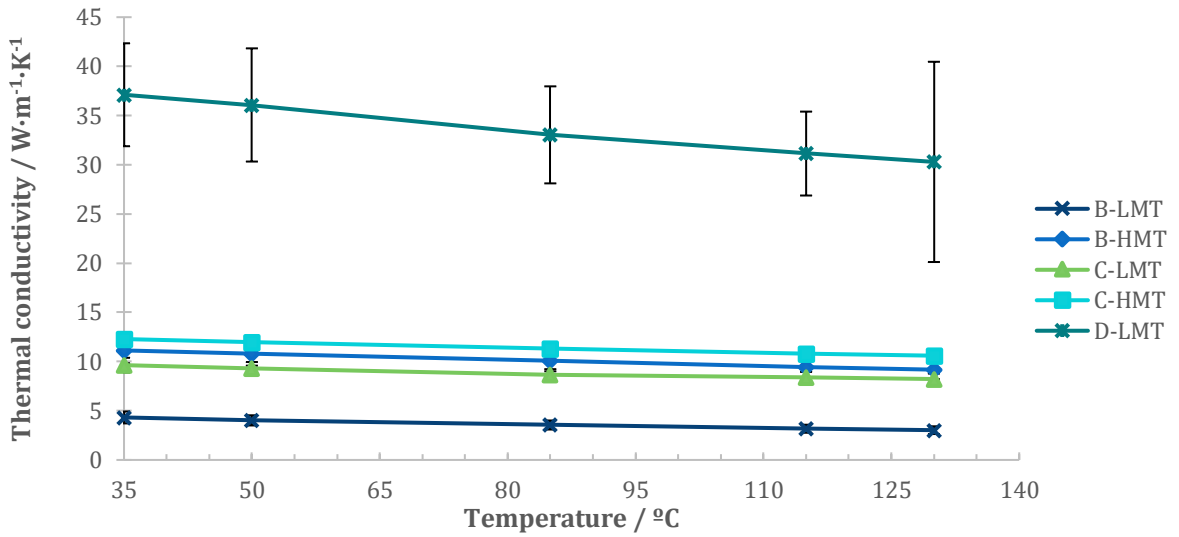


Figure 4-5 – Representation of the in-plane thermal conductivity for position 2.

The results presented in Figure 4-4 and Figure 4-5 lead to the inference that thermal conductivity decreases with increasing temperature. As temperature increases, the molecular vibrations also increase, decreasing the mean free path for heat conduction. This means obstruction of the flow of electrons and phonons, which results in a reduction in thermal conductivity.

The values of thermal conductivity obtained in-plane are substantially higher than through-plane, which can be attributed to the heat being conducted mainly through covalent bonding between carbon atoms, whereas the through-plane heat conduction is limited by weak van der Waals forces.

Since all samples follow the same trend regarding temperature, the study of the differences in thermal conductivity with different mould temperatures and between different regions of the original disc can be focused on one temperature. To facilitate this analysis, results are shown for 35 ºC. Results for thermal conductivity as a function of time for all samples are presented in Appendix D.

In-plane measurements

Figure 4-6 presents the results for measurements of thermal conductivity in-plane, at 35 ºC, for selected samples considering the previous results.

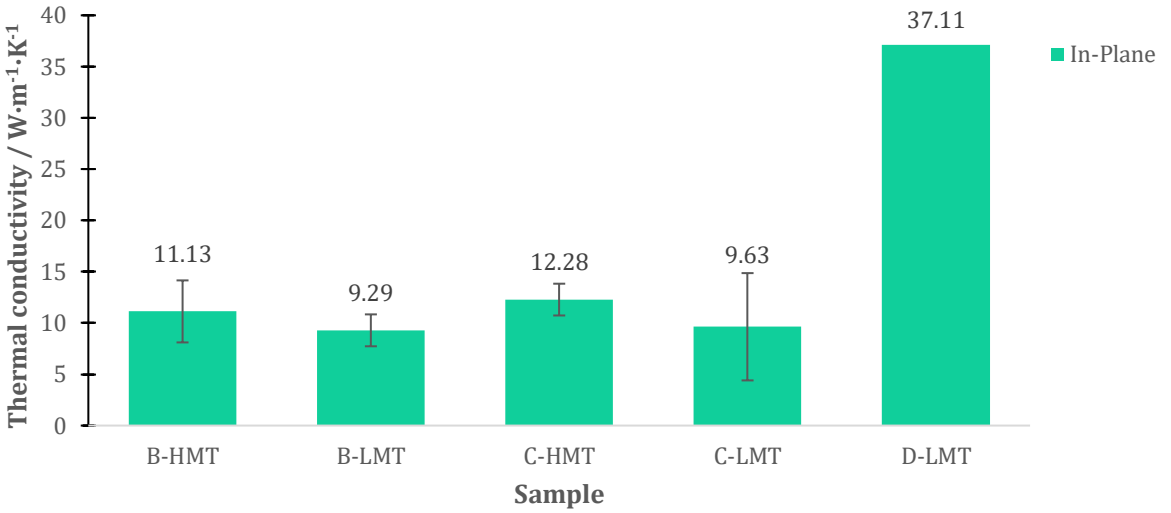


Figure 4-6 – Representation of the in-plane thermal conductivity at 35 ºC.

The analysis of Figure 4-6 concludes that the increase in mould temperature positively influences thermal conduction in the composites. All materials injected at higher mould temperatures show higher thermal conductivity. The higher mould temperature minimizes the difference in temperature between the melt and the mould walls, thus delaying the heat transfer. This materializes in a lower viscosity of the melt and slower crystallization, which means the fillers have more liberty to rotate and align with the flow direction.

Material D is the only one with thermal conductivity superior to 20 $W \cdot m^{-1} \cdot K^{-1}$, as required for heat exchanger applications.

Through-plane measurements

The measurements through-plane were performed for four different positions, which are indicated in blue to represent the discs manufactured by injection moulding in Figure 4-7.

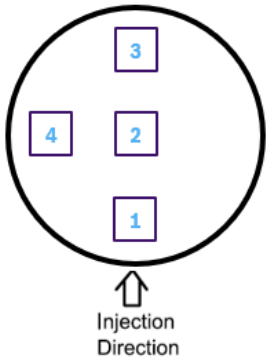


Figure 4-7 – Representation of the disc samples, with the different analysed positions in blue.

The results obtained through-plane are presented in Figure 4-8, for all four positions, at 35 ºC.

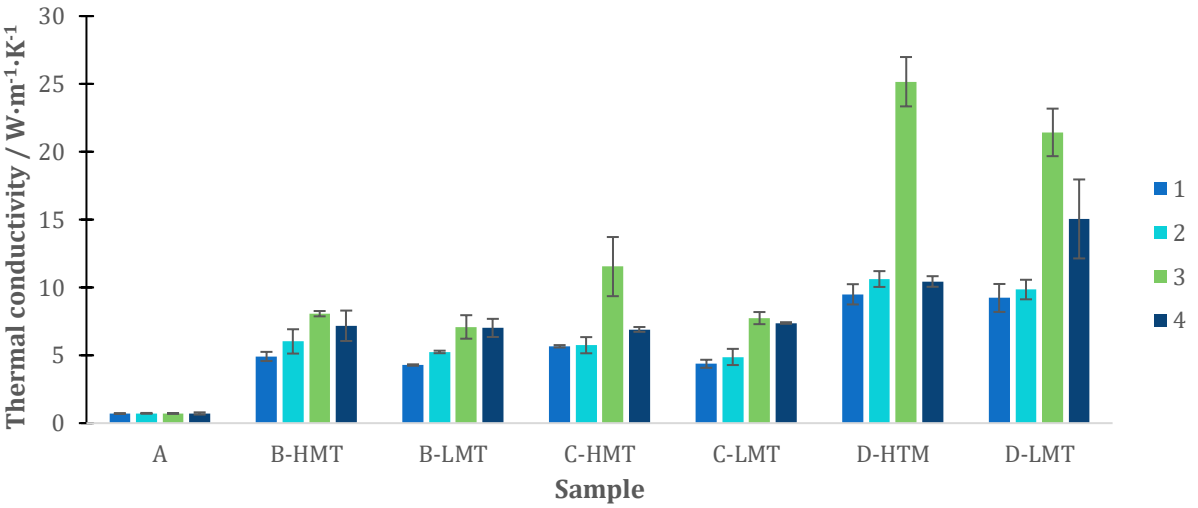


Figure 4-8 – Representation of the through-plane thermal conductivity at 35 ºC.

In Figure 4-8 it is possible to see that the thermal conductivity increases from position 1 to 3, where it reaches its highest values. During the injection mouldin g process, the fillers in the melt are oriented in different directions under the influence of shear forces resulting from flow patterns. This leads to different thermal conductivities at different parts of the disc. Figure 4-9 shows a moulded disc, where traces of the flow pattern are evident.



Figure 4-9 – Flow pattern in a disc produced from injection moulding.

The effect of mould temperature appears to be the same as in-plane. The samples with higher mould temperature (HTM) display higher values than those with lower mould temperature (LMT). The increase in mould temperature leads to higher filler orientation in the through-plane measurements, same as in the in-plane.

- **Sample A**

The through-plane thermal conductivity of material A in relation to temperature for each position at 35 ºC can be seen in Figure 4-10.

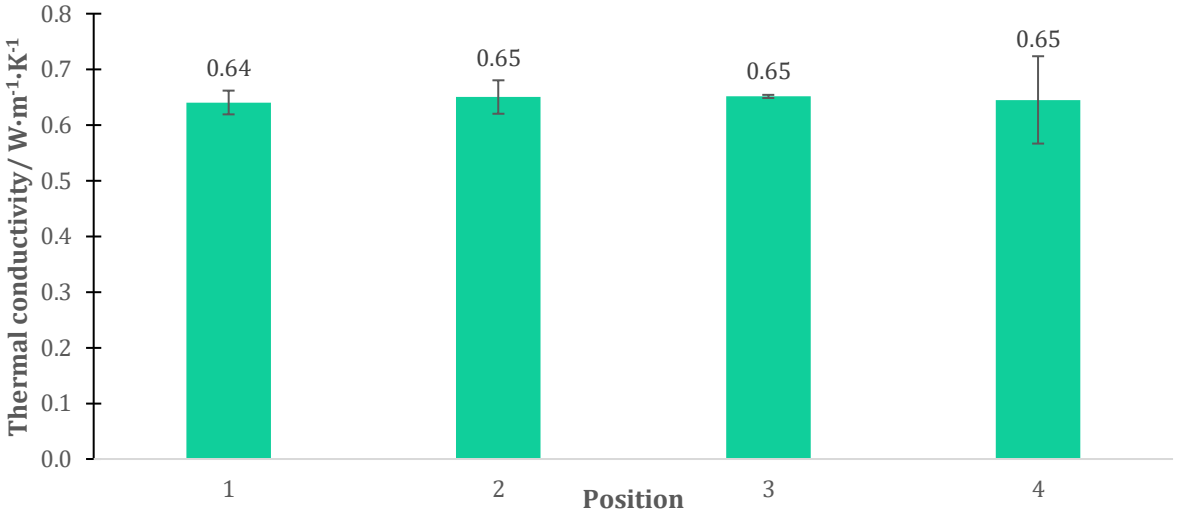


Figure 4-10 – Through-plane thermal conductivity of sample A at 35 ºC.

Material A does not show differences in thermal conductivity between different regions of analysis. The results are constant and too low for the application in heat sinks. This material incorporates only carbon-based fillers, namely carbon black and carbon fibre, into the polymeric matrix. These are commonly used fillers to introduce thermal conductivity. However, since the polymer matrix represents about 63 wt% of this material, the low values obtained for thermal conductivity could be explained by the amount of filler not being high enough to form continuous conductive pathways in the polymer matrix.

- **Sample B**

The though-plane thermal conductivity of each position of B-HTM and B-LMT are presented in Figure 4-11.

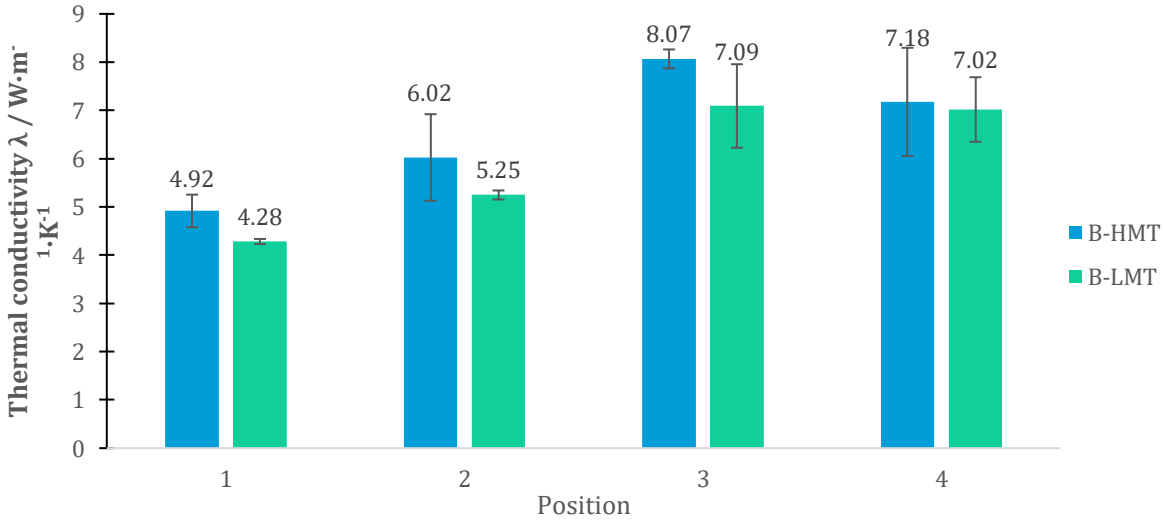


Figure 4-11 – Through-plane thermal conductivity of B-LMT and B-HMT at 35 ºC.

The analysis of Figure 4-11 indicates that the thermal conductivity measured through-plane differs with positions. In both cases, the values of B-LMT and B-HMT increase in the flow direction, from the first position, closest to the injection point, to the third, the furthest. On the sample with higher mould temperature, position 3 is the highest measured through-plane, while in the sample with lower mould temperature the positions 3 and 4 are similar.

Comparing positions in the same horizontal axis, position 4 is always higher than 2. This could root from the proximity to the mould walls and the frozen layer. Due to the high difference in temperature between the mould and the melt, a layer of the melt is immediately cooled without allowing the fillers to orient. Since this layer is not aligned, the melt close to it suffers greater resistance due to the shelled friction during the flowing process, causing considerable shear stress and inducing the orientation of the fillers in the flow direction. This effect has a higher impact when the difference in temperature melt and mould is higher, so in B-LMT. This could explain the proximity in the values for position 4. Position 3 could also benefit from this effect and be the front of the fountain flow and the most recent material to enter the mould. The measured thermal conductivity of material B meets the requirements for the desired application in heat sinks. All positions of both samples deliver values superior to 5 $W \cdot m^{-1} \cdot K^{-1}$, apart from B-LMT in position 1. When compared to sample A, these values increased significantly and are acceptable for heat exchangers applications. This material only contains about 24 %wt of the polymeric matrix, so the filler content should be high enough for the formation of heat conduction paths. The presence of graphite greatly induces the thermal conductivity.

- **Sample C**

The only differentiating factor between material B and C is the polymer matrix. Figure 4-12 presents the results of through-plane thermal conductivity for all positions of samples C-LMT and C-HMT at 35ºC.

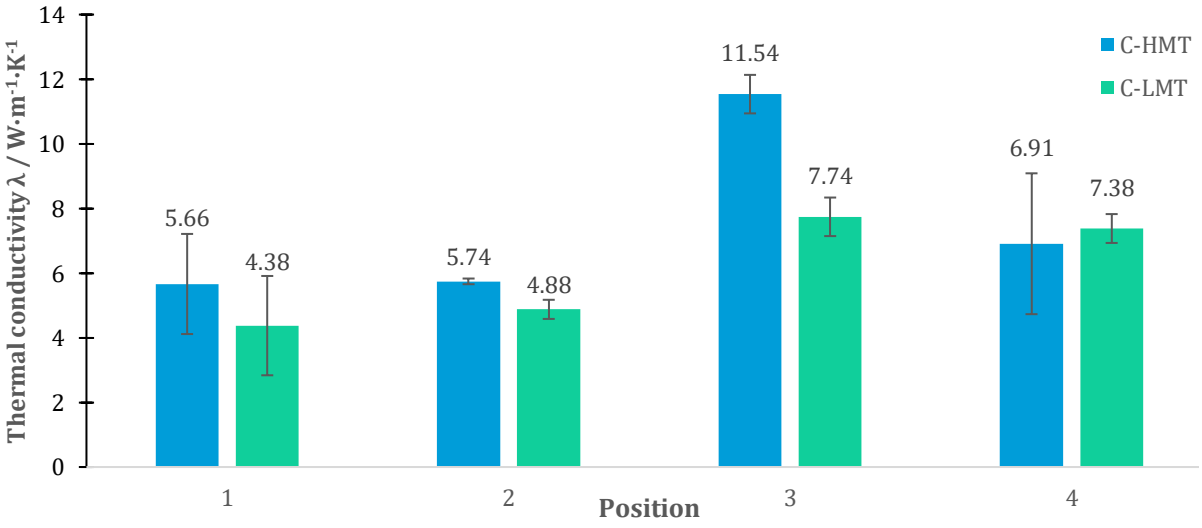


Figure 4-12 - Through-plane thermal conductivity of C-LMT and C-HMT at 35 ºC.

The thermal conductivity results for material C show similar tendencies to material B, with different values for different positions. Both C-HMT and C-LMT have the lowest thermal conductivity in position 1, followed by position 2. For the material with high mould temperature (C- HMT), position 3 is the highest measured through-plane. The material with low mould temperature (C-LMT) shows similar thermal conductivity values for positions 3 and 4. The same behaviour as in material B can be observed again for positions 2 and 4, with the proximity to the mould walls resulting in higher thermal conductivity for samples in the same horizontal axis. The thermal conductivity was superior in the sample with higher mould temperature for all positions, except position 4.

Material C also delivers thermal conductivity values superior to 5 $W \cdot m^{-1} \cdot K^{-1}$ on all positions, except for C-LMT in position 1. This material contains the same percentage of filler as B, which should be enough to allow for the formation of heat conduction paths.

- **Comparison of polymer matrix**

Material C has the same fillers, filler content and manufacturing parameters as material B, differing only in the matrix. Although PBT has lower thermal conductivity than PA6, the latter has significant advantages that make him a more exciting choice for the automotive industry. Comparing the two materials was performed to evaluate if the differences between them in thermal conductivity justify using one over the other when considering their other properties.

Thermal conductivity measured through-plane of samples B and C at high and at low mould temperature are presented in Figure 4-13 and Figure 4-14, respectively.

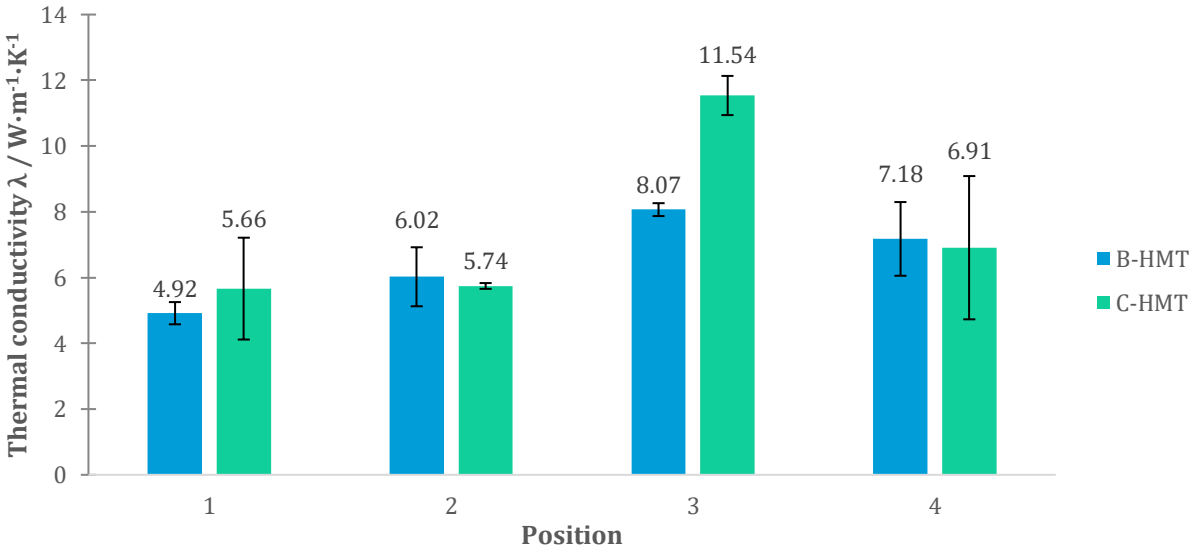


Figure 4-13 - Through-plane thermal conductivity of B-HMT and C-HMT at 35 ºC.

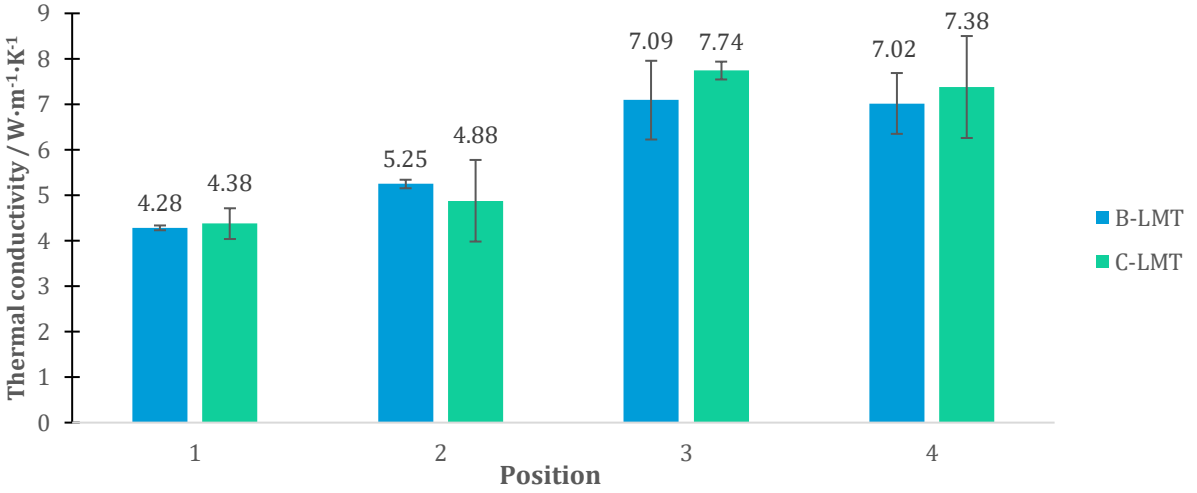


Figure 4-14 - Through-plane thermal conductivity of B-LMT and C-LMT at 35 ºC.

The results present similar thermal conductivity values for both materials, with the PBT matrix (C) even surpassing the values for position 3 with both high and low mould temperatures.

- **Sample D**

Figure 4-15 shows the results of through-plane thermal conductivity for all samples D-LMT and D-HMT positions at 35ºC.

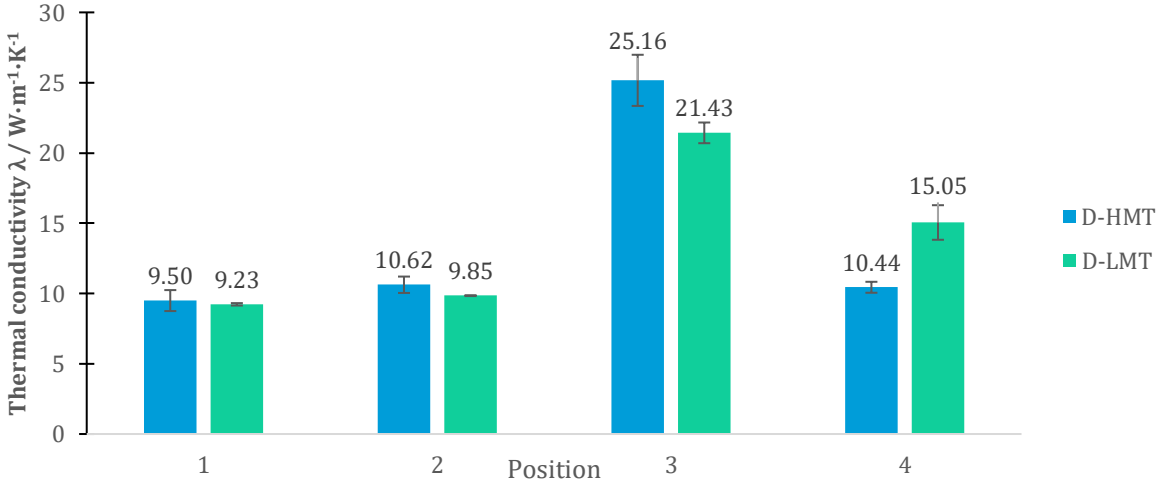


Figure 4-15 -Thermal Conductivity in each position of D-LMT and D-HMT at 35 ºC.

The results presented in Figure 4-15 indicate that the thermal conductivity of both D-LMT and D-HMT increase in the flow direction, with position 3 providing the highest values. Following the same trend as in materials B and C, the comparison of positions in the same horizontal axis shows that the thermal conductivity in position 4 is higher than in 2 for D-LMT. However, this

does not happen for the first time for the sample at high mould temperature (D-HTM). Instead, the difference between the two values is insignificant.

While materials B and C are hybrid composites with more than one type of filler, material D only contains graphite as a discontinuous phase. While hybrid composites can increase effective thermal conductivity, they can also create more resistances between the fillers. Thus, this single reinforcing phase material presents the most promising thermal conductivity values.

The difference in thermal conductivity between positions

Figure 4-16 shows a representation of the sample cut for transverse measurements, marking each position and the difference in mm between them. The difference between positions 1 and 2 and between 2 and 3 is only 20 mm in the vertical axis direction. Position 2 and 4 differ 20 mm in the horizontal axis direction, and positions 1 and 4 are 20 mm apart in the vertical direction and 20 mm in the horizontal direction.

Since all measurements were performed for samples cut from a disc with a diameter of only 60 mm, it is relevant to extrapolate the results from the laboratory to industrial scale. It is crucial to understand how the differences in thermal conductivity shown from different regions of the original disc could translate into heat sinks with much bigger dimensions. Table 5 shows the percentual increase in thermal conductivity between each position, as demonstrated in Figure 4-16.

Table 5. Increase in thermal conductivity between different positions of samples B-HMT and B-LMT at 35 ºC

Position	Thermal conductivity increase / %					
	B-HTM	B-LMT	C-HMT	C-LMT	D-HMT	D-LMT
1->2	22.5	22.5	1.4	11.5	-10.6	6.7
2->3	33.9	35.1	100.9	58.7	165.0	117.6
1->4	46.0	63.9	22.0	68.7	-1.7	63.1
2->4	19.1	33.8	20.3	51.3	10.0	52.9

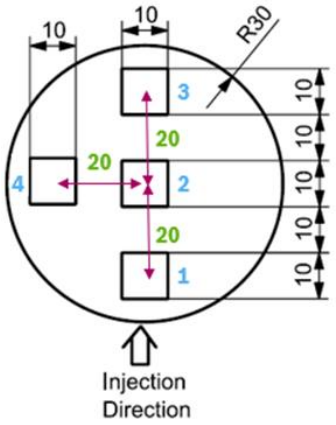


Figure 4-16 – Representation of the sample cut for through-plane measurements, with each position in blue and the difference between them in green.

These results show the relevancy of the differences between each position, especially from positions 2 to 3 where the thermal conductivity more than doubles for samples C-HMT (100.9 %) and D-HMT (165.0 %) in a difference of only 20 mm. When designing and manufacturing heat sinks, the injection point should be carefully chosen because it will determine how different regions of the product dissipate heat.

4.4 SEM/EDX

SEM analysis was performed to evaluate if the difference in thermal conductivity between measuring regions and with different mould temperatures resulted from different morphologies, such as filler load and dispersion. The test was performed for selected samples considering the results presented in Figure 4-17 shows the SEM images of B-LMT in positions a) 1, b) 2, and c) 3 and B-HMT in positions d) 1, e) 2, and f) 3. This material contains graphite, triiron tetraoxide and mineral powder on a PA6 matrix. The carbon materials cannot be evaluated in these images. The material manufactured with high mould temperature appears to have more extensive fillers. This could affect the lowering in melt viscosity resulting in lower shear between the filler and the polymer matrix, thus decreasing the filler degradation. SEM analysis does not conclude if the amount of conductive material increases from position 1 to 3.

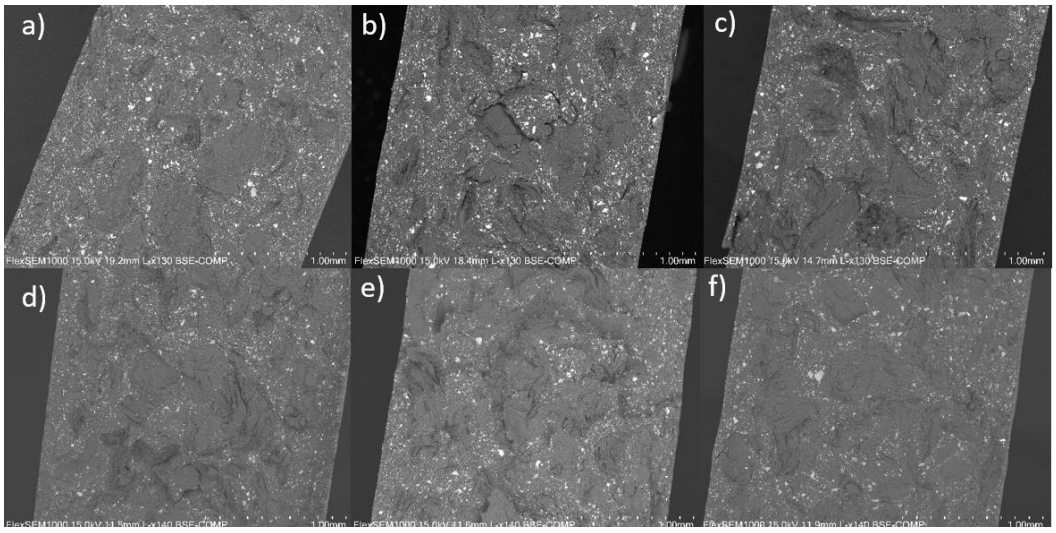


Figure 4-17 – SEM image of sample B-HMT for positions a) one, b) two and c) three and sample B-LMT for positions d) one, e) two and f) three. Image processing

EDX analysis showed that that materials B and C are composed of Carbon (C), Magnesium (Mg), Silicon (Si), Potassium (K), Iron (Fe), Aluminium (Al) and Oxygen (O). There is no significant variation in the amount of the chemical elements between positions, between different mould temperatures or between materials B and C. Since material D only contains the polymer matrix

and graphite, SEM and EDX analyses don't show any differences. The results of SEM and EDX obtained for other materials are presented in Appendix E and F, respectively.

4.5 Image processing

The software ImageJ was used to analyse the SEM images and estimate the filler content by utilizing their contrast, with the pixels with intensity values higher than the set threshold being identified as fillers. Selecting the correct threshold is vital for a more accurate analysis since it can greatly affect the results. This is a qualitative parameter, therefore choosing it manually leaves the results solely depending on the user's interpretation of the image, which may lead to unrealistic results. To reduce the user induced error, thresholds were defined with the models provided by the software. This allows for the for an estimation of the area fraction of the analysed images pertaining to fillers. Since material D only has graphite as fillers, the SEM images do not distinguish the filler from the matrix and thus weren't analysed. Table 6 shows the estimated percentages of the area of fillers in the SEM images for materials B and C. Figure 4-18 shows the analysis for sample B-LMT in position two, while the other results are presented in Appendix G.

Table 6. Estimation of percentage area of fillers in the SEM images of materials B and C, obtained by ImageJ.

Position	Filler Area / %			
	B-HMT	B-LMT	C-HMT	C-LMT
1	5.5	4.1	3.4	2.6
2	6.2	5.1	4.4	3.4
3	7.5	7.2	6.0	4.2

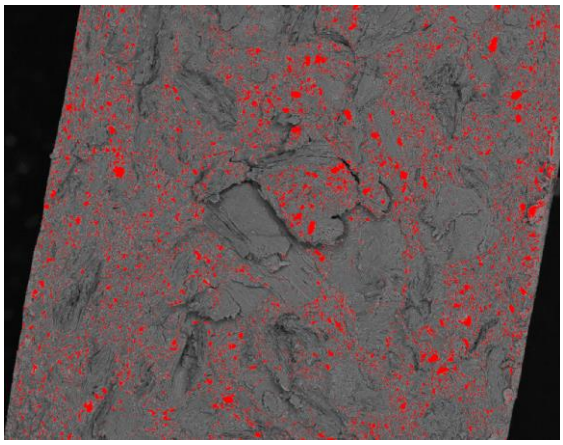


Figure 4-18 – ImageJ analysis for sample B-LMT in position 2.

The results presented in Table 6 indicate a slight increase in filler content from positions 1 to 3 on all four tests. Samples with high mould temperature (HMT) also show a slightly higher value than those with lower. Thus, these results corroborate the values obtained for thermal conductivity, although the percentual differences are minor. Additionally, the differences displayed for sample B for the different positions and the different mould temperatures are higher than those obtained for material C.

4.6 TGA

TGA was performed the evaluate the differences in filler content between measuring regions. A representative part of each position was heated to 800 ºC. This allows for the degradation of the polymer matrix so that the residual sample mass is assumed to be only fillers. The test was performed for samples B-HMT, C-HMT and D-HMT, as they show high percentual differences between each position, as previously shown in Figure 4-19 shows the mass loss as a function of time for B-HMT. In Figure 4-19 a) are apparent differences in mass loss between each measuring region. Position 3 lost the minor mass, translating to higher filler content, while position 1 lost the most, signifying the opposite. These results could explain the increase in thermal conductivity from position one to three in all the previous tests because higher filler content leads to higher thermal conductivity.

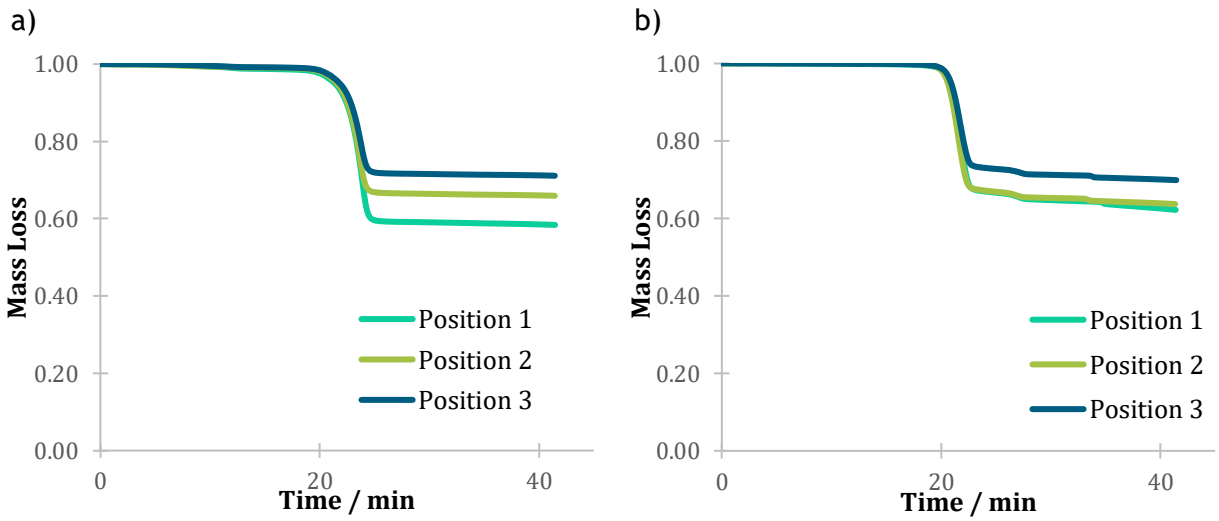


Figure 4-19 – TGA of the three positions of samples a) B-HMT and c) C-HMT.

Figure 4-19 b) shows that C-HMT also has different filler loading in the different regions analysed. Position 3 has the highest final mass, which means it has the most amount of filler. Position 1 lost the most weight and therefore has the least amount of filler. However, the difference is not as obvious as for B-HMT. These results agree with the thermal conductivity measurements since both increases in the flow direction (from position 1 to 3). The TGA analysis of sample D-HMT did not show any difference between each position, although the experimental results of thermal conductivity do. Table 7 presents the residual mass fraction for samples B-HMT, C-HMT and D-HMT obtained by TGA.

Table 7. Residual mass fraction for samples B-HMT, C-HMT and D-HTM, obtained by TGA.

Sample	B-HMT			C-HMT			D-HMT		
Position	1	2	3	1	2	3	1	2	3
Residual Mass Fraction / %	58.4	65.9	71.1	62.2	63.7	69.9	58.2	58.5	58.4

4.7 Micromechanical Models

To choose an adequate model for thermal conductivity prediction, the experimental values for position 2 (at the centre of the disc) at 35 ºC were compared to theoretical calculations. For the samples with different mould temperatures, the results for HTM were used.

Since material D only has one discontinuous phase, the models used to compare with the experimental value pertain to two-phase mixtures. Table 8 shows the results for sample D, using the plain and adequate mixtures models.

Table 8. Comparison of experimental and theoretical models for sample D for longitudinal effective thermal conductivity using models for two-phase mixtures.

	Inverse Rule of Mixtures	Geometric Mean	Maxwell	Bruggeman	Cheng and Vachon	Lewis and Nielsen φ_m = 0.637		Experimental
						A=3	A=1.5	
k ($w \cdot m^{-1} \cdot K^{-1}$)	2.88	9.80	5.48	7.45	14.58	12.76	10.09	10.62
Relative Error (%)	72.91	7.74	48.40	16.55	20.09	3.90	0.07	

The analysis of Table 8 concludes that the model that best estimates the experimental data is Lewis and Nielsen, for A = 1.5. The rule of mixtures has the biggest relative error associated. This model gives the lower limit for thermal conductivity estimation, which explains the prediction being significantly lower than the experimental error. Maxwell's model uses potential theory to predict the conductivity of randomly distributed and non-interacting homogeneous spheres[44]. This model underestimates high filler concentrations because it does not account for the formation of conductive networks in the flow direction due to the particle interaction. Bruggeman's model is derived from Maxwell's for spherical fillers and presents the same limitation. Cheng and Vachon assumed the discontinuous phases have a parabolic distribution and overestimate thermal conductivity[44]. Table 9 presents the comparison between thermal conductivity obtained experimentally and calculated through models for multi-phase mixtures for A, B and C since they contain multiple types of fillers.

Table 9. Comparison of experimental and theoretical models for samples A, B and C for longitudinal effective thermal conductivity using models for multi-phase mixtures.

		Inverse Rule of Mixtures	Geometric Mean	Hamilton		Cheng	Budiansky	Experimental
				Sphere n=3	Cylinder n=6			
A	***k*** **($w \cdot m^{-1} \cdot K^{-1}$)**	0.31	0.60	0.52	0.79	0.69	1.31	0.72
	Relative Error (%)	57.35	16.94	28.11	10.02	4.77	81.29	
B	***k*** **($w \cdot m^{-1} \cdot K^{-1}$)**	0.75	16.54	3.31	6.59	5.94	3.62	6.02
	Relative Error (%)	87.58	174.59	45.00	9.38	1.48	39.93	
C	***k*** **($w \cdot m^{-1} \cdot K^{-1}$)**	1.58	15.34	2.81	5.34	5.56	3.62	5.66
	Relative Error (%)	72.50	167.08	51.08	7.12	3.29	37.01	

For all samples, Cheng's model presented the best estimations pertaining to the experimental data. Since B and C only differ in the matrix, comparing the results obtained for both materials shows similar relative errors for each model. The geometric mean model presented the worst prediction in both cases since this model depends solely on the weighted average of fillers and matrix and has no physical basis. Budiansky's model assumes that the particles are near-spherical in shape, while Hamilton's model uses a parameter to account for non-spherical particles. Using Hamilton's model for samples A, B and C, the results are more favourable, assuming the particle are cylinders, explaining the high relative error calculated with Budiansky's. Considering these results, Cheng's and Lewis and Nielsen's models were used to predict thermal conductivity for two- and multi-phase mixtures, respectively, with increasing filler content. The amount of filler in the graphs indicates the total amount, and the contribution of each discontinuous phase was calculated according to the materials tested. The results are shown in Figure 4-20.

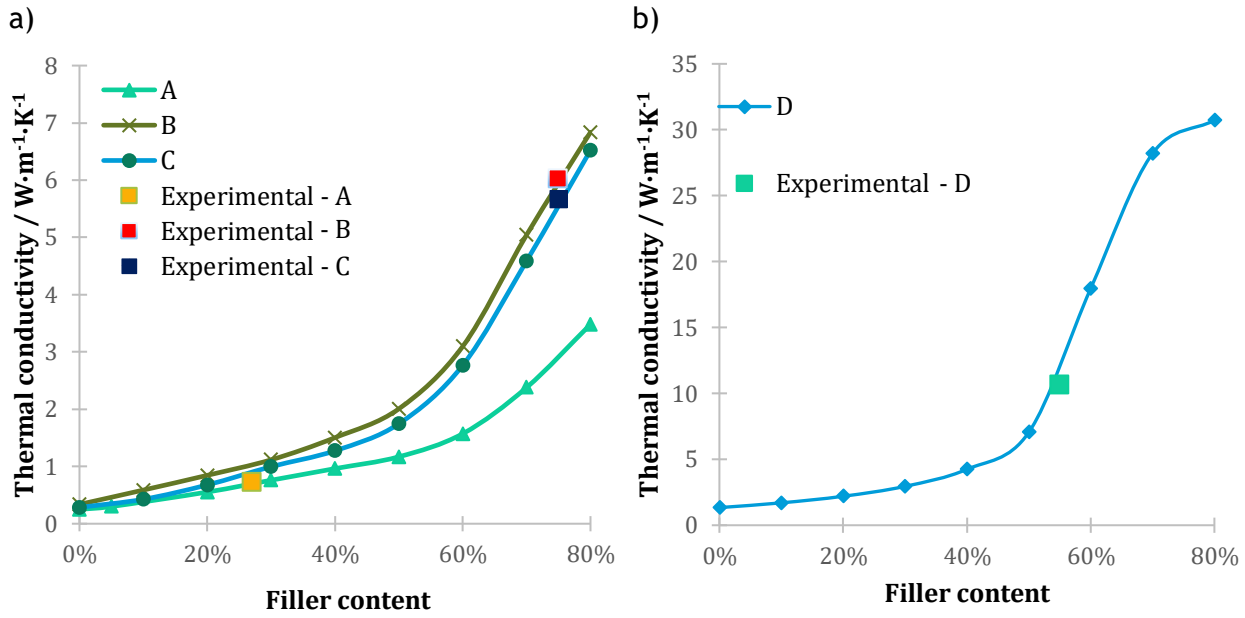


Figure 4-20 - Theoretical prediction of thermal conductivity with increasing filler load for samples A, B and C using the Cheng model and D using the Lewis and Nielsen model.

The results indicate that increasing the filler content leads to higher thermal conductivity. After reaching around 50 % quantity of filler, there is an exponential increase in thermal conductivity. These results are in agreement with the thermal percolation theory. The addition of conductive fillers above the percolation threshold results in the creation of a neighbouring micelles network. This allows for heat conduction and results in a sharp increase in thermal conductivity. Theoretically, increasing the filler content seems to be an effective method to increase thermal conductivity. However, the filler/matrix ratio cannot be infinitely increased. This would result in a deterioration of the mechanical properties of the material. Additionally, the material would be impossible to inject, and the density would increase.

5 Conclusions

This project assessed the thermal conductivity of different thermoplastic composites and different strategically selected regions of the samples produced by injection moulding, as well as the influence of the mould temperature in the injection moulding process on thermal conductivity.

While material A is an electrical material and does not deliver promising results, materials B, C and D show acceptable values with high enough thermal conductivity to substitute metals in heat sinks.

The results displayed a dependency of thermal conductivity on filler orientation. The samples measured perpendicularly to melt flowing (through-plane) displayed low thermal conductivity than those measured in parallel (in-plane).

This study showed that the thermal conductivity increases in the melt flow direction, from the injection point to the furthest point, with values increasing up to 165 % in regions only 20 mm apart. These results emphasize the importance of choosing the injection point in the manufacturing and design of polymer composite heat sinks since different regions present different thermal conductivity and cooling efficiency. SEM/EDX analysis does not show apparent differences to justify these results, but the image processing software detects slight differences in filler content between each region in agreement with the experimental data. Additionally, the TGA method indicated an increase in filler content in the melt flow direction, explaining the increase in thermal conductivity.

It was also shown that increasing the mould temperature positively affects thermal conductivity and is an effective way of optimizing the injection moulding process.

In conclusion, this work provides insight into the effects of mould temperature, melt flow direction and filler dispersion in the morphology and the thermal conductivity of thermoplastic composites. This allows for the optimization of the design and production of heat sinks for better performance and brings attention to the importance of choosing the injection point according to the requirements of the final product since it will influence thermal conductivity differently in different regions.

6 Assessment of the work done

6.1 Objectives achieved

The main goal of this dissertation was to select commercial injection grades and evaluate their morphology and thermal behaviour, as well as to understand if they meet the thermal requirements for heat exchanging applications, optimize injection parameters and investigate thermal behaviour in different regions of the samples. The appropriate test was performed, and the main objectives of this dissertation were fulfilled.

6.2 Limitations and Future Work

As a limitation, the current pandemic situation delayed the work, especially at the beginning. It took more than excepted for the samples to be produced by injection moulding and cut according to the requirements of the study.

As further work, the characterization of the thermoplastic composites using X-ray micro-computed tomography (μCT) could be beneficial to understand the differences in morphology between positions and samples with different mould temperatures. Additionally, since this work was oriented toward replacing metals with thermoplastic composites in heat sinks, it would be interesting to perform the same tests on that final product. All tests were performed for samples of a disc with only 60 mm and, since significant differences were obtained for parts separated by only 20 mm, it would be interesting to study how this behaviour translates to the final product.

6.3 Final Assessment

The appreciation of the work done is very positive. The main goal was achieved, and the results obtained are solid and significant.

The experimental work was an excellent introduction to new characterization techniques and to understand the increasing applicability of polymer composites, specifically in the automotive industry. With the constant need for better performances, research in this area is fundamental. The Laser Flash Analysis is a sophisticated technique with a slow learning curve; however, it is evident that it possesses enormous potential after mastering the fundamentals. In addition, working in a fast-paced environment focused on innovation and making technological advances for commercial products was a great learning experience.

7 References

(1) Cernuschi, F.; Bison, P. G.; Figari, A.; Marinetti, S.; Grinzato, E. Thermal Diffusivity Measurements by Photothermal and Thermographic Techniques. *Int. J. Thermophys.* **2004**, *25* (2), 439–457. https://doi.org/10.1023/B:IJOT.0000028480.27206.cb.

(2) Chawla, K. K. Introduction. In *Composite Materials*; Springer New York: New York, NY, 2012; pp 3–6. https://doi.org/10.1007/978-0-387-74365-3_1.

(3) Zainudin, E. S.; Sapuan, S.; Imihezri, S. S. S. A Review of the Effect of Moulding Parameters on the Performance of Polymeric Composite Injection Moulding. *Turkish J. Eng. Environ. Sci.* **2006**, *30*, 23–34. https://doi.org/10.3906/sag-1207-74.

(4) Radford, D. W. Application of High Temperature Polymer Matrix Composites to Engine Intake Valves. In *Comprehensive Composite Materials II*; Elsevier: Oxford, 2017; pp 312–349. https://doi.org/10.1016/B978-0-12-803581-8.10339-X.

(5) Loos, M. Composites. In *Carbon Nanotube Reinforced Composites*; William Andrew Publishing: Oxford, 2015; pp 37–72. https://doi.org/10.1016/B978-1-4557-3195-4.00002-3.

(6) Gupta, G.; Kumar, A.; Tyagi, R.; Kumar, S. Application and Future of Composite Materials: A Review. *Int. J. Innov. Res. Sci. Eng. Technol.* **2016**, *5* (5), 6907–6911.

(7) Marchetto, D.; Moreira, D.; Ribatski, G. A Review on Polymer Heat Sinks for Electronic Cooling Applications. In *Proceedings of the 17th Brazilian Congress of Thermal Sciences and Engineering*; Associacao Brasileira de Engenharia e Ciencias Mecanicas - ABCM: Águas de Lindóia, SP, Brazil, 2018; pp 25–28. https://doi.org/10.26678/ABCM.ENCIT2018.CIT18-0394.

(8) Pradeep, S.; Iyer, R.; Kazan, H.; Pilla, S. Automotive Applications of Plastics: Past, Present, and Future. In *Applied Plastics Engineering Handbook: Processing, Materials, and Applications: Second Edition*; Elsevier Inc., 2017; pp 651–673. https://doi.org/10.1016/B978-0-323-39040-8.00031-6.

(9) Biron, M. Thermoplastic Composites. In *Thermoplastics and Thermoplastic Composites*; Elsevier, 2007; pp 767–828. https://doi.org/10.1016/B978-185617478-7.50009-X.

(10) Gamstedt, E. K.; Berglund, L. A. Fatigue of Thermoplastic Composites. *Fatigue Compos. Sci. Technol. Fatigue Response Fibre-Reinforced Plast.* **2003**, 314–338. https://doi.org/10.1016/B978-1-85573-608-5.50016-4.

(11) Khemka, P. Plastics in the Automotive Industry – Which Materials Will Be the Winners and Losers? https://www.nexant.com/resources/plastics-automotive-industry-which-materials-will-be-winners-and-losers (accessed May 5, 2021).

(12) Khattak, Z.; Ali, H. M. Air Cooled Heat Sink Geometries Subjected to Forced Flow: A Critical Review. *Int. J. Heat Mass Transf.* **2019**, *130*, 141–161. https://doi.org/10.1016/j.ijheatmasstransfer.2018.08.048.

(13) Moore, A. L.; Shi, L. Emerging Challenges and Materials for Thermal Management of Electronics. *Mater. Today* **2014**, *17* (4), 163–174.

https://doi.org/10.1016/j.mattod.2014.04.003.

(14) Agari, Y.; Ueda, A.; Omura, Y.; Nagai, S. Thermal Diffusivity and Conductivity of PMMA/PC Blends. *Polymer (Guildf).* **1997**, *38* (4), 801–807. https://doi.org/10.1016/S0032-3861(96)00577-0.

(15) Asheghi, M.; Kurabayashi, K.; Kasnavi, R.; Goodson, K. Thermal Conduction in Doped Single-Crystal Silicon Films. *J. Appl. Phys.* **2002**, *91* (8), 5079–5088. https://doi.org/10.1063/1.1458057.

(16) Zhang, H.; Zhang, X.; Fang, Z.; Huang, Y.; Xu, H.; Liu, Y.; Wu, D.; Zhuang, J.; Sun, J. Recent Advances in Preparation, Mechanisms, and Applications of Thermally Conductive Polymer Composites: A Review. *J. Compos. Sci.* **2020**. https://doi.org/10.3390/jcs4040180.

(17) Si, W.; Sun, J.; He, X.; Huang, Y.; Zhuang, J.; Zhang, J.; Murugadoss, V.; Fan, J.; Guo, Z. Enhancing Thermal Conductivity via Conductive Network Conversion from High to Low Thermal Dissipation in the Polydimethylsiloxane Composites. *J. Mater. Chem. C* **2020**, *8* (10), 3463–3475. https://doi.org/10.1039/C9TC06968B.

(18) Guo, Y.; Ruan, K.; Shi, X.; Yang, X.; Gu, J. Factors Affecting Thermal Conductivities of the Polymers and Polymer Composites: A Review. *Compos. Sci. Technol.* **2020**, *193*, 108–134. https://doi.org/10.1016/j.compscitech.2020.108134.

(19) Patel, S. N.; Chabinyc, M. L. Anisotropies and the Thermoelectric Properties of Semiconducting Polymers. *J. Appl. Polym. Sci.* **2017**, *134* (44–403). https://doi.org/10.1002/app.44403.

(20) Eiermann, K.; Hellwege, K. -xH. Thermal Conductivity of High Polymers from −180°C. to 90°C. *J. Polym. Sci.* **1962**, *57* (165), 99–106. https://doi.org/https://doi.org/10.1002/pol.1962.1205716508.

(21) Burger, N.; Laachachi, A.; Ferriol, M.; Lutz, M.; Toniazzo, V.; Ruch, D. Review of Thermal Conductivity in Composites: Mechanisms, Parameters and Theory. *Prog. Polym. Sci.* **2016**, *61*, 1–28. https://doi.org/10.1016/j.progpolymsci.2016.05.001.

(22) Zhang, T.; Wu, X.; Luo, T. Polymer Nanofibers with Outstanding Thermal Conductivity and Thermal Stability: Fundamental Linkage between Molecular Characteristics and Macroscopic Thermal Properties. *J. Phys. Chem. C* **2014**, *118* (36), 21148–21159. https://doi.org/10.1021/jp5051639.

(23) Huang, C.; Qian, X.; Yang, R. Thermal Conductivity of Polymers and Polymer Nanocomposites. *Mater. Sci. Eng. R Reports* **2018**, *132*, 1–22. https://doi.org/https://doi.org/10.1016/j.mser.2018.06.002.

(24) Porto, L. S.; Silva, D. N.; de Oliveira, A. E. F.; Pereira, A. C.; Borges, K. B. Carbon Nanomaterials: Synthesis and Applications to Development of Electrochemical Sensors in Determination of Drugs and Compounds of Clinical Interest. *Rev. Anal. Chem.* **2019**, *38* (3). https://doi.org/doi:10.1515/revac-2019-0017.

(25) Wypych, G. Physical Properties of Fillers and Filled Materials. In *Handbook of Fillers*; Elsevier, 2016; pp 303–371. https://doi.org/B978-1-895198-91-1.50007-5.

(26) Tessema, A.; Zhao, D.; Moll, J.; Xu, S.; Yang, R.; Li, C.; Kumar, S. K.; Kidane, A. Effect of Filler Loading, Geometry, Dispersion and Temperature on Thermal Conductivity of Polymer Nanocomposites. *Polym. Test.* **2017**, *57*, 101–106.

https://doi.org/10.1016/j.polymertesting.2016.11.015.

(27) Zhang, S. The Effects of Particle Size and Content on the Thermal Conductivity and Mechanical Properties of Al2O3/High Density Polyethylene (HDPE) Composites. *Express Polym. Lett.* **2011**, *5* (7), 581–590. https://doi.org/10.3144/expresspolymlett.2011.57.

(28) Bicerano, J.; Douglas, J. F.; Brune, D. A. Model for the Viscosity of Particle Dispersions. *J. Macromol. Sci. - Rev. Macromol. Chem. Phys.* **1999**, *39* (4), 561–642. https://doi.org/10.1081/MC-100101428.

(29) Chen, H.; Ginzburg, V. V; Yang, J.; Yang, Y.; Liu, W.; Huang, Y.; Du, L.; Chen, B. Thermal Conductivity of Polymer-Based Composites: Fundamentals and Applications. *Prog. Polym. Sci.* **2016**, *59*, 41–85. https://doi.org/https://doi.org/10.1016/j.progpolymsci.2016.03.001.

(30) Tao, Y.; Yang, Z.; Lu, X.; Tao, G.; Xia, Y.; Wu, H. Influence of Filler Morphology on Percolation Threshold of Isotropical Conductive Adhesives (ICA). *Sci. China Technol. Sci.* **2012**, *55* (1), 28–33. https://doi.org/10.1007/s11431-011-4651-2.

(31) Zhang, Z. Thermal Properties of Solids and the Size Effect. In *Nano/Microscale Heat Transfer*; Springer, 2020; pp 175–253. https://doi.org/10.1007/978-3-030-45039-7.

(32) Samal, S. Effect of Shape and Size of Filler Particle on the Aggregation and Sedimentation Behavior of the Polymer Composite. *Powder Technol.* **2020**, *366*, 43–51. https://doi.org/10.1016/j.powtec.2020.02.054.

(33) Liu, C.; Chen, M.; Zhou, D.; Wu, D.; Yu, W. Effect of Filler Shape on the Thermal Conductivity of Thermal Functional Composites. *J. Nanomater.* **2017**, *2017*, 6375135. https://doi.org/10.1155/2017/6375135.

(34) Mohammad Nejad, S.; Bozorg Bigdeli, M.; Srivastava, R.; Fasano, M. Heat Transfer at the Interface of Graphene Nanoribbons with Different Relative Orientations and Gaps. *Energies* **2019**, *12*, 796. https://doi.org/10.3390/en12050796.

(35) Warzoha, R. J.; Fleischer, A. S. Heat Flow at Nanoparticle Interfaces. *Nano Energy* **2014**, *6*, 137–158. https://doi.org/10.1016/j.nanoen.2014.03.014.

(36) Babu, K. Thermal Contact Resistance: Experiments and Simulation, Chalmers University of Technology, Gothenburg, Sweden, 2015.

(37) Rosato, M.; Rosato, D. *Injection Molding Handbook*; Springer US, 2000. https://doi.org/10.1007/978-1-4615-4597-2.

(38) Baltussen, M. G. H. M.; Hulsen, M. A.; Peters, G. W. M. Numerical Simulation of the Fountain Flow Instability in Injection Molding. *J. Nonnewton. Fluid Mech.* **2010**, *165* (11), 631–640. https://doi.org/10.1016/j.jnnfm.2010.03.001.

(39) Li, X.-P.; Zhao, G.-Q.; Yang, C. Effect of Mold Temperature on Motion Behavior of Short Glass Fibers in Injection Molding Process. *Int. J. Adv. Manuf. Technol.* **2014**, *73* (5), 639–645. https://doi.org/10.1007/s00170-014-5874-8.

(40) Joseph Bensingh, R., Santhosh, M., & Ilangovan, S. Molding Process Induced Anisotropy Effect on Buckling Analysis of Fiber-Filled Plastic Crc Push Rod. *Int. J. Mech. Eng. Technol.* **2014**, *5* (2), 149–161.

(41) Bärwinkel, S.; Seidel, A.; Hobeika, S.; Hufen, R.; Mörl, M.; Altstädt, V. Morphology Formation in PC/ABS Blends during Thermal Processing and the Effect of the Viscosity

Ratio of Blend Partners. *Materials (Basel)*. **2016**, *9*, 659. https://doi.org/10.3390/ma9080659.

(42) Sepe, M. The Importance of Melt & Mold Temperature. **2011**, *57*, 16–17.

(43) NETZSCH. *LFA 467 HyperFlash® Series - Light Flash Apparatus*; 2017.

(44) Progelhof, R. C.; Throne, J. L.; Ruetsch, R. R. Methods for Predicting the Thermal Conductivity of Composite Systems: A Review. *Polym. Eng. Sci.* **1976**, *16* (9), 615–625. https://doi.org/https://doi.org/10.1002/pen.760160905.

(45) Cheng, S. C.; Law, Y. S.; Kwan, C. C. Y. Thermal Conductivity of Two-Phase and Three-Phase Heterogeneous Solid Mixtures. *Int. J. Heat Mass Transf.* **1972**, *15* (2), 355–358. https://doi.org/10.1016/0017-9310(72)90081-6.

(46) Shinzawa, H.; Mizukado, J. Water Absorption by Polyamide (PA) 6 Studied with Two-Trace Two-Dimensional (2T2D) near-Infrared (NIR) Correlation Spectroscopy. *J. Mol. Struct.* **2020**, *1217*, 128389. https://doi.org/10.1016/j.molstruc.2020.128389.

(47) Arhant, M.; Le Gac, P.-Y.; Le Gall, M.; Burtin, C.; Briançon, C.; Davies, P. Modelling the Non Fickian Water Absorption in Polyamide 6. *Polym. Degrad. Stab.* **2016**, *133*, 404–412. https://doi.org/10.1016/j.polymdegradstab.2016.09.001.

(48) Turner, S. R.; Liu, Y. Chemistry and Technology of Step-Growth Polyesters. In *Chemistry and Technology of Step-Growth Polyesters*; Elsevier: Amsterdam, 2012; pp 311–331. https://doi.org/10.1016/B978-0-444-53349-4.00143-6.

(49) ASTM International. *Standard Test Methods for Density and Specific Gravity (Relative Density) of Plastics by Displacement*; West Conshohocken, PA, 2020. https://doi.org/10.1520/D0792-20.

(50) KERN & Sohn GmbH. *Operating Instructions Density Determination Set: KERN PBS-A03/A04*; 2016.

(51) ASTM International. *Standard Test Method for Thermal Diffusivity by the Flash Method.*; ASTM E1461-07: West Conshohocken, PA, 2007. https://doi.org/10.1520/E1461-07.

(52) ASTM International. *Standard Test Method for Determining Specific Heat Capacity by Differential Scanning Calorimetry*; E1269-11: West Conshohocken, PA, 2018. https://doi.org/10.1520/E1269-11R18.

(53) ASTM International. *Standard Test Method for Compositional Analysis by Thermogravimetry*; E1131-20: West Conshohocken, PA, 2020.

(54) Bird , R. B.; Stewart, W. E.; Lightfoot, E. N. Thermal Conductivity and the Mechanisms of Energy Transportna. In *Transport Phenomena, Revised 2nd Edition*; Wiley, 2006; pp 263–190.

(55) Callister, W. D. *Materials Science and Engineering*, Seventh Ed.; John Wiley and Sons Inc.: New York, 2007.

(56) Lewis, T. B.; Nielsen, L. E. Dynamic Mechanical Properties of Particulate-Filled Composites. *J. Appl. Polym. Sci.* **1970**, *14* (6), 1449–1471. https://doi.org/https://doi.org/10.1002/app.1970.070140604.

Appendix A - Properties of different polymers

Table 10. Properties of some polymers[55].

Material	Category	Density ($g \cdot cm^{-3}$)	Maximum Service Temperature (ºC)	Tg (ºC)	Tm (ºC)	Volume Resistivity ($x10^{12}\ \Omega.m$)	HDT @1.8MPa (ºC)	Elastic Modulus (GPa)	k ($W \cdot m^{-1} \cdot K^{-1}$)
ABS	amorphous	1.05	86-89	90	221	14	100	1.79	0.14
HDPE	Semi-crystalline	0.97	100-120	-110	130.8	16	90	0.5	0.44
LDPE	Semi-crystalline	0.94	80-100	-110	105	0.92	59	0.13	0.33
PA 12	Semi-crystalline	1.01	70	35	176	10	50	1.7	0.12
PA 6	Semi-crystalline	1.14	80-120	60	219	14	80	2	0.24
PA 6.6	Semi-crystalline	1.15	80-140	55	280	14	105	2	0.25
PBT	Semi-crystalline	1.31	80-140	55	223	14	85	2	0.21
PC	Semi-crystalline	1.22	100-140	160	280	16	180	2.5	0.21
PEEK	Semi-crystalline	1.32	154-260	145	343	16	160	3.5	0.29
PEI	Amorphous	1.27	170	215	75	5	200	3	0.22
PES	Amorphous	1.37	175-180	220	227	15	203	2.3	0.17
PP	Semi-crystalline	0.92	100-130	-20	176	16	60	1	0.2
PPA	Semi-crystalline	1.2	140	125	330	15	110	3.7	0.15
PPS	Semi-crystalline	1.35	200-220	90	307	15	135	3.3	0.3
PS	amorphous	0.96	150-180	100	240	16	100	2.5	0.03

Appendix B - Thermal conductivity of commonly used thermally conductive fillers

Table 11. Thermal conductivity values of commonly used thermally conductive fillers[55].

Metals		**Ceramics**		**Carbon-based**	
Material	***k*** ($W \cdot m^{-1} \cdot K^{-1}$)	**Material**	***k*** ($W \cdot m^{-1} \cdot K^{-1}$)	**Material**	***k*** ($W \cdot m^{-1} \cdot K^{-1}$)
Aluminum	234	**Silica**	1.5	**Carbon nanotube**	1000–4000
Copper	400	**Aluminum Nitride**	80-200	**Carbon fibre**	300–1000
Gold	317	**ß -Silicon carbide**	120	**Carbon black**	6–174
Zinc	121	**ß-Silicon nitride**	103–200	**Graphene**	2000–6000
Iron	80	**Hexagonal Boron Nitride**	300+	**Graphite**	100–400
Nickel	90	**α-Alumina**	30		
Tin	67	**Beryllium oxide**	270		
Stainless Steel	15	**Magnesium oxide**	40		
Silver	427	**Zinc oxide**	30		

Appendix C - Technical specifications of the LFA equipment

Table 12. Technical specifications of the LFA equipment[43].

Temperature range	-100°C - 500°C
Maximum Heating rate	50 K/min
Furnace cooling device	Liquid nitrogen cooling (-100 °C– 500 °C) Pressurized air (0 °C – 500 °C)
Thermal diffusivity	0.01 $mm^2 \cdot s^{-1}$ - 2000 $mm^2 \cdot s^{-1}$
Thermal conductivity	0.1 $W \cdot m^{-1} \cdot K^{-1}$ - 4000 $W \cdot m^{-1} \cdot K^{-1}$
Accuracy	Thermal diffusivity: ± 3% Specific heat: ± 5%
Repeatability	Thermal diffusivity: ± 2% Specific heat capacity: ± 3%
Xenon flash lamp	Pulse energy: up to 10 Joules/pulse (variable), software-controlled Pulse width: 10 to 1500 µs
Atmosphere	Inert, oxidizing, static and dynamic
Vacuum	< 150 mbar
Data acquisition	2 MHz Minimum measurement time (10 half times) down to 1 ms for highly conducting and/or thin samples Maximum measurement time up to 120 s for low-conducting and/or thick samples



Figure C-1 – LFA 467 HyperFlash® manufactured by NETZSCH.

Appendix D - Experimental results of thermal conductivity

Below are presented the results of thermal conductivity as a function of time, from 35 ºC to 130 ºC, and the increase between positions.

D.1 Sample A

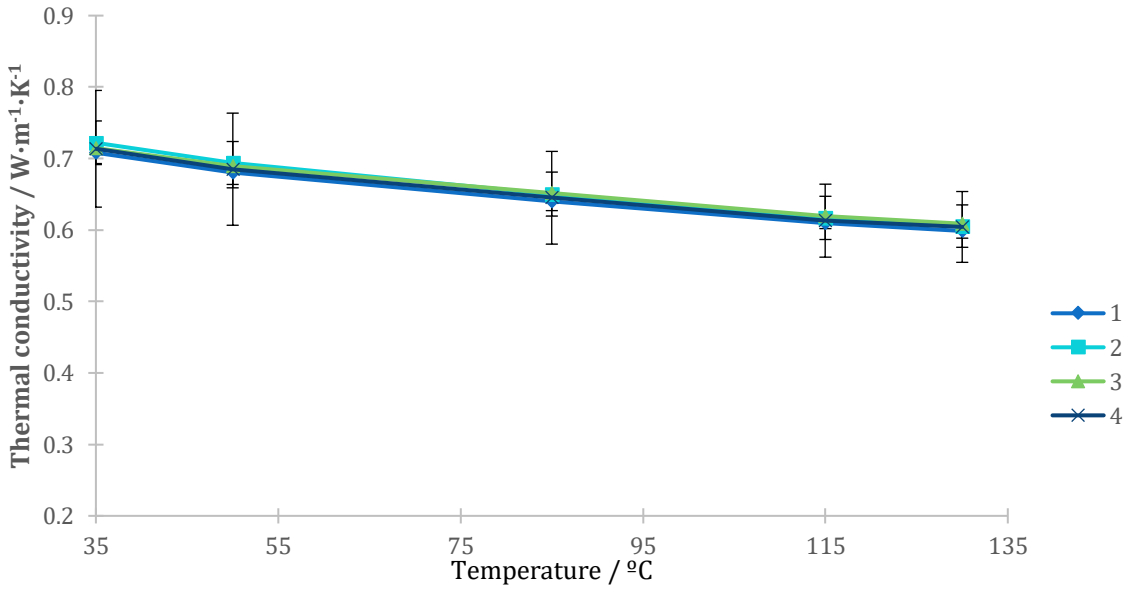


Figure D-1 – Through-plane Thermal conductivity as a function of temperature of sample A.

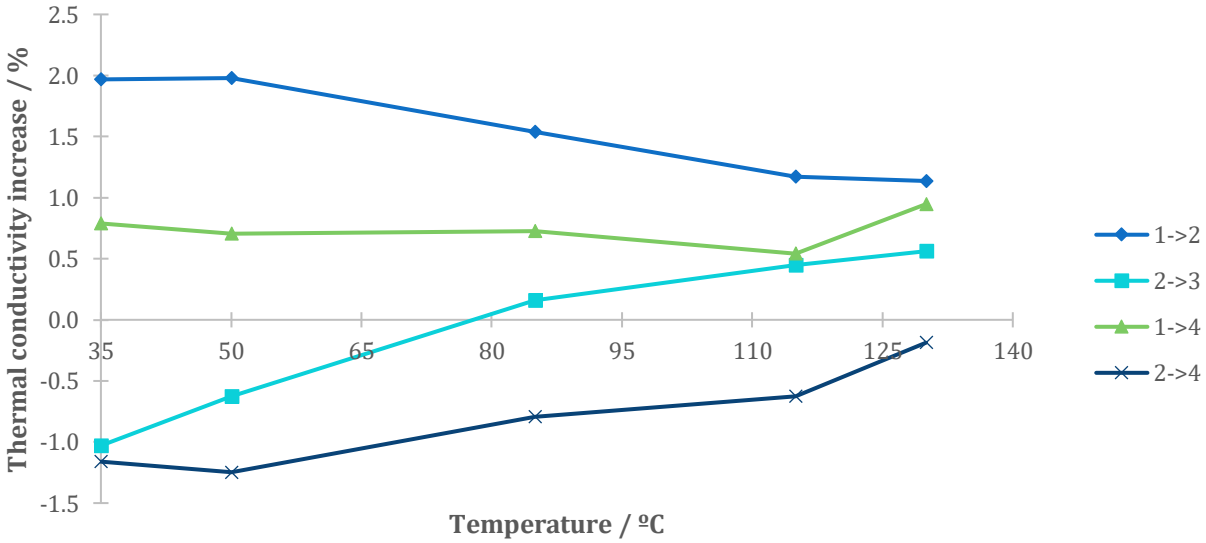


Figure D-2 – Percentual increase in thermal conductivity as a function of temperature between positions in sample A.

D.2 Samples B-HMT and B-LMT

Sample B-HMT

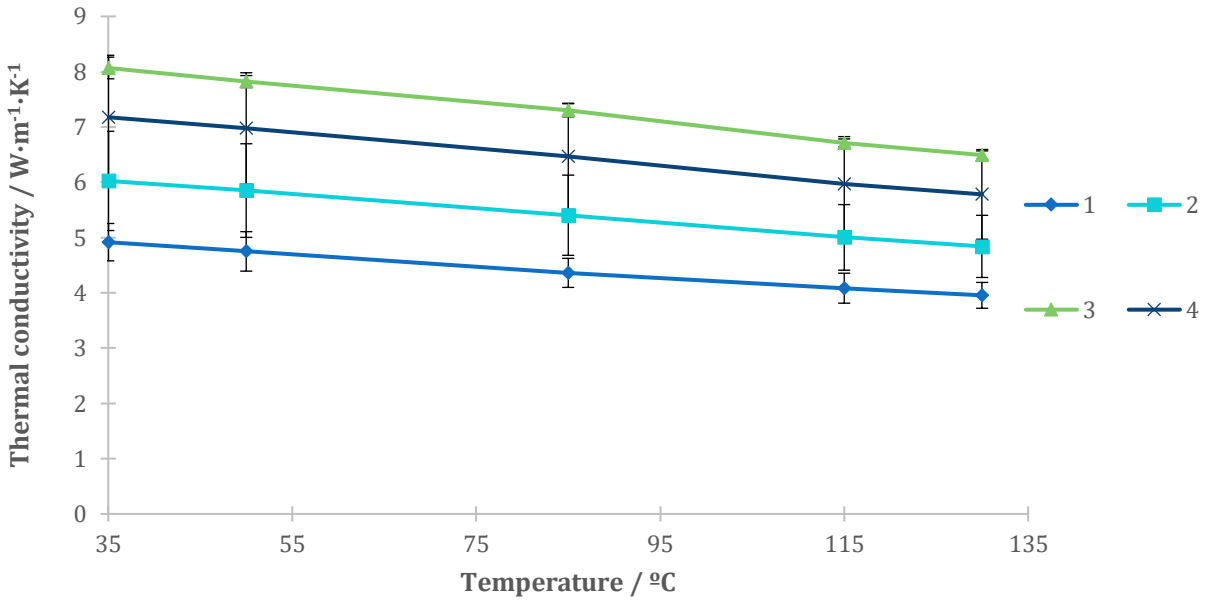


Figure D-3 – Through-plane Thermal conductivity as a function of temperature of sample B-HMT.

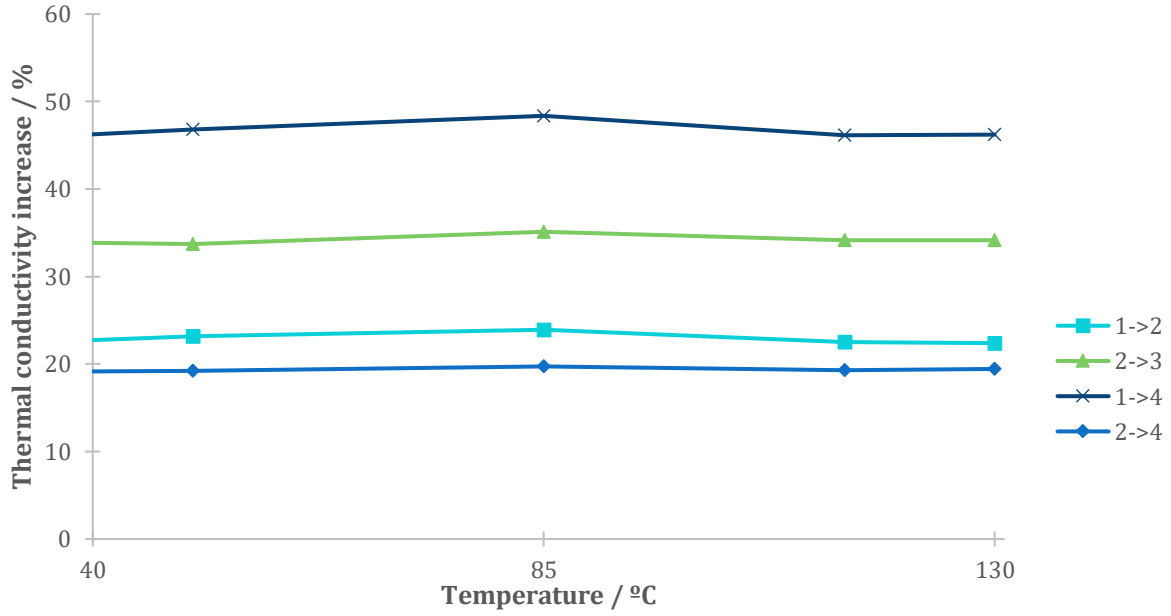


Figure D-4 – Percentual increase in thermal conductivity as a function of temperature between positions in sample B-HMT.

Sample B-LMT

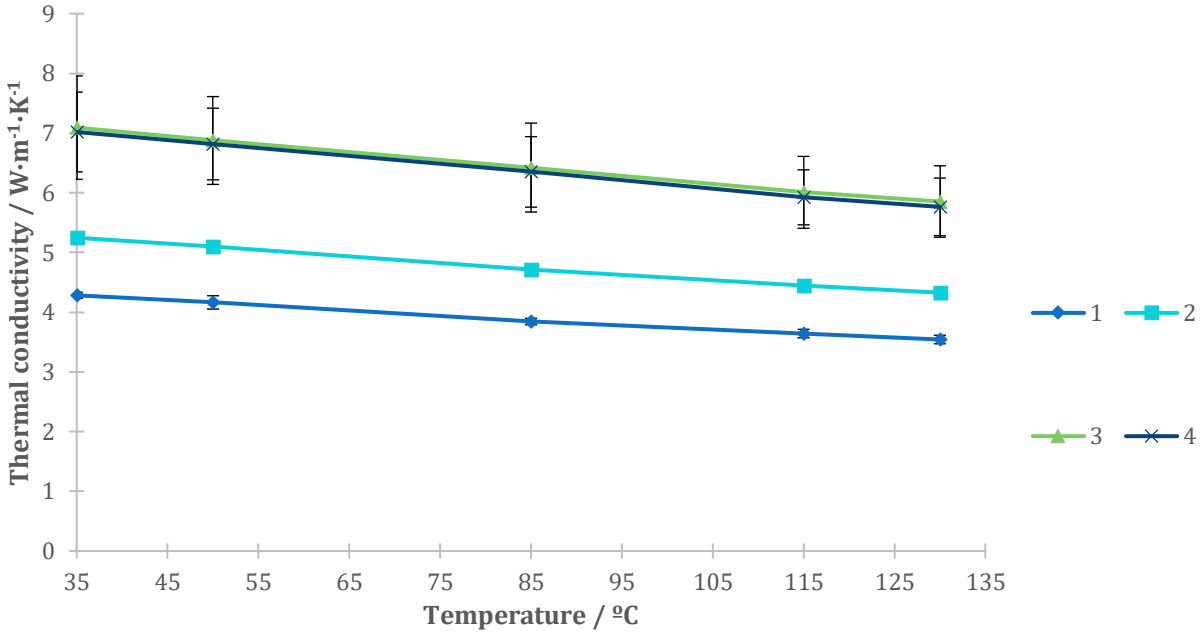


Figure D-5 - Through-plane thermal conductivity as a function of temperature of sample B-LMT.

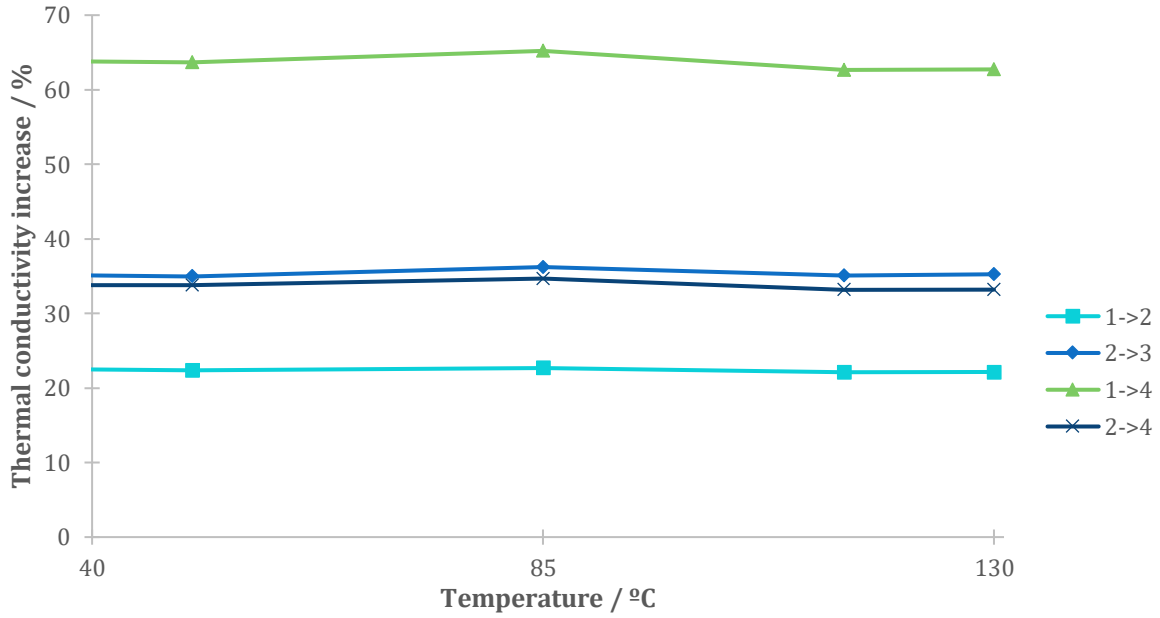


Figure D-6 - Percentual increase in thermal conductivity as a function of temperature between positions in sample B-LMT.

Comparison of through-plane thermal conductivity between sample B-HMT and B-LMT in each position

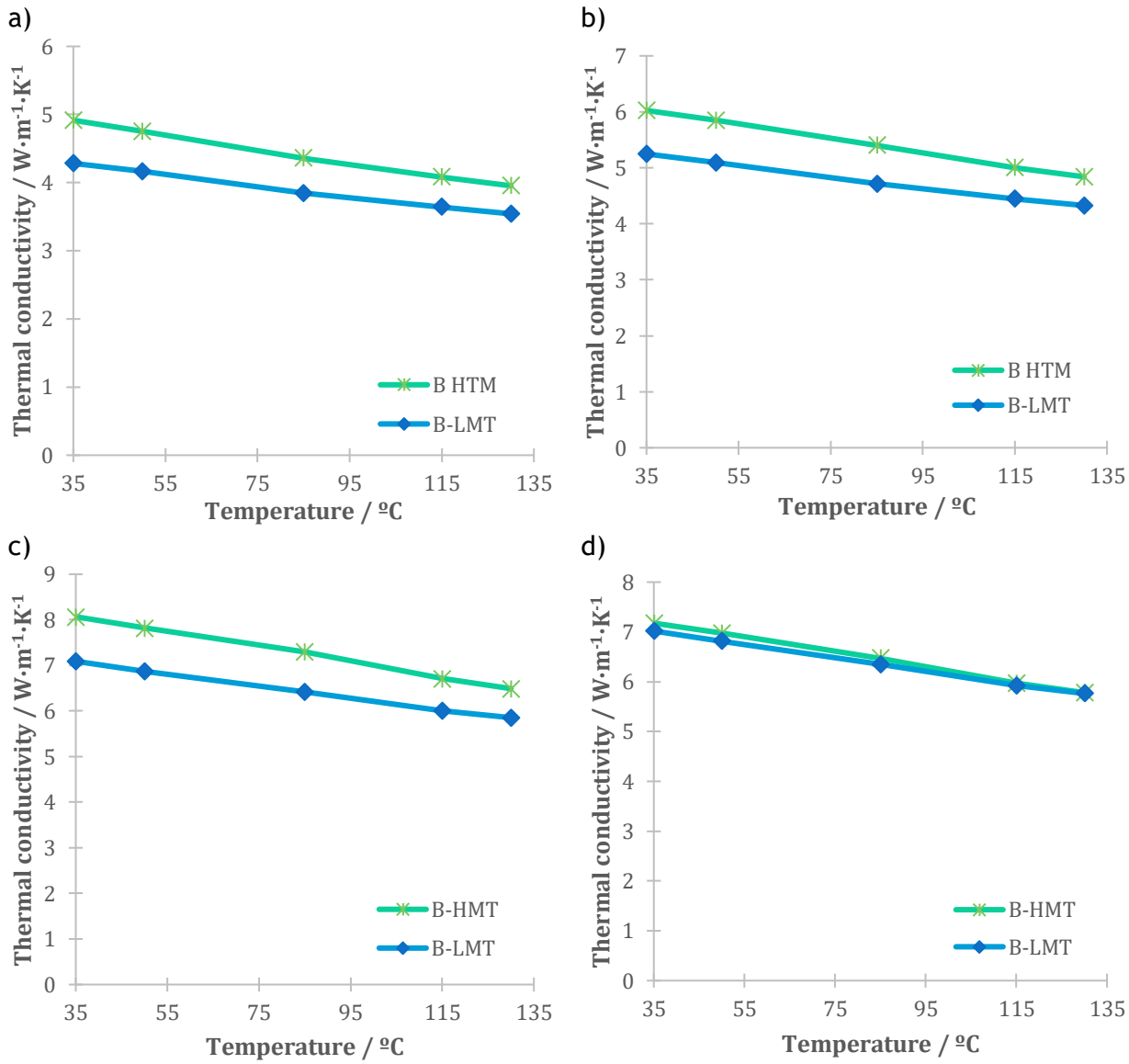


Figure D-7 – Through-plane thermal conductivity as a function of temperature of B-HMT and B-LMT in positions a) one, b) two, c) three and d) four.

Comparison of increase in through-plane thermal conductivity between sample B-HMT and B-LMT between positions

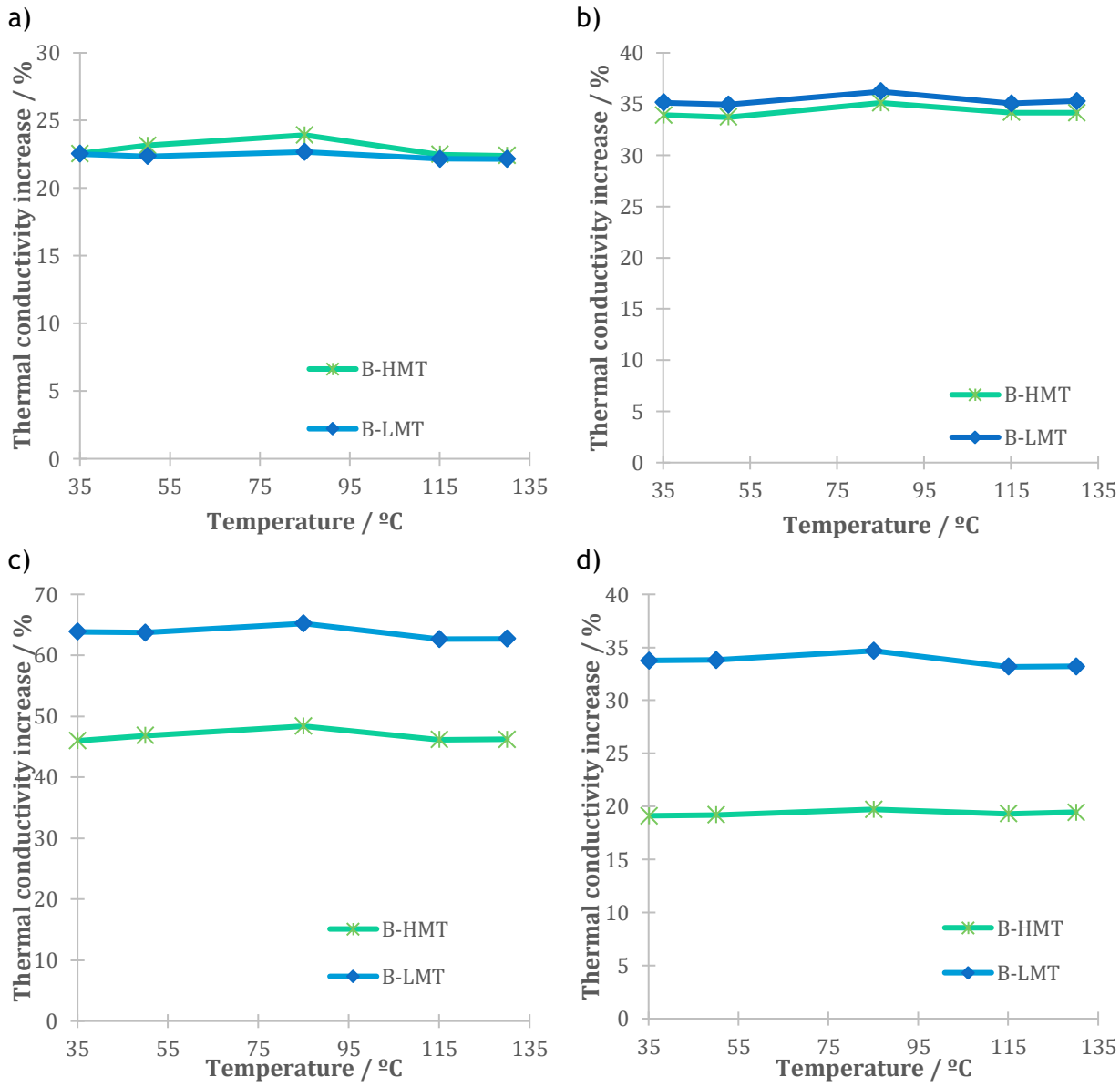


Figure D-8 - Increase in through-plane thermal conductivity for sample B-HMT and B-LMT between positions a) one and two, b) two and three, c) one and four and d) two and four.

D.3 Samples C-HMT and C-LMT

Sample C-HMT

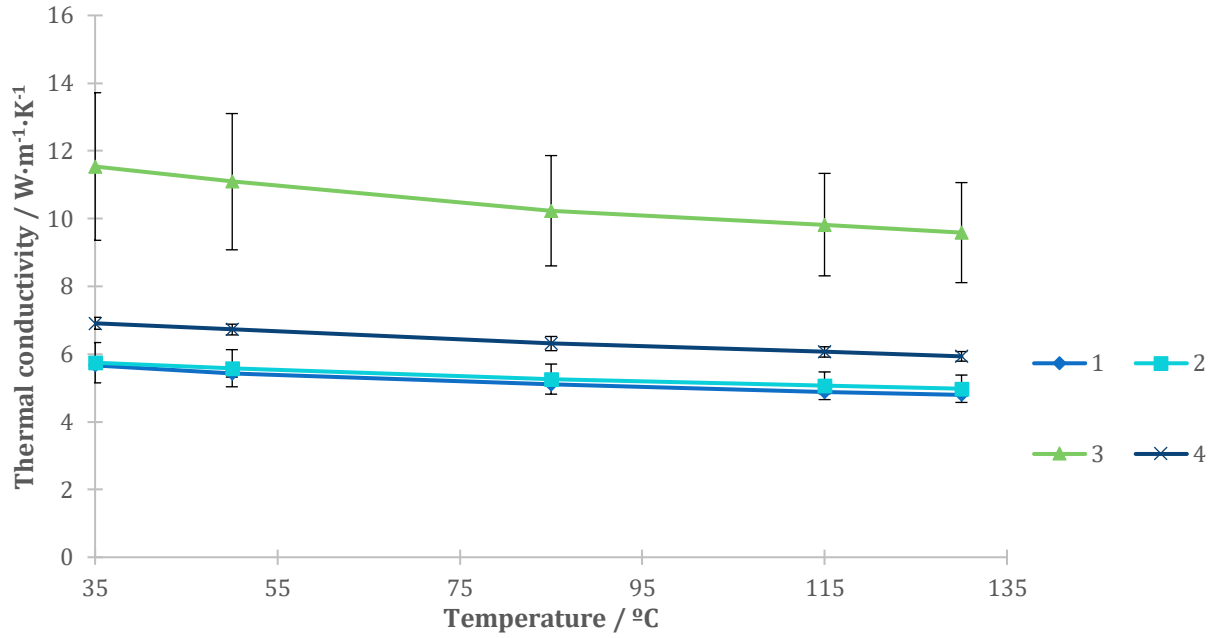


Figure D-9 – Through-plane Thermal conductivity as a function of temperature of sample C-HMT.

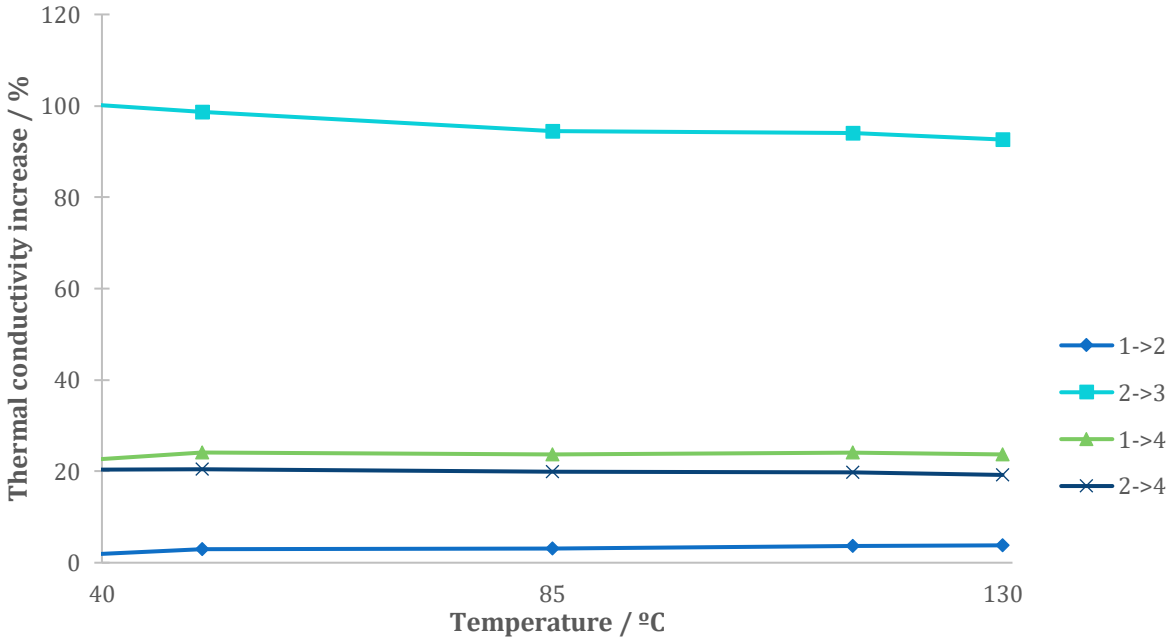


Figure D-10 - Percentual increase in thermal conductivity as a function of temperature between positions in sample C-HMT.

Sample C-LMT

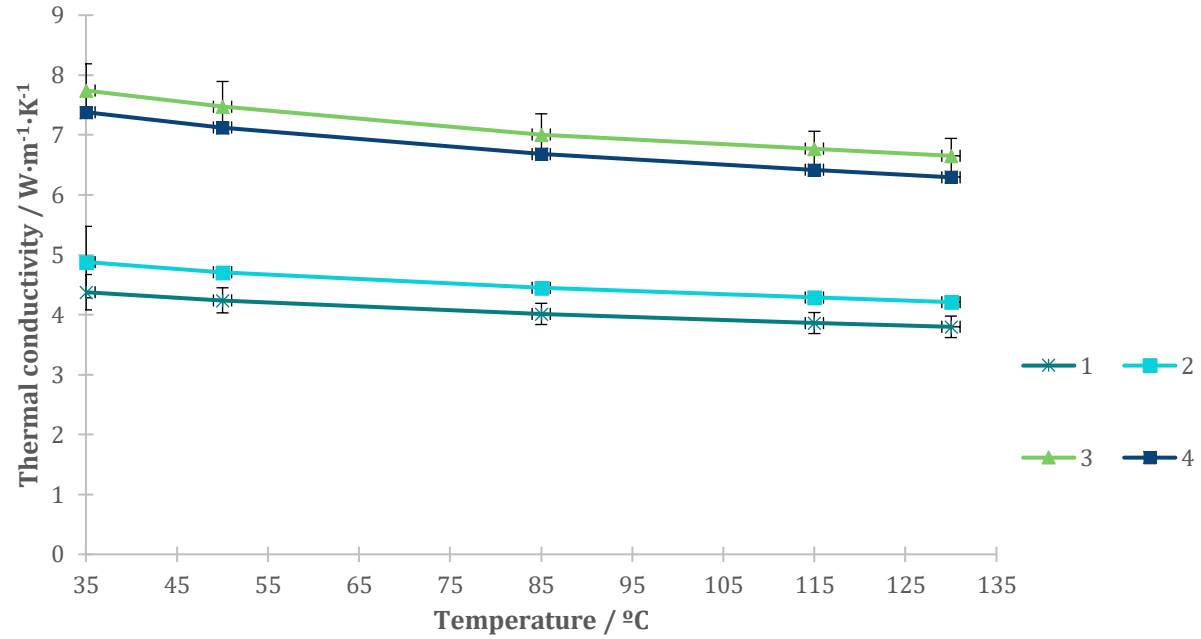


Figure D-11 – Through-plane Thermal conductivity as a function of temperature of sample C-LMT.

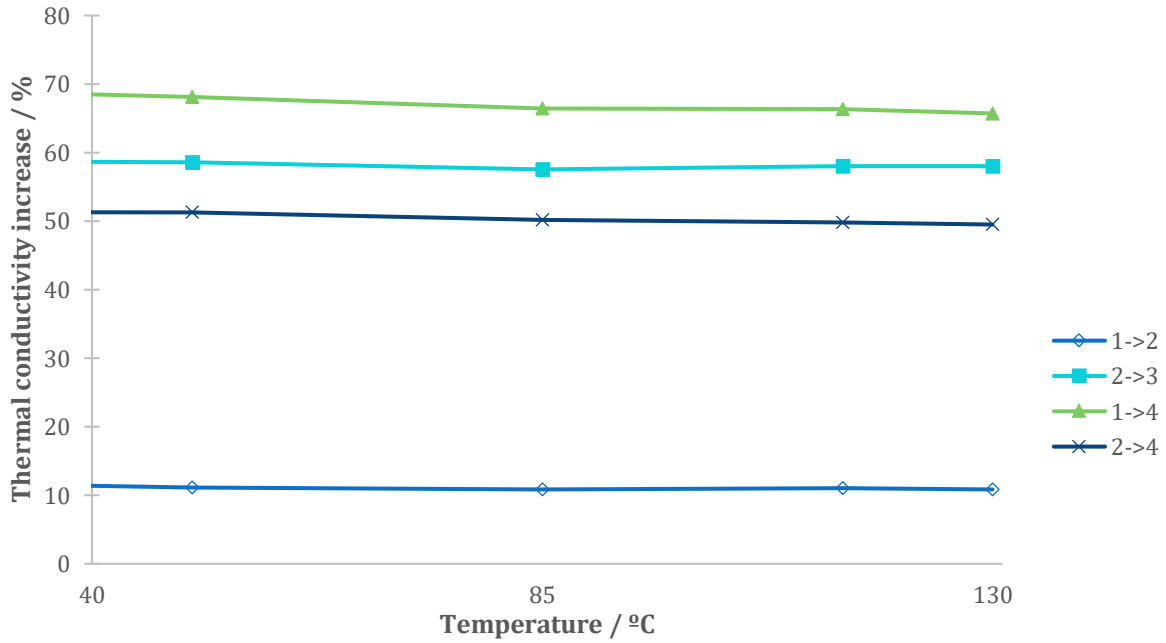


Figure D-12 – Percentual increase in thermal conductivity as a function of temperature between positions in sample C-LMT.

Comparison of through-plane thermal conductivity between sample C-HMT and C-LMT in each position

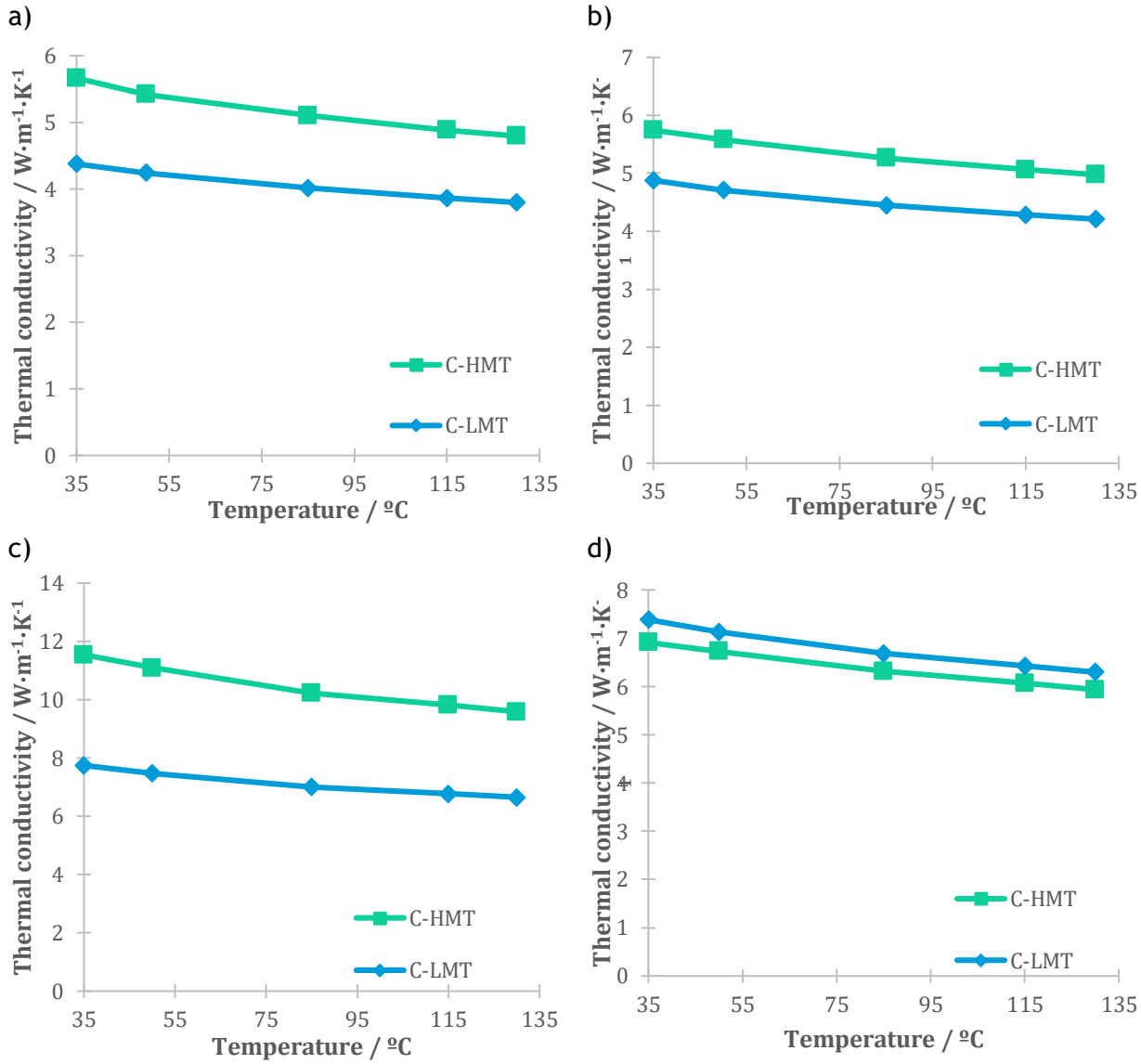


Figure D-13 - Through-plane thermal conductivity as a function of temperature of C-HMT and C-LMT in positions a) one, b) two, c) three and d) four.

Comparison of increase in through-plane thermal conductivity between sample C-HMT and C-LMT between positions

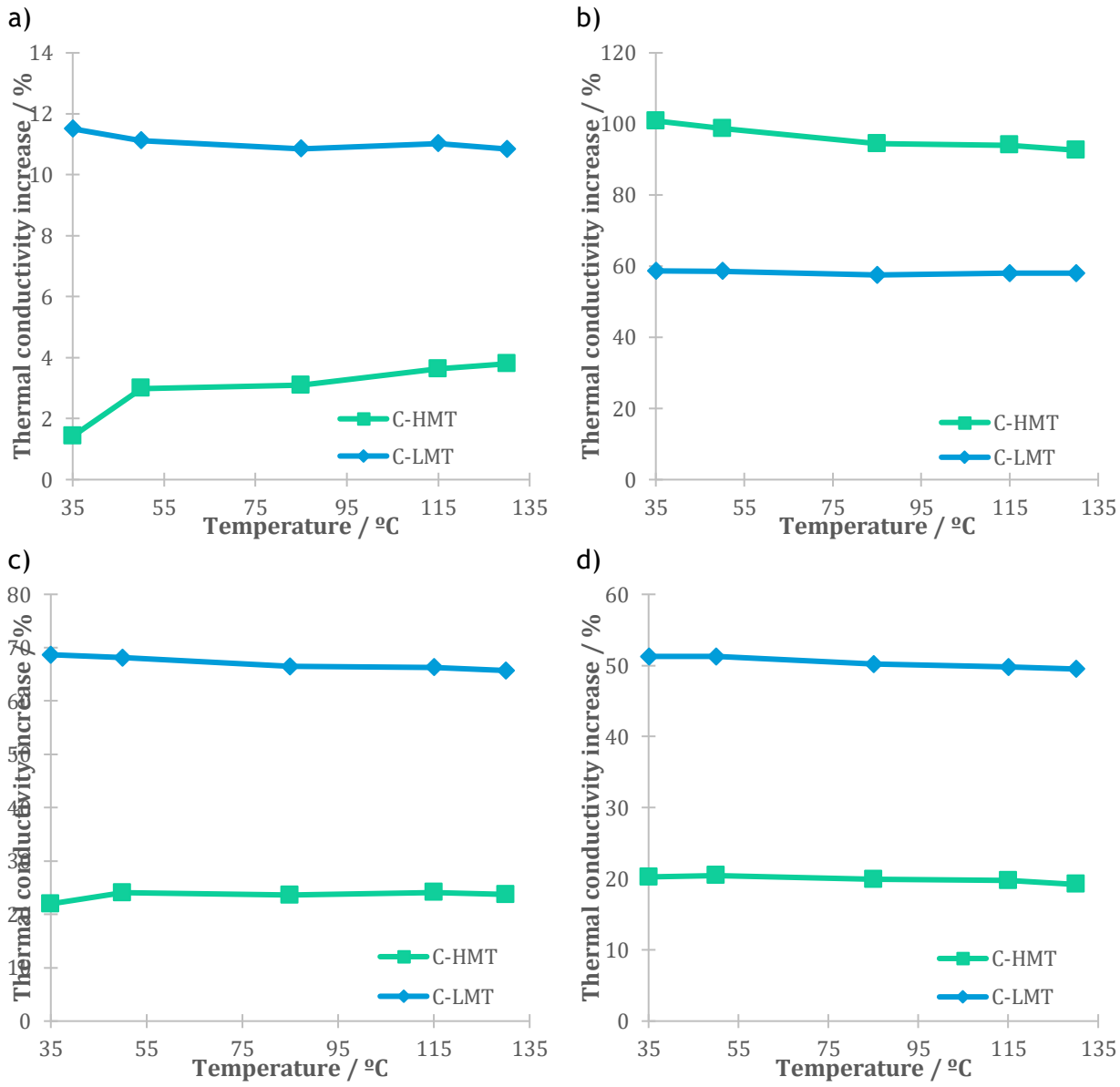


Figure D-14 – Increase in through-plane thermal conductivity for sample C-HMT and C-LMT between positions a) one and two, b) two and three, c) one and four and d) two and four.

D.4 Samples B and C

Comparison of through-plane thermal conductivity between sample B-HMT and C-HMT in each position

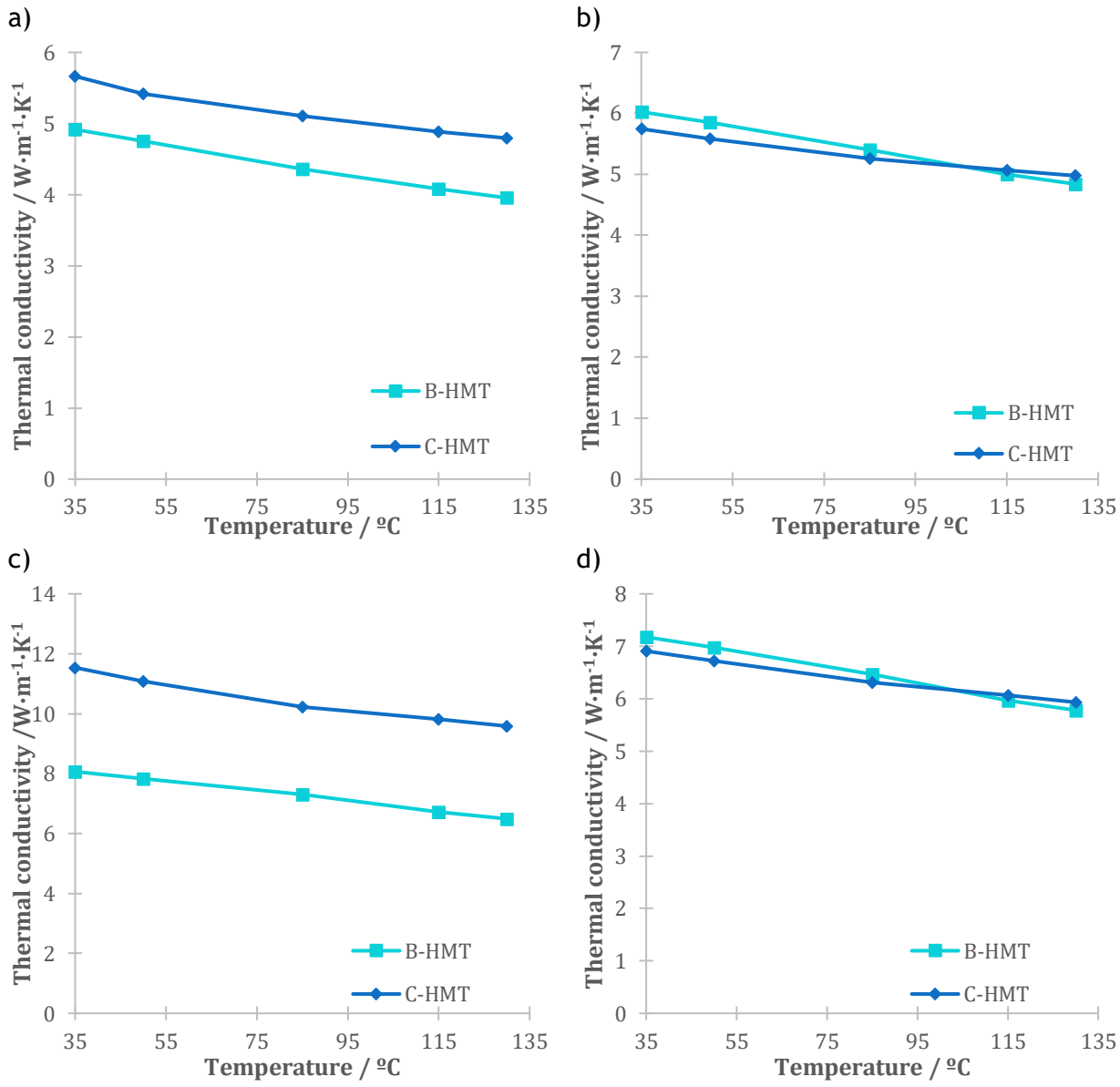


Figure D-15 - Through-plane thermal conductivity as a function of temperature of B-HMT and C-HMT in positions a) one, b) two, c) three and d) four.

Comparison of through-plane thermal conductivity between sample B-LMT and C-LMT in each position

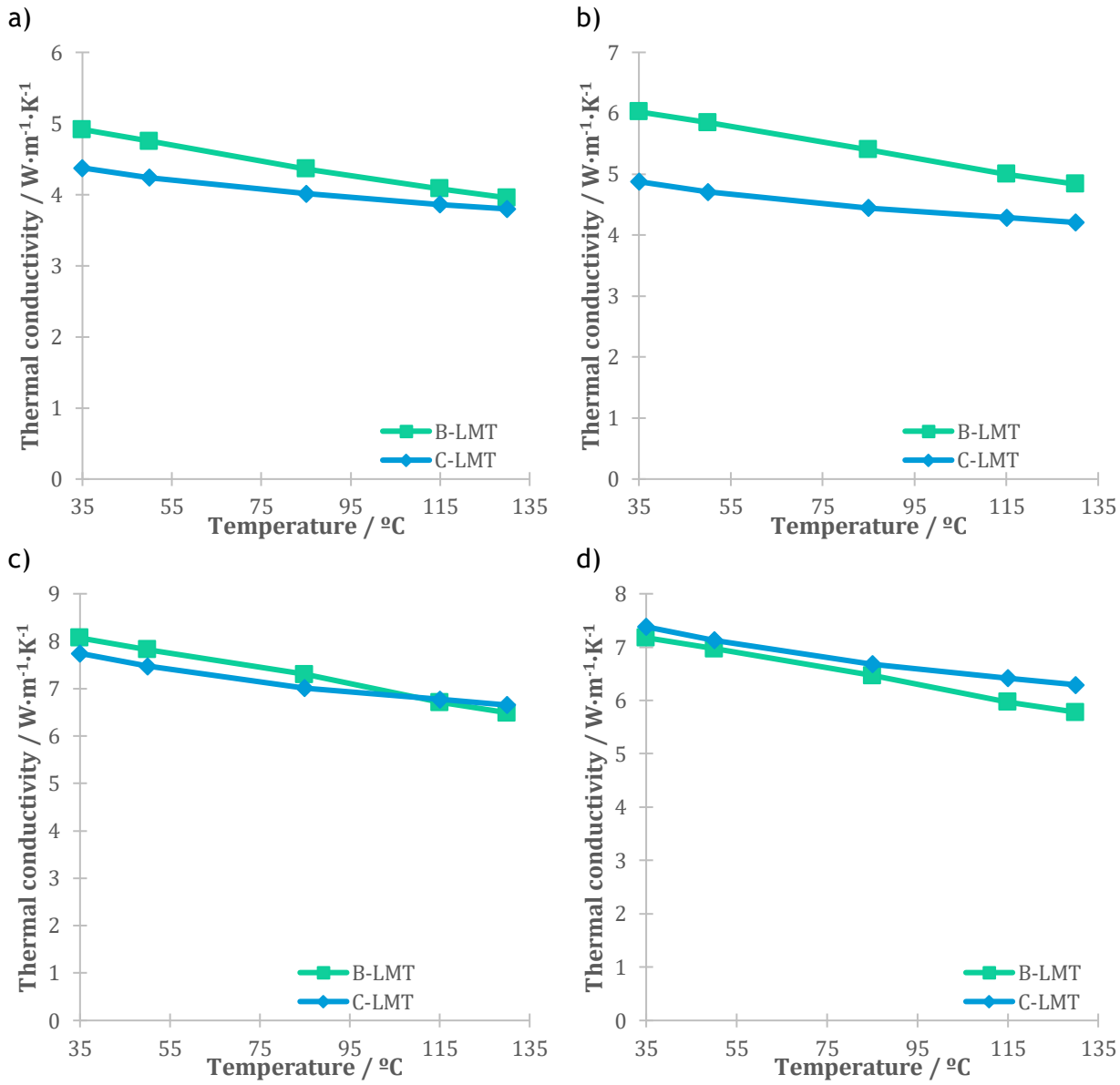


Figure D-16 - Through-plane thermal conductivity as a function of temperature of B-LMT and C-LMT in positions a) one, b) two, c) three and d) four.

D.5 Samples D-HMT and D-LMT

Sample D-HMT

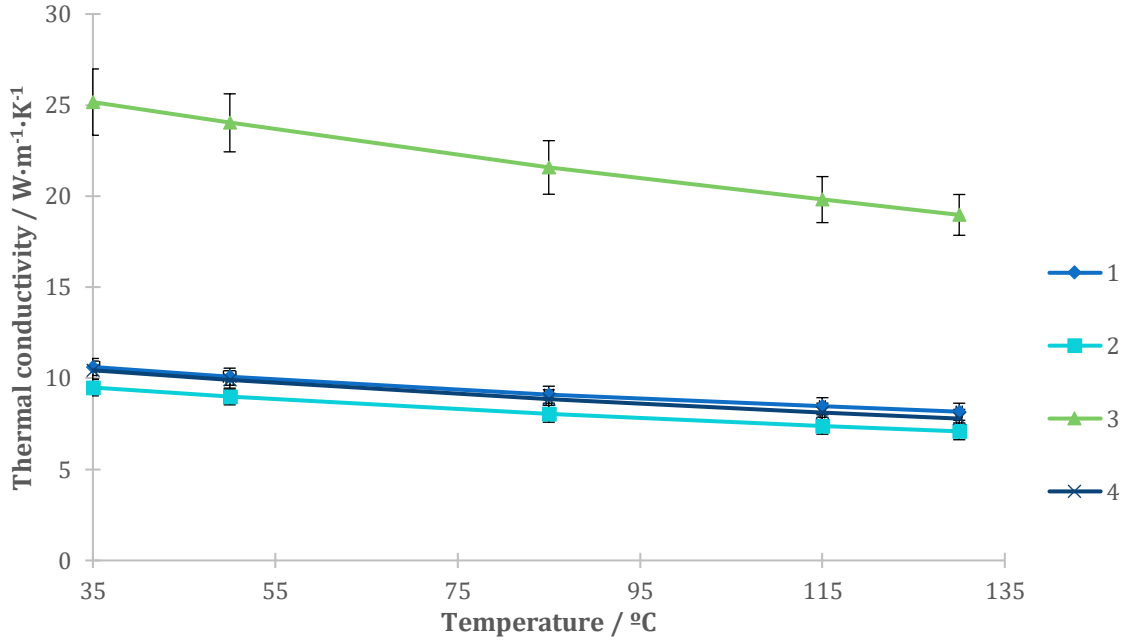


Figure D-17 – Through-plane Thermal conductivity as a function of temperature of sample D-HMT.

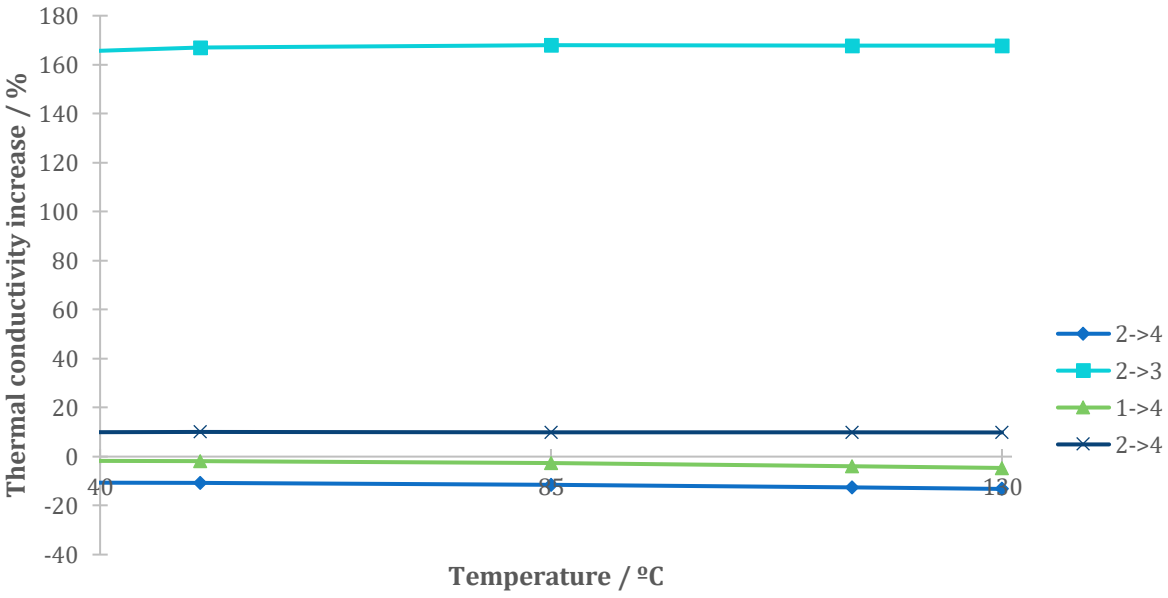


Figure D-18 – Percentual increase in thermal conductivity as a function of temperature between positions in sample D-HMT.

D-LMT

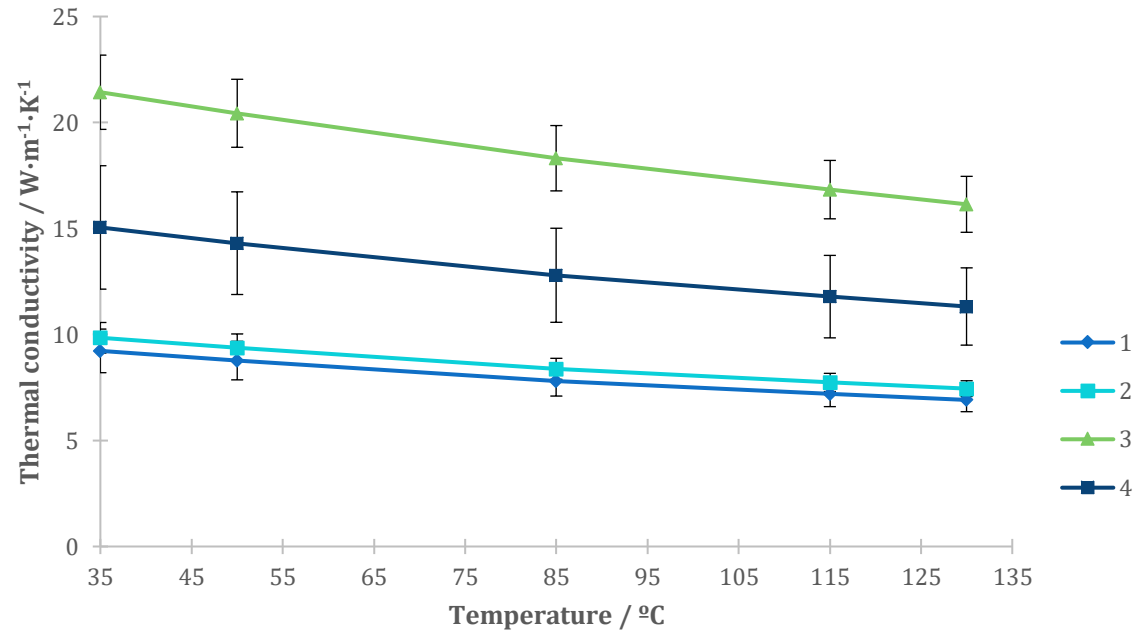


Figure D-19 – Through-plane Thermal conductivity as a function of temperature of sample D-LMT.

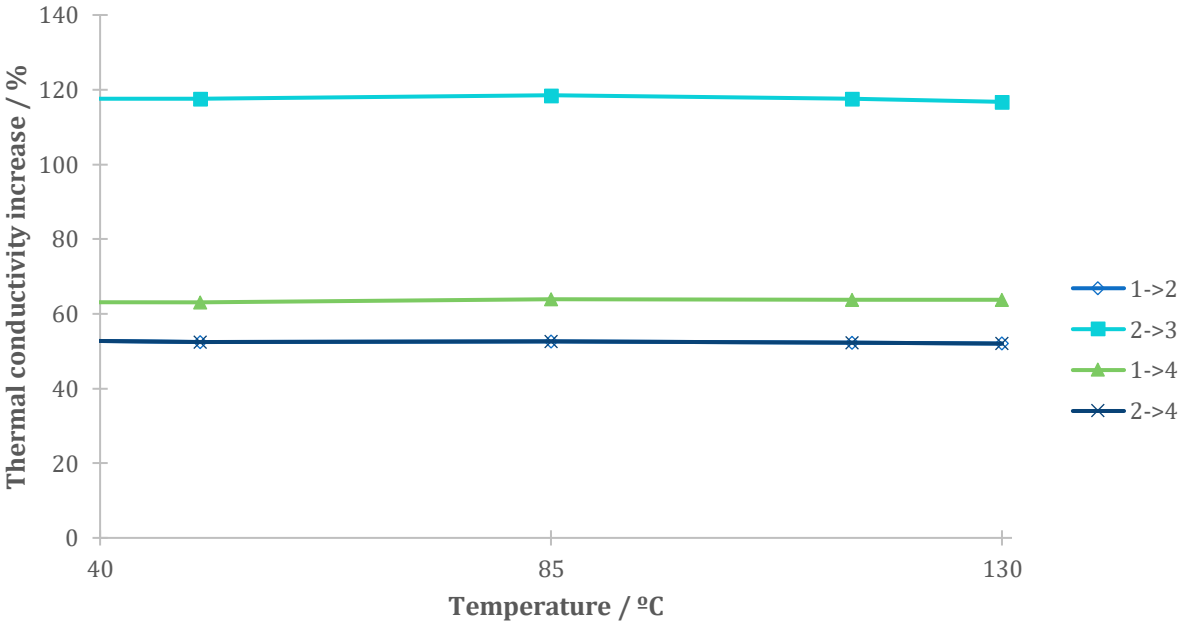


Figure D-20 – Percentual increase in thermal conductivity as a function of temperature between positions in sample D-LMT.

Comparison of through-plane thermal conductivity between sample D-HMT and D-LMT in each position

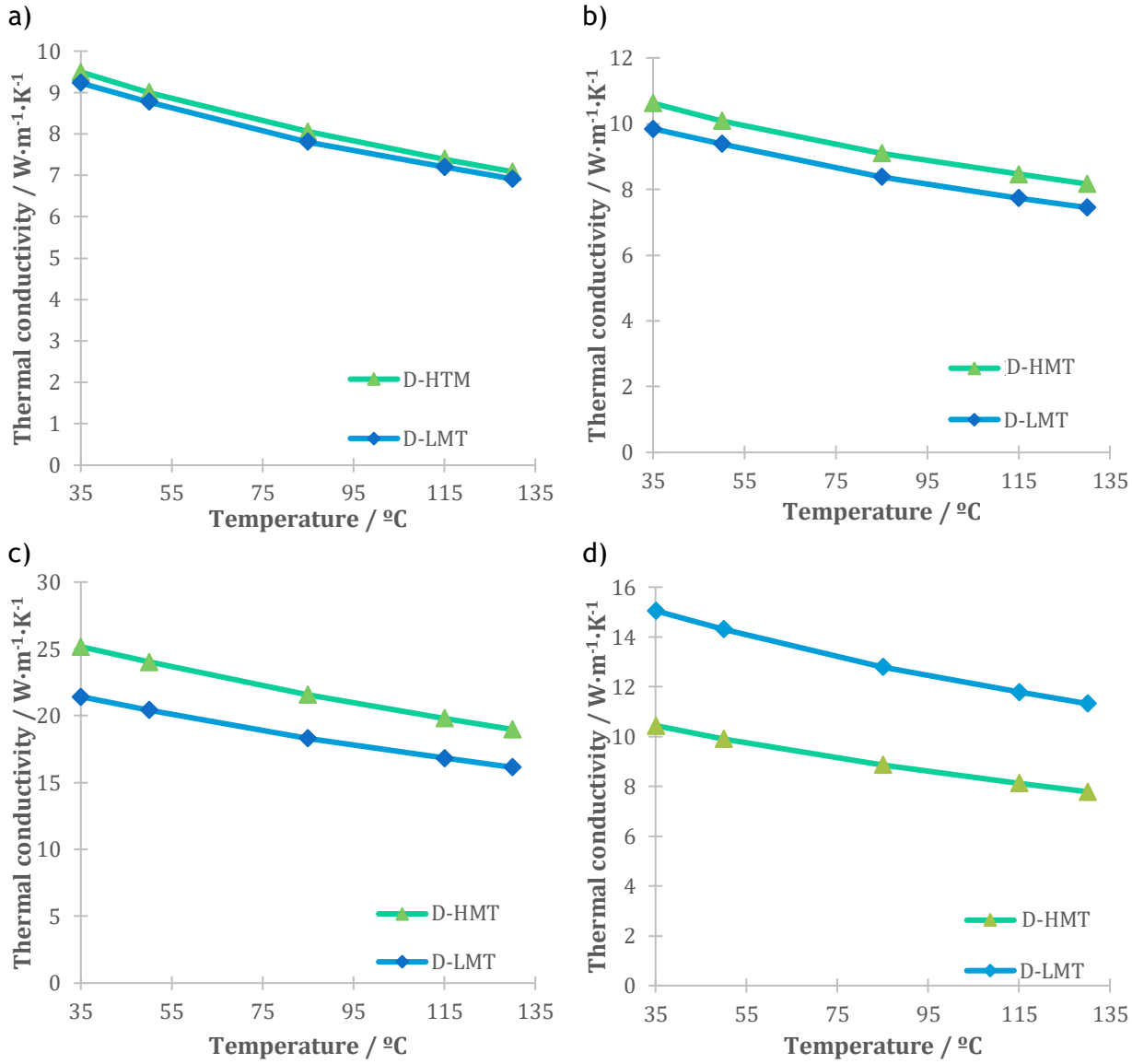


Figure D-21 - Through-plane thermal conductivity as a function of temperature of D-HMT and D-LMT in positions a) one, b) two, c) three and d) four.

Comparison of increase in through-plane thermal conductivity between sample D-HMT and D-LMT between positions

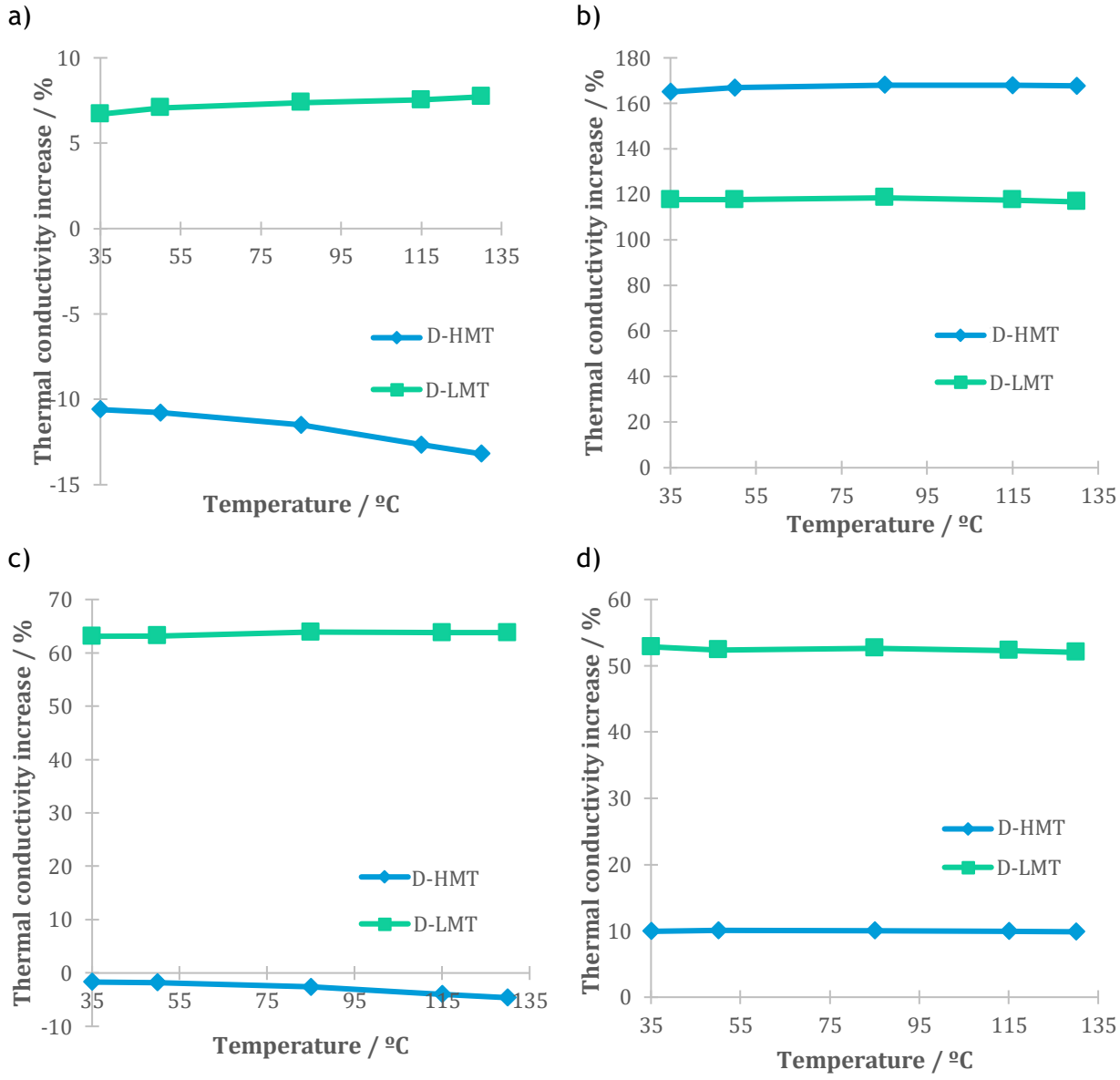


Figure D-22 – Increase in through-plane thermal conductivity for sample D-HMT and D-LMT between positions a) one and two, b) two and three, c) one and four and d) two and four.

Appendix E - SEM

SEM images of materials A, C-HMT, C-LMT, D-HMT and D-LMT are presented below, for the three positions on the flow direction evaluated in this dissertation.

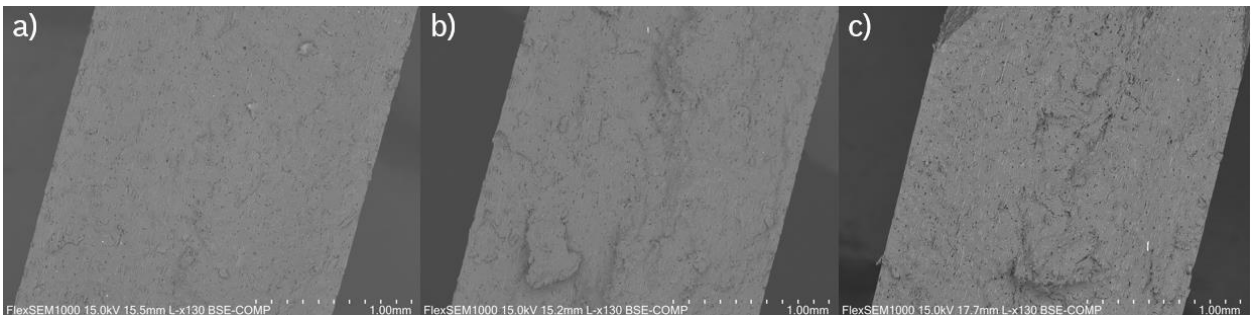


Figure E-1 – SEM image of sample A for positions a) one, b) two and c) three.

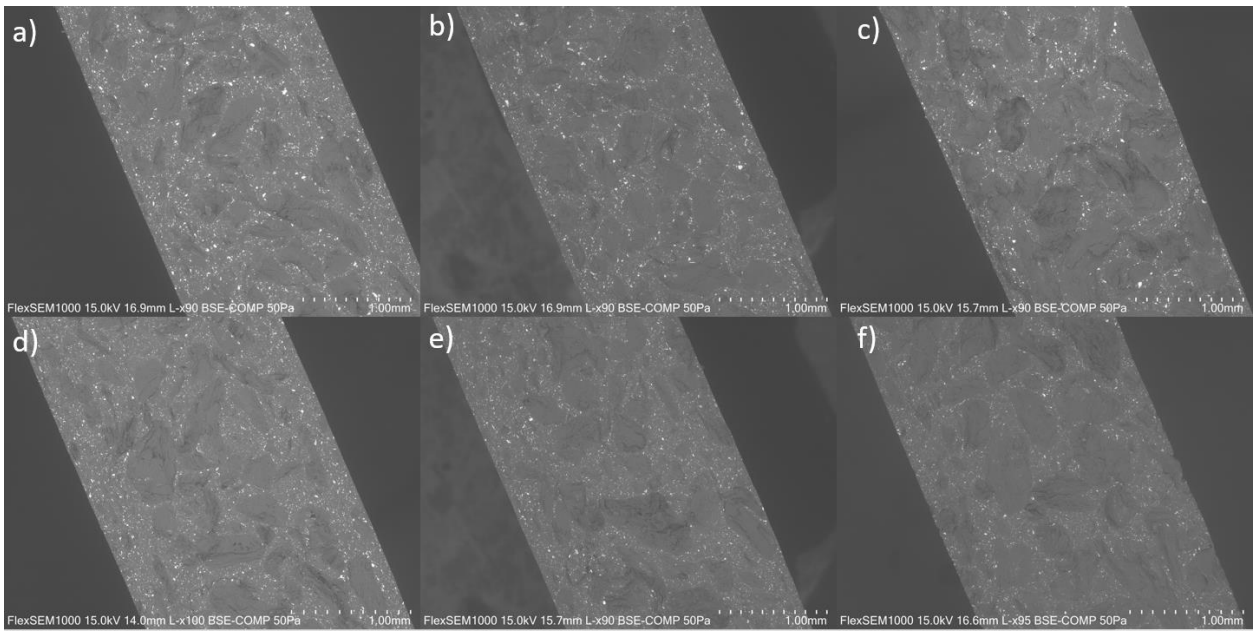


Figure E-2 – SEM image of sample C-HMT for positions a) one, b) two and c) three and sample C-LMT for positions d) one, e) two and f) three.

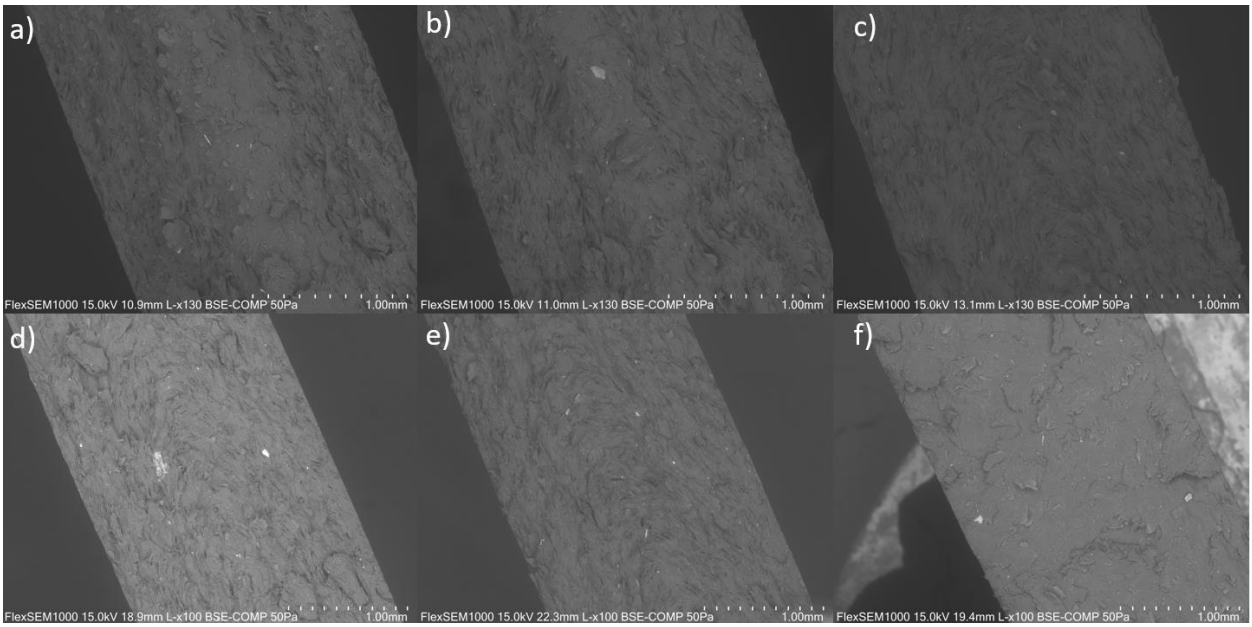


Figure E-3 – SEM image of sample D-HMT for positions a) one, b) two and c) three and sample D-LMT for positions d) one, e) two and f) three.

Appendix F - EDX

I.1 Material B

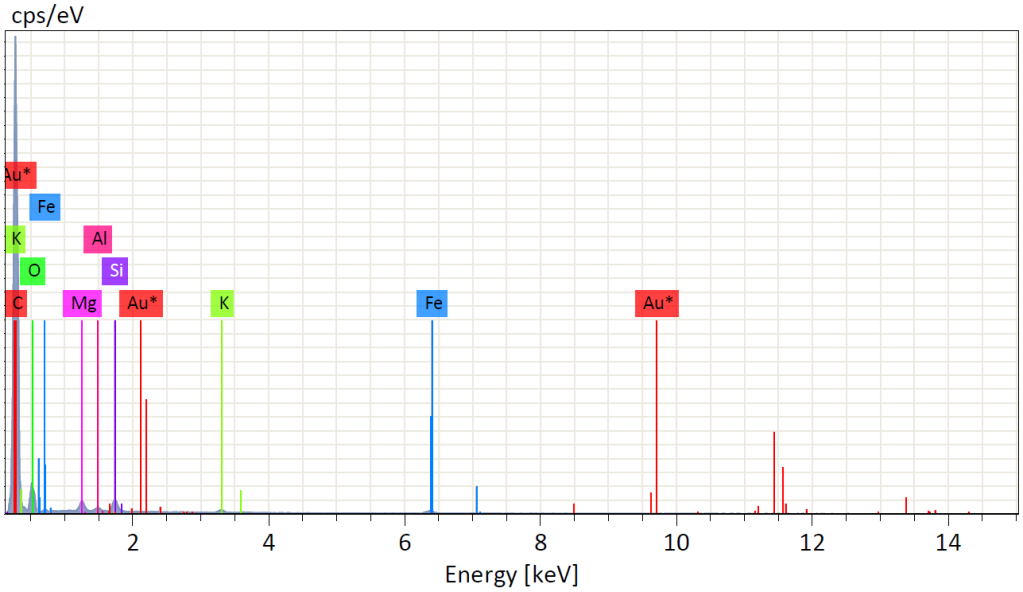


Figure F-1 – EDX spectrum for the material B-HMT.

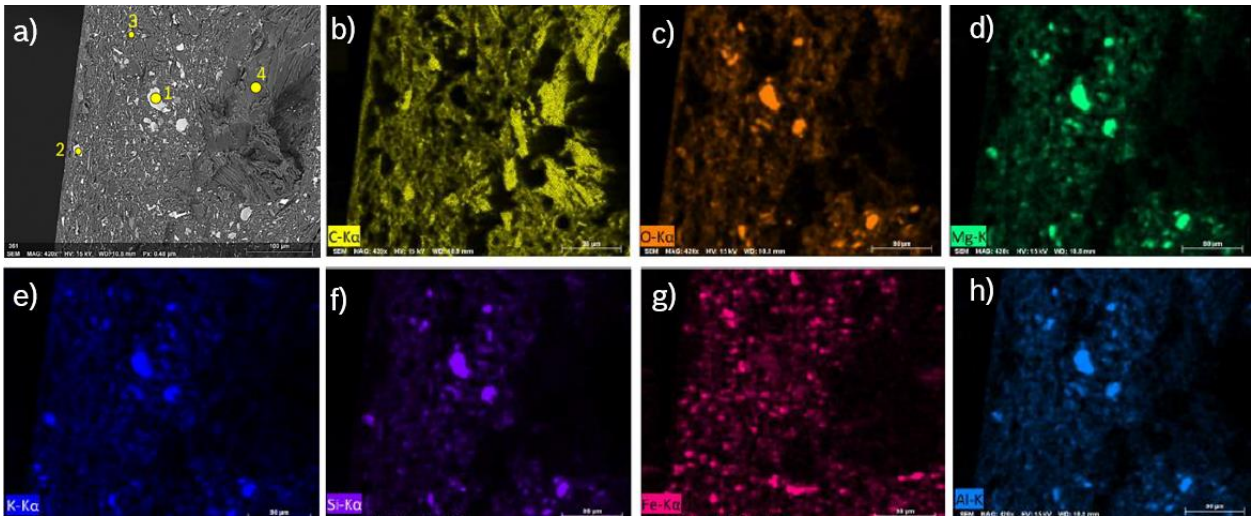


Figure F-2 –EDX mapping analysis of material B-HMT: a) analysed areas, b) Carbon (C), c) Oxygen (O), d) Magnesium (Mg), e) Potassium (K), f) Silicon (Si), g) Iron (Fe), and h) Aluminium (Al).

Table 13. Normalized mass concentration of the chemical elements constituting samples B-LMT and B-HMT, obtained by Energy Dispersive X-ray spectroscopy.

	Normalized mass concentration / %							
	Spectrum	C	O	Mg	Al	Si	K	Fe
B-HMT	Position 1	80.21	16.09	0.84	0.29	0.86	0.33	1.37
	Position 2	81.32	15.52	0.62	0.16	0.76	0.36	1.26
	Position 3	81.55	15.37	0.73	0.24	0.72	0.30	1.10
B-LMT	Position 1	82.85	14.33	0.63	0.20	0,64	0.26	1.09
	Position 2	79.63	16.56	0.85	0.26	0.88	0.34	1.48
	Position 3	83.07	13.67	0.72	0.25	0.80	0.31	1.18

I.2 Material C

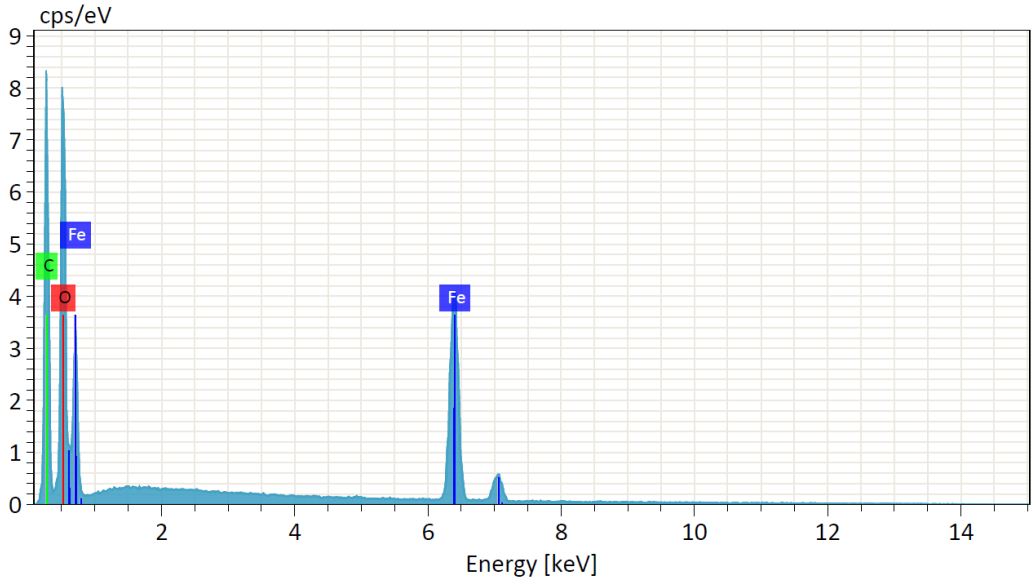


Figure F-3 - EDX spectrum for the material C-HMT.

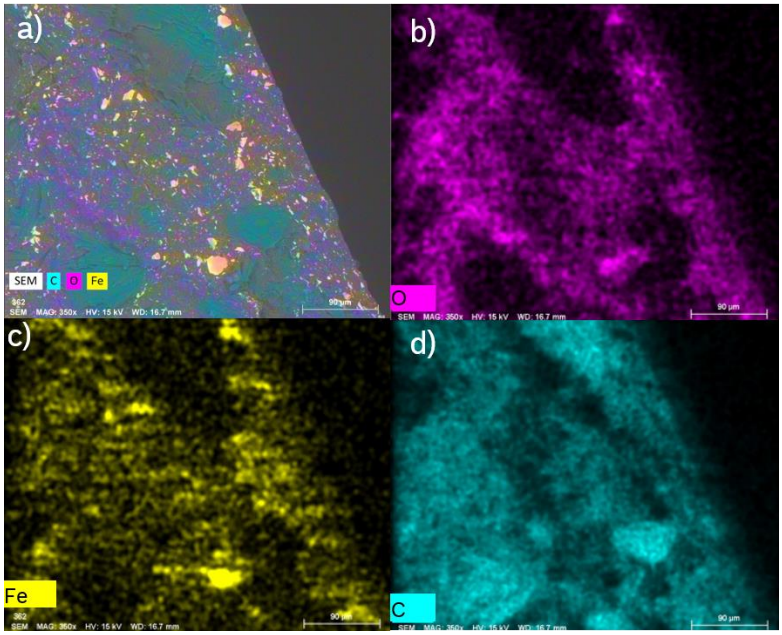


Figure F-4 – EDX mapping analysis of material C: a) analysed area, b) Oxygen (O), c) Iron (Fe), and d) Carbon (C).

Table 14. Normalized mass concentration of the chemical elements constituting samples C-LMT and C-HMT, obtained by Energy Dispersive X-ray spectroscopy

	Normalized mass concentration / %			
	Spectrum	**C**	**O**	**Fe**
C-HMT	Position 1	77.06	19.00	3.94
	Position 2	77.86	18.54	3.61
	Position 3	81.15	15.98	2.87
C-LMT	Position 1	80.35	16.38	3.27
	Position 2	80.05	17.00	2.95
	Position 3	80.76	16.79	2.45

I.3 Material D

Since sample D only contains graphite as fillers, the EDX analysis only detects Carbon, Oxygen and Nitrogen. Below is presented the EDX mapping analysis of material D, including residual traces.

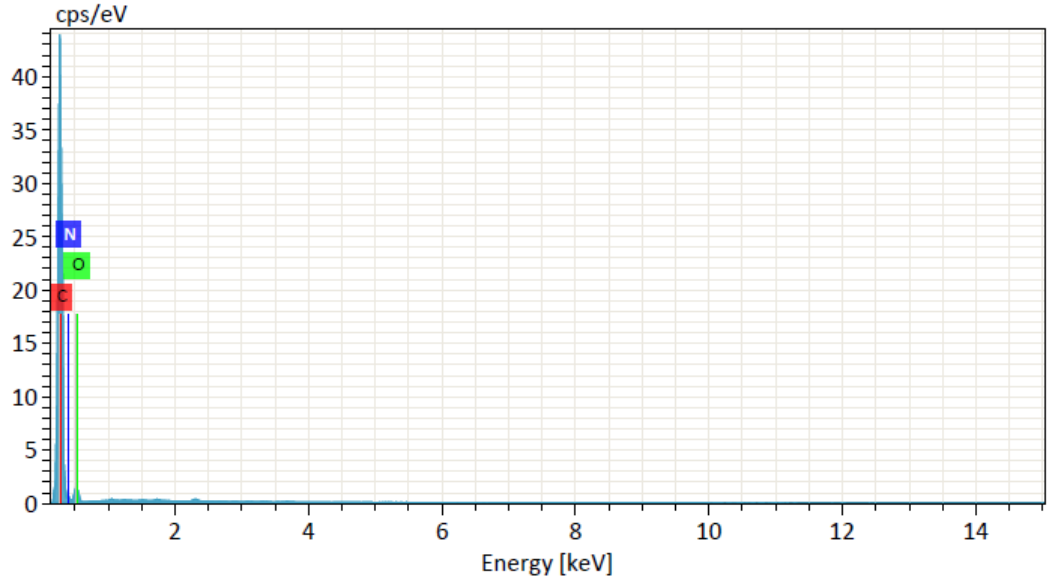


Figure F-5 – EDX spectrum for the material D-HMT.

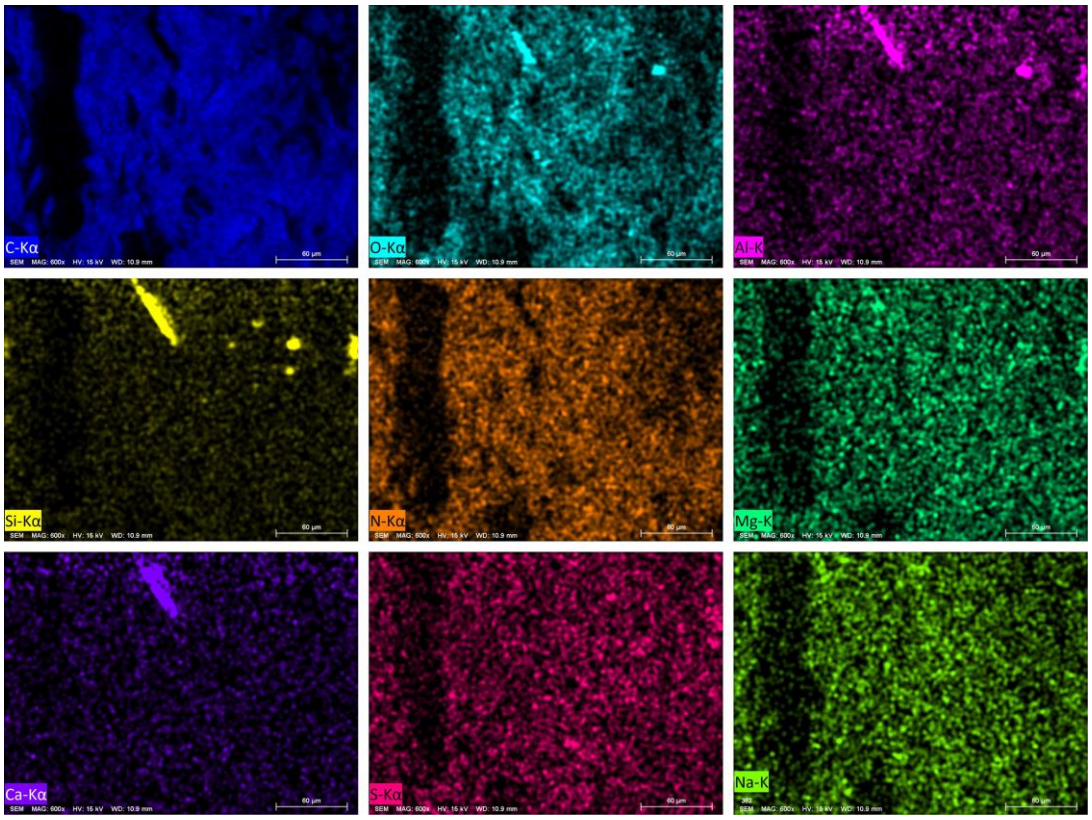


Figure F-6 – EDX mapping analysis of material D.

Table 15. Normalized mass concentration of the chemical elements constituting samples D-HMT, obtained by Energy Dispersive X-ray spectroscopy

Normalized mass concentration / %								
Spectrum	**C**	**N**	**O**	**Na**	**Mg**	**Al**	**Si**	**S**
Position 1	75.25	14.02	10.12	0.27	0.07	0.02	0.05	0.20

Appendix G - Image processing

The micrographs obtained by SEM were analysed using the software ImageJ. Below are presented the processed images, where the fillers are marked in red.

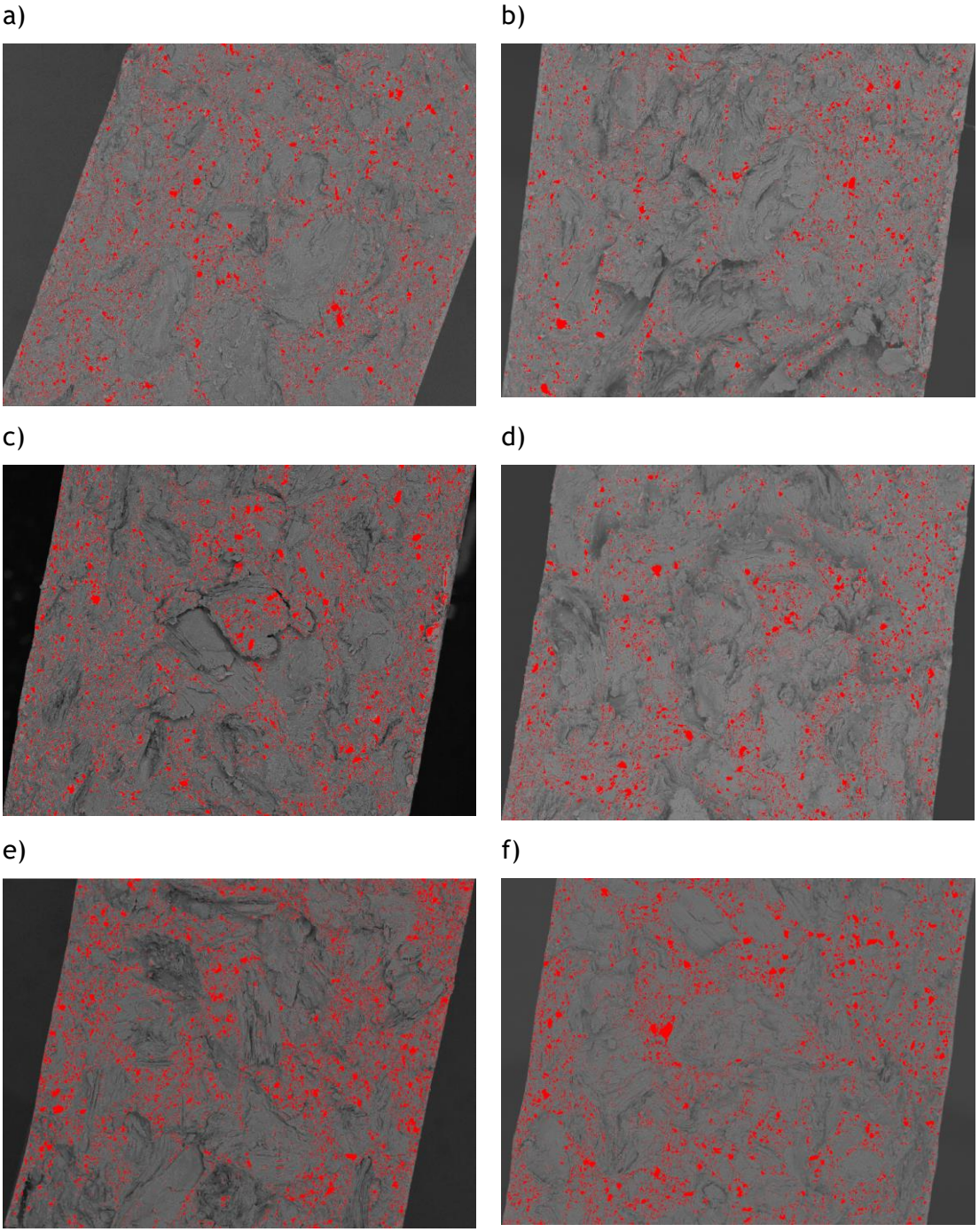


Figure G-1 – ImageJ for position: 1 a) B-HMT and b) B-LMT; position 2: c) B-HMT and d) B-LMT; position 3: e) B-HMT and f) B-LMT.

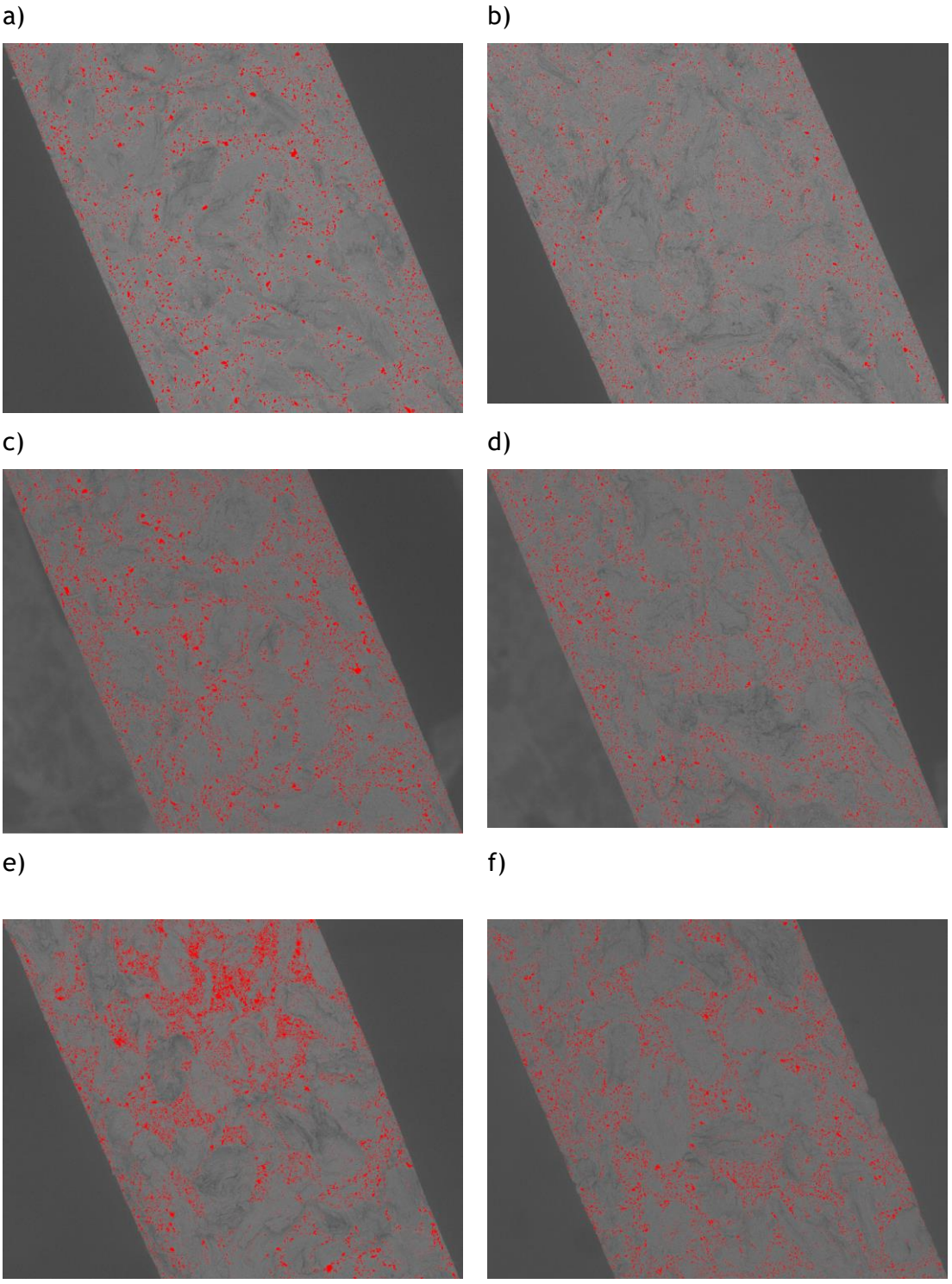


Figure G-2 – ImageJ for position: 1 a) C-HMT and b) C-LMT; position 2: c) C-HMT and d) C-LMT; position 3: e) C-HMT and f) C-LMT.

Appendix H - Lewis and Nielsen's Model parameters

The values of A and ϕ_m for many geometric shapes and orientation are given in Table 16 and Table 17, respectively.

Table 16. Value of A for various systems [56].

Type of dispersed phase	Direction of heat flow	A
Cubes	Any	2.0
Spheres	Any	1.50
Aggregates of spheres	Any	$(2.5/\varphi_n)$
Randomly oriented rods aspect ratio=2	Any	1.58
Randomly oriented rods aspect ratio=4	Any	2.08
Randomly oriented rods aspect ratio=6	Any	2.8
Randomly oriented rods aspect ratio=10	Any	4.93
Randomly oriented rods aspect ratio=15	Any	8.38
Uniaxially oriented fibers	Parallel to fibers	2L/D
Uniaxially oriented fibers	Perpendicular to fibers	0.5

Table 17. Value of Φ_m for various systems [56].

Shape of particle	Type of packing	Φ_m
Spheres	Hexagonal close	0.7405
Spheres	Face centered cubic	0.7405
Spheres	Body centered cubic	0.60
Spheres	Simple cubic	0.524
Spheres	Random close	0.637
Rods or fibers	Uniaxial hexagonal close	0.907
Rods or fibers	Uniaxial simple cubic	0.785
Rods or fibers	Uniaxial random	0.82
Rods or fibers	Three-dimensional random	0.52